Temperature Independent Anomalous Hall Effect in Thin Bismuth

Oulin Yu

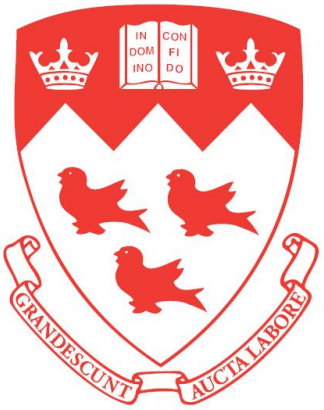

Department of Physics
McGill University
Montréal, Québéc, Canada

December 4, 2024

A thesis submitted to McGill University in partial
fulfillment of the requirements of the degree of
Doctor of Philosophy

"All truths are easy to understand once they are discovered; the point is to discover them."

– Galileo Galilei

"In Schottky we fought, in Onsager we trust."

– Guillaume Gervais

Acknowledgements

Without a doubt, this project would not have been possible without the support of my supervisor, Guillaume Gervais. His passion for physics and boundless energy are not only remarkable, but also contagious. This was especially crucial during the challenging years of my PhD, when I struggled and doubted, but he has always believed in me and this project. And he was right — I can proudly say that I am happy with what I have achieved. In fact, he is often right. And if I may give a word of advice for future members of the Gervais Lab: don't bet against him. I learned a great deal from Guillaume. Beyond the physics, what was most valuable was the way of thinking and approaching challenges that he imparted to me. Even outside the lab, we discovered we have much in common — motorcycle, food, wine, humor, and more. I am truly grateful to have him as my supervisor.

I would also like to thank my co-supervisor, Thomas Szkopek, for his patience and mentorship. Without the incredible amount of time he spent with me analyzing and troubleshooting the numerous challenges we faced in this project, I would not have made it this far. He complements Guillaume perfectly, and from Thomas, I gained a distinct set of skills. Despite their different approaches, both Thomas and Guillaume share one crucial quality: they deeply care about their students. I couldn't ask for better supervisors.

As the Gervais Lab alumnus Pierre-François Duc quotes in his thesis, "Ce n'est qu'en essayant continuellement qu'on finit par réussir & donc plus ça rate plus on a de chances que ça marche!" Indeed, failure is the mother of success, but failure is not

fun. However, the people who I spent the past years with at McGill made my PhD experience both encouraging and enjoyable. I especially want to thank the generation before me, Pierre-François Duc, Benjamin Schmidt, Matei Petrescu and Olivier Cyr-Choinière, for teaching me where to find everything and how things worked in the lab. A special thanks to Pierre-François for introducing me to the FRezCa project, which has made my spare time more meaningful. I am also grateful to my generation of the Gervais Lab members: Frederik Poitevin, Frédéric Boivin, Sujatha Vijayakrishnan, Talia Martz-Oberlander, Zachary Berkson-Korenberg, Nick Wicklund, Dawson Willerton and Renée Goodman. Thank you for your continuous support and making the lab a lively and harmonious place. And of course, I would like to thank the undergraduate students who worked in the lab and contributed in various ways. Many thanks to John Smeros, Richard Talbot, Robert Gagnon and Pascal Bourseguin — you made everything much easier.

Among the above-mentioned people, Frederik Poitevin, Frédéric Boivin, and Avram Silberztein deserve a special thank you for their significant contributions to this bismuth project. Frédéric Boivin assisted me with the high-field measurements at the magnet lab — I hope it wasn't too intense and that you still had a great time. Avram was always there to challenge me and introduce new theories, which is exactly what I believe science should be. And thank you, Frederik, for building the Triton fridge and for sharing it with all of us.

Just a few hundred meters down the hill from the Rutherford building, in McConnell, I could always find my two good friends, Eli Martel and Minh Tran. Thank you for being there — for the fun coffee breaks and all the activities we enjoyed outside of campus. These moments were invaluable.

Finally, I want to express my deepest gratitude to my family, especially my parents. They were the first to teach me about the scientific method and the importance of critical thinking. They nurtured my curiosity and, most importantly, planted the seed that led me to pursue physics.

Abstract

Bismuth is one of the oldest metals known to human kind and one of the most extensively studied materials. It is often called a "wonder" material due to the many significant discoveries made in bulk bismuth, including diamagnetism, quantum oscillations, thermoelectric effects and quantum confinement effects. Even in the era of low dimensional materials, bismuth continues to spark interest among scientists. Notably, there are substantial evidences that bismuthene, the two-dimensional limit of bismuth, is a higher order topological insulator and acts as a superconductor below a critical temperature of $T_c \approx 0.5$ mK.

In solid-state physics, the Hall effect family has also been extensively studied and continues to be an active area of research. Among its many variants, the anomalous Hall effect (AHE) remains controversial even after 150 years of investigation. It is only with the recent understanding of Berry curvature have the different mechanisms become less obscure, and we now have a better picture of the three mechanisms at play — the intrinsic, skew scattering and side-jump mechanisms. Despite the specific mechanism involved, breaking time-reversal symmetry (TRS) remains a necessary condition for the AHE to occur, and as such, one would least expect diamagnetic bismuth to exhibit the AHE since broken TRS typically occurs in ferromagnetic systems.

In this thesis, we developed a novel mechanical exfoliation method to isolate thin bismuth flakes down to 2 nm. Using this technique, we fabricated thin bismuth devices with thicknesses ranging from 29 to 69 nm, where we unambiguously observed the anomalous Hall effect accompanied by a longitudinal resistance with no magnetoresis-

tance up to ± 30T. Most notably, these behaviors exhibit negligible temperature dependence between 15 mK and 300 K, and this lack of temperature dependence suggests that the hidden mechanism for broken TRS in thin bismuth leading to the observed AHE, is indeed intrinsic.

Abrégé

Le bismuth est l'un des métaux les plus anciens connus par l'humanité et l'un des matériaux les plus étudiés. Il est souvent appelé un matériau "miracle" en raison des nombreuses découvertes significatives faites dans le bismuth, y compris le diamagnétisme, les oscillations quantiques, les effets thermoélectriques et les effets de confinement quantique. Même à l'ère des matériaux de basse dimension, le bismuth continue de susciter l'intérêt des scientifiques. Notamment, il existe des évidences substantielles que le bismuthène, la forme bidimensionnelle du bismuth, est un isolant topologique de haut ordre et agit comme un supraconducteur en dessous d'une température critique de $T_c \approx 0,5$ mK.

Dans un autre ordre d'idée, en physique de l'état solide, la famille des effets Hall a également été largement étudiée et reste un domaine de recherche actif. Parmi ses nombreux types, l'effet Hall anormal reste disputé même après 150 ans d'investigation. Ce n'est qu'avec la compréhension récente de la courbure de Berry que les différents mécanismes sont devenus moins obscurs, et nous avons maintenant une meilleure idée des trois mécanismes en jeu : le mécanisme intrinsèque, la diffusion et le «side-jump». Quel que soit le mécanisme impliqué, la rupture de la symétrie par renversement du temps reste une condition nécessaire pour que l'effet Hall anormal se produise. Ainsi, on ne s'attendrait pas nécessairement à retrouver l'effet Hall anormal dans le bismuth qui est un matériau diamagnétique, car la rupture de la symétrie par renversement du temps se produit généralement dans des systèmes ferromagnétiques.

Dans cette thèse, nous avons développé une nouvelle méthode d'exfoliation mé-

canique pour isoler des couches minces de bismuth jusqu'à une épaisseur de 2 nm. En utilisant cette technique, nous avons fabriqué des dispositifs de bismuth avec des épaisseurs moyennes allant de 29 à 69 nm, où nous avons observé sans ambiguïté l'effet Hall anormal accompagné d'une résistance longitudinale sans magnétorésistance jusqu'à ± 30 T. Notamment, ces comportements varient de façon négligeable selon la température dans une intervalle entre 15 mK et 300 K. Cette absence de dépendance en température implique que le mécanisme de rupture de la symétrie par renversement du temps dans le bismuth qui engendre l'effet Hall anormal observé, est effectivement intrinsèque.

Contributions and Statement of Originality

This thesis presents my original contributions to the field of condensed matter physics. Previous works on bismuth and the anomalous Hall effect are thoroughly cited. In this section, I detail my specific contributions as the primary author, along with the contributions from my co-authors.

- *Mechanical exfoliation utilizing micro-trenches:* A novel mechanical exfoliation technique is developed in order to produce thin bismuth flakes down to 2 nm. Previous mechanical exfoliation methods were proven to be ineffective for bismuth, since its interlayer bonds are stronger than that of graphene or phosphorene. The idea of using micro-trenches patterned on SiO_2/Si substrate in order to facilitate the exfoliation of bismuth was conceived by my supervisors, Thomas Szkopek (TS) and Guillaume Gervais (GG). The fabrication, characterization and the study of gate leakage of the micro-trenches were carried out by myself (OY). The exfoliation and characterization of the exfoliated flakes were performed by OY, and assisted by Simon Godin (SG), Jacob Lalande (JL) and Paolo Fossati (PF). Raphaela Allgayer (RA) helped with the Raman spectra as well as their analysis. OY and SG worked together on the flake visibility. Finally, OY analyzed nearly 500 flakes to study the relationship between flake thickness and flake surface area while stuck at home during COVID. Everyone, along with Chunwei Hsu, who worked on the exfoliation of bismuth flakes at an earlier stage, reviewed the manuscript writ-

ten by OY. This manuscript, reported in *J. Appl. Phys.* **134**, 244302 (2023), is presented in Chapter 3, and the Supplemental Material is found in Appendix A.

- *Fabrication of thin bismuth devices:* The fabrication process was conducted by OY, with support from staffs at McGill Nanotools, the Laboratoire de microfabrication at Polytechnique Montréal, and the Interdisciplinary Institute for Technological Innovation at Sherbrooke University. GG, TS and Marie-Hélène Bernier provided essential guidance in troubleshooting. Eli Martel, Minh Tran, and Frederik Poitevin (FP) contributed through valuable discussions, while FP, Robert Gagnon and Vahid Tayari offered expertise in soldering and wire-bonding. Postmortem analysis of non-working devices were done by OY and Avram Silberztein (AS).

- *Low temperature and high magnetic field techniques:* I was extremely fortunate to have access to dilution refrigerators equipped with magnets already set up for the measurements. These were maintained by FP, Matei Petrescu, and Sujatha Vijayakrishnan, while GG provided expertise in low-temperature and high-field measurements.

- *Anomalous Hall effect in thin bismuth:* The transport measurements that led to the discovery of the anomalous Hall effect in thin bismuth, along with finding an absence of magnetoresistance, were conducted by OY. The initial findings and analysis using Onsager symmetrization were also led by OY, with significant guidance provided by GG. This work, reported in *Phys. Rev. B* **109**, L121406 (2024), is discussed in Chapter 4. The Supplemental Material is found in Appendix B.

- *Temperature independent anomalous Hall effect:* Further investigation of the anomalous Hall effect in thin bismuth was conducted at the National High Magnetic Field Laboratory in Tallahassee, Florida, with the support of Shalinee Chikara and Shermane Benjamin. It was unexpectedly found that the anomalous Hall effect in bismuth is entirely temperature independent. Additionally, the magentoresistance remained absent up to a field of ± 30 T, which was also surprising.

These experiments, guided by GG, were performed by OY and Frédéric Boivin, leading to the manuscript discussed in Chapter 5. In the Supplemental Material presented in Appendix C, the conductivity scaling analysis was performed by OY while AS contributed significantly to important discussions.

Contents

List of Figures

List of Abbreviations

2D	Two-dimensional
AFM	Atomic force microscopy
AHC	Anomalous Hall conductivity
AHE	Anomalous Hall effect
CVD	Chemical vapor deposition
EBL	Electron beam lithorgraphy
FQHE	Fractional quantum Hall effect
HOTI	Higher order topological insulator
IQHE	Integer quantum Hall effect
IS	Inversion symmetry
MBE	Molecular beam epitaxy
NHMFL	National High Magnetic Field Laboratory
PMMA	Polymethylmethacrylate
PVD	Physical vapor deposition
QAHE	Quantum anomalous Hall effect
RIE	Reactive ion etching
SM	Supplemental Material
SMSC	Semimetal-to-semiconductor
SdH	Shubnikov-de Haas
TEM	Tunneling electron miscroscopy
TRS	Time-reversal symmetry
VTI	Variable temperature insert
vdW	van der Waal

1

Introduction

1.1 Introduction

Two central ideas of the Scientific Revolution during the Renaissance laid the foundation for modern science. The first is the use of mathematics to describe physical phenomena, epitomized by Galileo's famous quote: "The book of nature is written in the language of mathematics", and further emphasized by Eugene Wigner's 1960 article, "The Unreasonable Effectiveness of Mathematics in the Natural Sciences". Equally crucial is the shift toward diligent experimentation, which marked a departure from the speculative natural philosophy of the ancient world. This rigorous empirical approach has been fundamental to countless scientific discoveries, shaping the course of modern science.

Arguably just as important to science are perseverance and the pursuit of curiosity —

qualities I have learned extensively from both of my supervisors. While I could motivate this project by listing the exciting properties of bismuth and why it is considered a "wonder material", I will reserve that discussion for Chapter 2. The reality is that, even before I joined the lab, Guillaume and Thomas had already collaborated on identifying their next "big" project. At that time, phosphorene had just been exfoliated, prompting them to examine the remaining group V elements, with bismuth emerging as the last frontier — an element that is heavy, radioactively stable, and relatively unexplored in the two-dimensional world. When asked about the motivation to research on bismuth, Guillaume's answer is simply, "Why not"? This same spirit of curiosity and this urge to explore are what drove me to physics in the first place.

Strictly speaking, there were goals: fabricating transport devices from the thinnest possible bismuth flakes, and measuring them. This thesis condenses that journey and its exciting findings into a short diary.

1.2 Thesis Outline

First, the theory and the background are introduced in Chapter 2, where the "wonder material" bismuth and the anomalous Hall effect are discussed along some basics on transport measurement. Three manuscript chapters follow. Chapter 3 presents the novel mechanical exfoliation technique utilizing micro-trenches. Chapter 4 gives the first important finding, an emergence of the anomalous Hall effect in bismuth along with a surprising absence of any magnetoresistance. Finally, Chapter 5 demonstrates that this anomalous Hall effect is temperature independent, but also increases the range of investigated magentic fields to ± 30 T for both the Hall and longitudinal signals. The Supplemental Materials for these published articles are added to the appendices. Further, Chapter 6 expands on the discussion for all three manuscripts before the thesis is concluded in Chapter 7.

2

Theory and Background

This chapter provides the essential background information necessary for understanding the subsequent chapters of this thesis. It is divided into three sections. The first section presents a brief history and highlights the key properties of bismuth, which is central to this project. This background explains the rationale for researching bismuth which led to our discovery of the anomalous Hall effect in thin bismuth. The second section reviews the anomalous Hall effect and its quantized version, the quantum anomalous Hall effect. Finally, the third section covers transport measurements, including the renowned Onsager reciprocity theorem, as these are crucial for interpreting the results presented in this project.

2.1 Bismuth

2.1.1 History

Bismuth has been known since ancient times due to its natural occurrence in elemental form. Its silvery-white appearance likely inspired its name, derived from the German term *wismut*, meaning “weiße Masse" or “white mass", or possibly from *bleiweiss*, meaning “white lead” [1]. It was frequently mistaken for tin or lead because of their similar appearance and metallurgical properties until the French chemist Claude François Geoffroy clarified the differences in the 18^{th} century.

Scientifically, bismuth is notable for being the first material in which many physical phenomena were discovered. As the most diamagnetic material found in nature, bismuth was observed by Anton Brugmans to be slightly repelled by a magnet. Further experimentation by Michael Faraday revealed that this repulsion is a fundamental property of matter, leading him to coin the term “diamagnetism” in 1845 [2]. Unlike other metals, bismuth exhibits very low thermal conductivity and a high Hall coefficient, resulting in an exceptionally high Ettingshausen coefficient ($\sim 10^{-4}$ m·K/(T·A)) that is many orders of magnitude greater than that of metals like copper, silver, and gold ($\sim 10^{-16}$ m·K/(T·A)) [3]. This distinctive property led Albert von Ettingshausen and Walther Nernst to discover the Nernst-Ettingshausen effect in 1886, following their accidental observation of a temperature gradient when they heated one side of a bismuth sample.

Bismuth is also renowned for its remarkable electronic transport properties. In 1928, Peter Kapitza, through studying bulk bismuth, formulated his famous law of magnetoresistance. In 1930, after the brief four-year collaboration with Wander Johannes de Haas, Lev Shubnikov discovered that the longitudinal resistance of low-impurity bismuth crystals exhibited magnetic oscillations, now known as the Shubnikov-de Haas (SdH) effect which is a precursor to the quantum Hall effect. Shortly after this discovery in 1930, de Haas, along with his student Pieter M. van Alphen, was inspired to

further investigate the magnetic susceptibility of bismuth, leading to the discovery of the de Haas-van Alphen effect in the same year.

These physical phenomena are just some examples of the effects first discovered in bismuth. This certainly makes bismuth a remarkable material, with some even referring to it as a "wonder material" due to the insights gained from its unusual properties, including low carrier densities, small effective mass, high mobilities, and long free paths.

2.1.2 Renaissance

Towards the end of the 20th century, bismuth in its elemental form lost some of its trend, giving way to a focus on bismuth-based compounds. For example, bismuth selenide, Bi_2Se_3, was shown to be an intrinsic topological insulator [4], leading to its increased popularity among physicists and engineers. However, there has been a recent resurgence of research into elemental bismuth.

A major advancement in material science and solid-state physics in the 21st century was the successful isolation of graphene, a material consisting of a single atomic layer of carbon. This achievement was recognized with the Nobel Prize in 2010, awarded to Andre Geim and Konstantin Novoselov, marking the beginning of a new era for two-dimensional materials. Since then, scientists have sought to exfoliate or grow other materials in their two-dimensional forms. A logical avenue of exploration has been the group V elements in the periodic table, which share a similar hexagonal structure to graphene but with varying degrees of buckling. Phosphorene, the single-layer form of black phosphorus, was successfully exfoliated in 2014 [5,6]. However, as we move down the group V elements, the interlayer bonds become stronger making traditional exfoliation methods challenging, and to date, clean mechanical exfoliation of bismuthene has not yet been possible.

Despite these challenges, F. Reis *et al.* successfully grew bismuthene on a SiC substrate using molecular beam epitaxy in 2017 [7], demonstrating its potential as a candidate for realizing the quantum spin Hall effect. Along with efforts from different

research groups across the globe, this rekindled interest in elemental bismuth by highlighting its promising physical properties in thin layers. Notably, it was later shown that bismuth is a higher-order topological insulator [8, 9] and exhibits superconductivity [10]. Nevertheless, many aspects of its electronic transport properties in its lower-dimensional forms remain unexplored and await to be unraveled. This is precisely the focus of my doctoral thesis project which led to the discovery of the anomalous Hall effect in thin bismuth despite ambiguous evidence has been reported in the bulk in 2021. These above-mentioned key discoveries are summarized in Fig. 2.1.

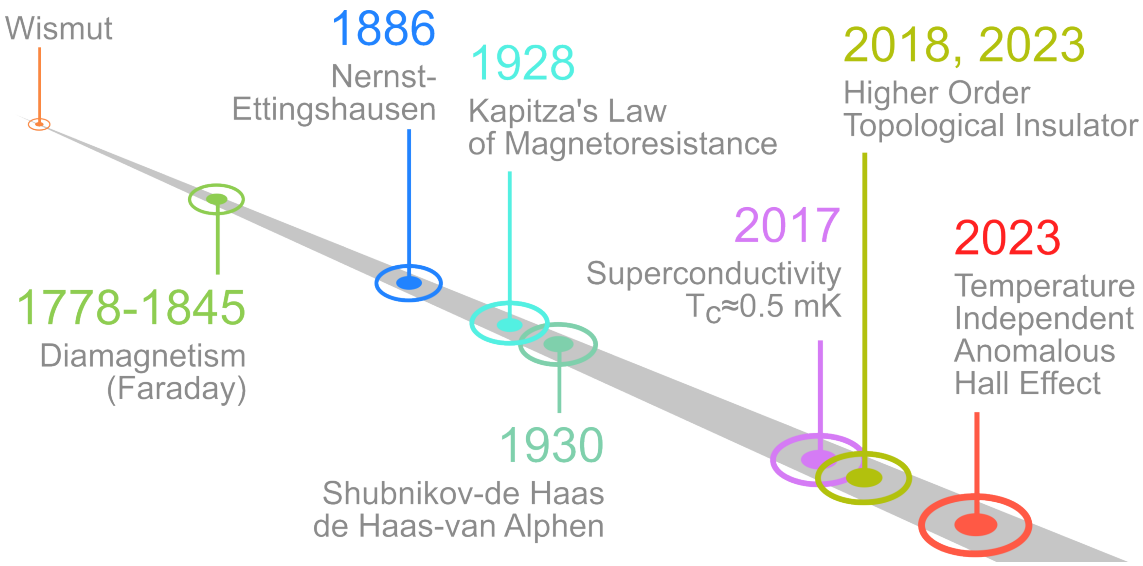

Figure 2.1: The time line for the key discoveries made with bismuth.

2.1.3 Bulk Electronic Band Structure

As for any other material, the point of departure for the description of band structure would be the crystal structure. For bulk bismuth, we adopt the convention of a rhombohedral Bravais lattice with two atoms per unit cell, as illustrated in Fig. 2.2. The unit cell is shaded in gray, and the trigonal axis perpendicular to the (111) plane is clearly indicated. Note that the bismuth atom in the center has three equidistant nearest neighboring atoms and three equidistant atoms that are slightly further. This arrangement gives the buckled hexagonal structure on the (111) surface, which will be discussed further in Section 2.1.5.

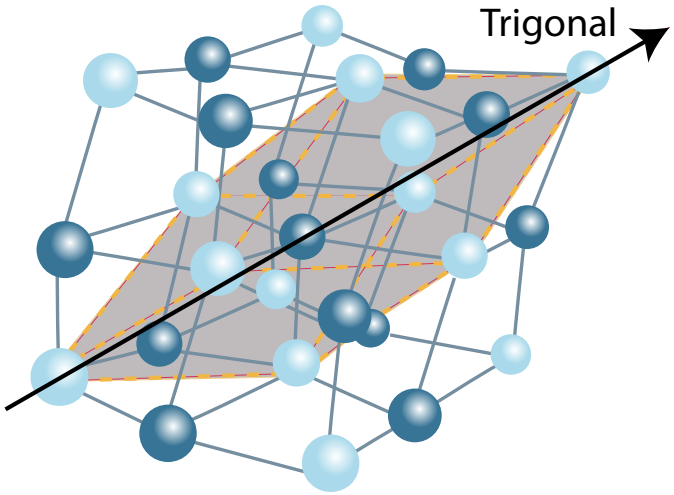

Figure 2.2: The rhombohedral crystal structure of bulk bismuth. The shaded area represents the unit cell containing two atoms.

The tight-binding and first-principle calculations of the electronic band structure, along with the Brillouin zone of bulk bismuth, are presented in Fig. 2.3. Given that bismuth is a heavy element with high spin-orbit coupling [11], this interaction is taken into account for these calculations which are also in good agreement with experimental results [12]. As shown in Fig. 2.3, it can be observed that the Fermi level crosses the p bands near the L and T points, leading to electron and hole pockets, respectively. This confirms the semimetallic nature of bulk bismuth, with shallow pockets having Fermi energies of 27.2 meV and 10.8 meV for electrons and holes [13], respectively. Consequently, bismuth exhibits a low carrier density of $\sim 3 \times 10^{17}\mathrm{cm}^{-3}$, and the effective mass of electrons along the trigonal axis is only approximately 0.003 m_e with m_e being the electron mass.

2.1.4 Quantum Confinement

As mentioned in the previous section, charge carriers in the (111) plane of bismuth have a low effective mass and small Fermi energy. This results in the carriers having a long de Broglie wavelength λ_B that is on the order of 120 Å. This has significant implications for bismuth thin films grown in the (111) direction. When the film thickness approaches λ_B, charge carriers become confined, leading to substantial interference ef-

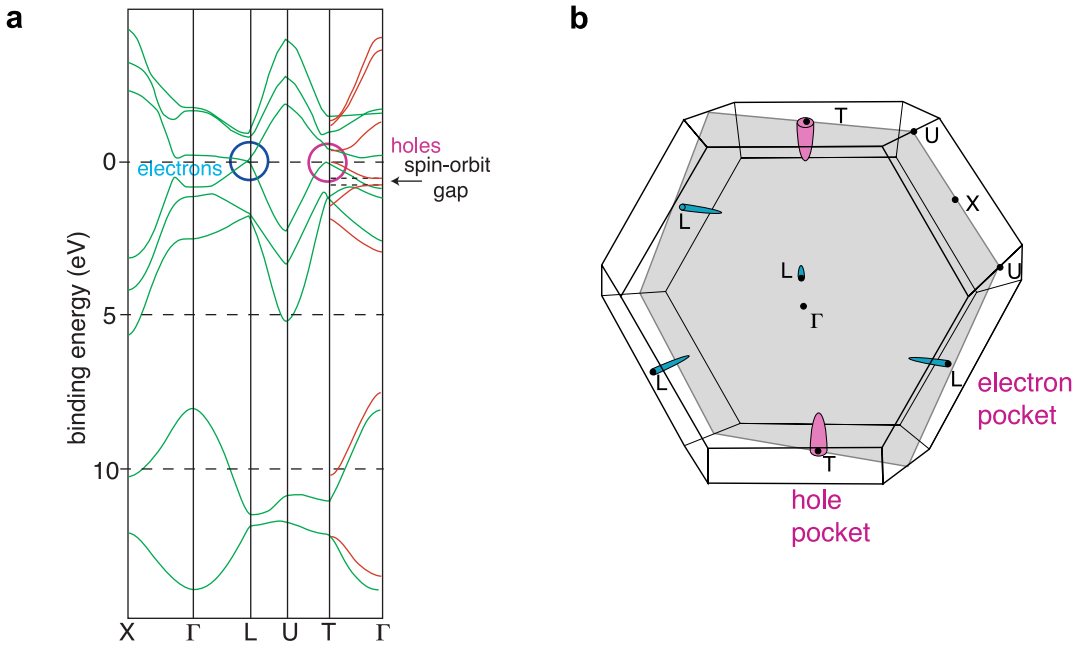

Figure 2.3: **a**. The corresponding electronic band structure according to tight-binding calculation (green) and first-principle calculation (red). **b**. Brillouin zone of bulk bismuth with depiction of the Fermi surface. The Γ-T line which corresponds to the trigonal or (111) surface is also shown. Both figures are reproduced with permission from Reference [12].

fects and the onset of quantization. These quantum confinement effects were predicted by Ogrin *et al.* [14], who argued that bismuth thin films grown in the (111) direction would be ideal for observing these phenomena due to their long λ_B and long mean free path on the order of couple of millimeters, which is crucial for interference effects [14]. Indeed, the long de Broglie wavelength minimizes the impact of surface imperfections and height variations, and oscillations in the transport properties of bismuth thin films have been observed when the film thickness is reduced to around 30 to 40 nm.

If the bulk band structure shown in Fig. 2.3 remains similar in thin films, reducing the film thickness could shift the electron energies at the L-point above the hole energies at the T-point. This would result in the creation of a small band gap, effectively turning bismuth into a semiconductor — a phenomenon known as the semimetal-to-semiconductor (SMSC) transition. Lutskii [15] and Sandomirskii [16] predicted that the critical thickness for this effect to occur is around 30 nm. Despite many efforts to confirm the SMSC transition, it has not yet been clearly observed. This is partly the

original goal of this thesis project which is to explore the SMSC transition through the mechanical exfoliation of bismuth thin films, in contrast to previous studies that focused on grown films.

2.1.5 Surface Electronic Band Structure

The lack of success in studying the SMSC transition in bismuth thin films can be attributed to the significant changes in the surface electronic band structure of bismuth compared to its bulk counterpart [12]. While bismuth has several surfaces, this section will focus solely on the (111) surface, which is the most relevant. The (111) direction is crucial because it has the weakest interlayer bonds, making it the natural cleavage plane. Additionally, the epitaxial growth of thin bismuth films predominantly occurs in the (111) direction. A schematic of the (111) direction bilayers are shown in Fig. 2.4.

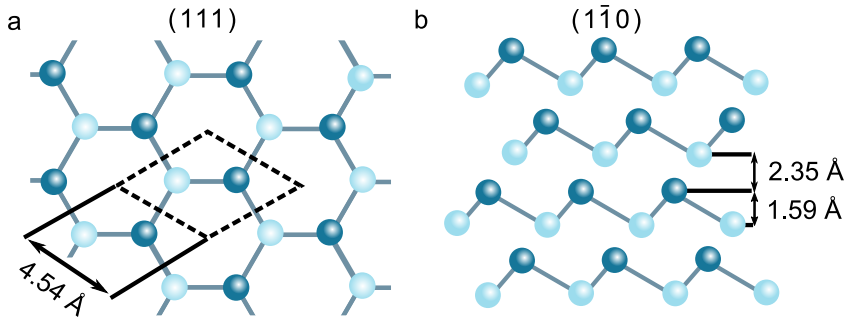

Figure 2.4: Layered bismuth crystal: **a**. top view of (111) and **b**. its side view, equivalent to (1$\bar{1}$0). Note that different color shadings are used to highlight the buckled honeycomb structure.

The electronic band structure of the (111) bismuth surface has been extensively studied and measured using angle-resolved photoemission spectroscopy (ARPES). The detailed findings of these studies are well documented [12], but the key conclusion is that the surface band structure differs significantly from the bulk. Notably, the surface states exhibit much more metallic behavior compared to the semimetallic nature of the bulk. This is surprising, given that the (111) surface geometry of bismuth remains largely unchanged and does not involve any dangling bonds. In fact, due to the weak interaction between bismuth bilayers in the (111) direction, the surface can be viewed as a separation between two bilayers, and thus one does not expect the surface band

structure to change substantially.

Through careful analysis of ARPES data, along with first-principle and tight-binding model calculations, it was revealed that the significant deviation between the bulk and surface band structures is due to the breaking of inversion symmetry at the surface and the strong spin-orbit interaction due to its high atomic mass, which leads to spin-splitting of the surface state bands [12]. These resulting metallic surface states become increasingly important as the film thickness is reduced, competing with quantum confinement effects. Consequently, this competition hinders the clear identification of the SMSC transition [12].

2.1.6 Transport Properties

The electrons and holes in bulk bismuth have been extensively studied, and it is now well understood that there are three electron valleys at the L-point and one hole valley at the T-point [17]. As a result, studying the transport properties of bulk bismuth necessitates a multi-carrier analysis for multi-valley systems. Interestingly, research on magnetoresistance in bulk bismuth even dates back to Kapitza, and it was through the study of bismuth that he uncovered what is now known as Kapitza's law of magnetoresistance [18].

Using a semiclassical approach, one can derive that the conductivity tensor $\hat{\sigma}$ for a single valley, single carrier system is, in the case of electrons,

$$\hat{\sigma}(B) = \frac{ne}{1 + \mu_x \mu_y B^2} \begin{pmatrix} \mu_x & -\mu_x \mu_y B \\ \mu_x \mu_y B & \mu_y \end{pmatrix}, \tag{2.1}$$

where n is the charge carrier density, e is the elementary charge, μ_x and μ_y are the anisotropic mobilities parallel or perpendicular to the current direction, and B is the magnetic field perpendicular to the sample. Using tensor inversion, we can then calcu-

late the resistivity tensor $\hat{\rho}$ that is given by

$$\hat{\rho}(B) = \frac{1}{ne\mu_x\mu_y}\begin{pmatrix} \mu_y & \mu_x\mu_y B \\ -\mu_x\mu_y B & \mu_x \end{pmatrix}, \tag{2.2}$$

where we find the trivial Hall resistivity $\rho_{xy} = \dfrac{B}{ne}$ and that the longitudinal resistivity is independent of the perpendicular field.

Equation (2.1) can be modified for holes by defining a hole carrier density p and the hole mobilities ν_x and ν_y. The electron and hole conductivities can then be added to obtain the total conductivity

$$\hat{\sigma}_{\text{total}}(B) = \hat{\sigma}_{\text{electron}}(B) + \hat{\sigma}_{\text{hole}}(B).$$

Omitting the detailed derivation for the tensor inversion, we present the key results from the calculation which implies that, at high magnetic field, the longitudinal and Hall resistivities are respectively given by [19]

$$\rho_{xx}(B) \simeq \frac{1}{e}\frac{\left(\frac{n}{\mu_y}+\frac{p}{\nu_y}\right)B^2}{\left(\frac{n}{\mu_y}+\frac{p}{\nu_y}\right)^2 + (n-p)^2B^2}, \tag{2.3}$$

$$\text{and} \qquad \rho_{xy}(B) \simeq \frac{B}{e}\frac{(n-p)B^2}{\left(\frac{n}{\mu_y}+\frac{p}{\nu_y}\right)^2 + (n-p)^2B^2}. \tag{2.4}$$

Hence, the transport behavior can be classified into two scenarios. When $n \neq p$, we can define a characteristic field

$$B^\star = \frac{n\nu_y + p\mu_y}{|n-p|\mu_y\nu_y}. \tag{2.5}$$

Above this critical field where $B \gg B^\star$, Eqs. (2.3) and (2.4) dictate that ρ_{xx} would become saturated while ρ_{xy} would scale linearly with B with a slope of $\dfrac{1}{(n-p)e}$. In bismuth, however, it turns out that the hole and electron densities are nearly identical, and

when $n = p$, Eq. (2.3) shows that ρ_{xx} would never saturate at high fields and continue to scale quadratically with B. This quadratic behavior remains valid even when considering a multi-valley, multi-carrier system [19]. It is important to note that, while the bulk electronic transport in bismuth is well understood, to date the surface transport properties are still being actively investigated.

2.1.7 Summary

Bismuth, one of the oldest metals known to human kind and one of the most extensively studied materials, led to many key discoveries in the history of solid-state physics. In its bulk form, bismuth has electron charge carriers with three valleys at the L-point and single-valley hole carriers at the T-point, and their transport is characterized by a B^2 dependence in the magnetoresistance. Bismuth thin films are an excellent platform for investigating quantum confinement effects including the SMSC transition. The latter, however, has not been clearly identified and remains controversial. It later became clear that the surface band structure differs significantly from the bulk, is highly metallic, and competes with confinement effects. Even as one of the best understood materials, bismuth continues to be actively researched today.

I would like to conclude this section by reemphasizing a key feature of bismuth. As one of the heaviest elements on the periodic table, it was long thought that bismuth is the highest atomic mass atom that is radioactively stable[1]. With such a high Z number, bismuth exhibits one of the highest spin-orbit couplings among all materials. This spin-orbit interaction is especially important in order to understand its surface band structure and was a key factor in elucidating the anomalously large diamagnetism observed in bismuth, which has puzzled physicists for decades [18]. Diamagnetism implies that bismuth must preserve time-reversal symmetry, and thus one would not expect bismuth to manifest the anomalous Hall effect typically found in ferromagnets, a phenomenon discussed in the following section.

[1]Interestingly, the half-life of its decay is about a billion times the age of the universe.

2.2 Anomalous Hall Effect

2.2.1 History

Ever since Edwin Hall's discovery of the ordinary Hall effect in 1879 [20], the study of transport properties in the presence of a magnetic field has evolved into a rich and ongoing field within solid-state physics. This family of Hall effects has remained vibrant for nearly 150 years, contributing to multiple Nobel Prizes, including those awarded for the integer quantum Hall effect (IQHE) and the fractional quantum Hall effect (FQHE). In 2016, the Nobel Prize in Physics was awarded to D. J. Thouless, F. D. M. Haldane, and J. M. Kosterlitz for their groundbreaking work on topological phase transitions and topological phases of matter, inspired by different types of quantum Hall effects. For these reasons, the ordinary Hall effect is often referred to as the "Queen" of solid-state physics [21].

In 1880, just a year after discovering the ordinary Hall effect, Edwin Hall observed that ferromagnetic materials responded to magnetic fields much more strongly than non-ferromagnetic materials, leading to what is now known as the anomalous Hall effect. While the ordinary Hall effect was quickly explained by the Lorentz force, the anomalous Hall effect proved more challenging to understand, as it appeared to depend on the specific materials being studied. Empirically, it was determined that the Hall resistivity follows the equation

$$\rho_{xy} = R_0 H_z + R_s M_z, \tag{2.6}$$

where R_0 is the ordinary Hall coefficient, H_z is the magnetic field perpendicular to the sample, M_z is the spontaneous magnetization and R_s is the coefficient for the anomalous Hall effect. Despite this empirical formula, the theoretical understanding of the second term in Eq. (2.6) was debated for over a century. Only with recent advances in topology and geometry, particularly the concept of Berry curvature [22], has the theory of the anomalous Hall effect become better established. However, even today,

our understanding of the anomalous Hall effect is still not complete. In Fig. 2.5**a** and **b**, we illustrate the ordinary Hall effect and the anomalous Hall effect, showing the sharp increase in ρ_{xy} at low fields, and finally in Fig. 2.5**c** the hysteresis loop for the AHE is sketched.

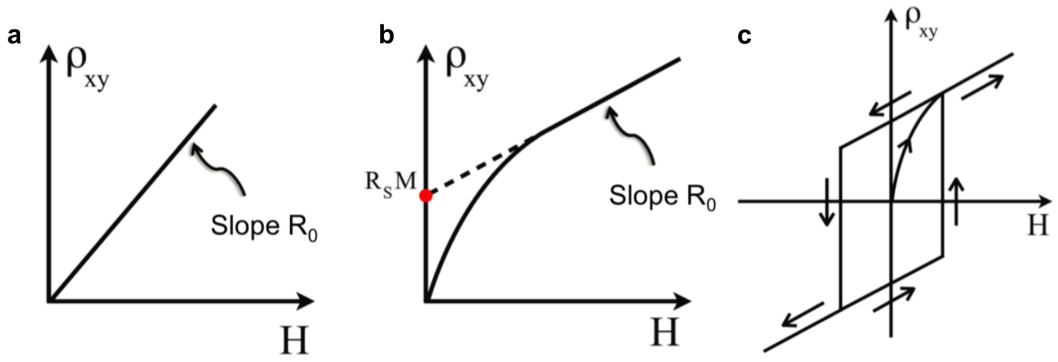

Figure 2.5: **a**. The ordinary Hall effect. **b**. The anomalous Hall effect described by the empiric equation mentioned in Eq. (2.6). **c**. The hysteresis loop for the anomalous Hall effect. All figures are reproduced with permission from Reference [23].

It is now understood that there are two types of contributions to the anomalous Hall effect. The intrinsic contribution, first formulated by Karplus and Luttinger (KL theory) in 1954 [24], is a consequence of the band structure where the electrons acquire an "anomalous" group velocity perpendicular to the applied electric field. This only depends on the crystal's Hamiltonian and is now understood in terms of the Berry curvature. The extrinsic contributions are scattering-based and involve two mechanisms: the skew scattering mechanism, proposed by J. Smit in 1955, which is due to the effective spin-orbit coupling of the electron or the impurity [25, 26], and the side-jump mechanism proposed by L. Berger in 1970, caused by the scattering of quasi-particles from spin-orbit coupled impurities [27].

In this section, we will discuss the different mechanisms of the anomalous Hall effect and how they are studied experimentally. Finally, since the intrinsic anomalous Hall effect is a precursor to the quantum anomalous Hall effect, the latter will also be briefly discussed.

2.2.2 Intrinsic Mechanism

R. Karplus and J. M. Luttinger were the first to propose a theory explaining the second term of Eq. (2.6) [24]. In order to include the effect of magnetic order, they expressed the total Hamiltonian as

$$H_{\text{total}} = H_0 + H_{SOI} + H_E, \tag{2.7}$$

where $H_0 = p^2/2m + V(\vec{r})$ is the crystal's Hamiltonian, $H_E = -e\vec{E} \cdot \vec{r}$ is the Hamiltonian for electrons in an external electric field, and finally the Hamiltonian due to spin-orbit interaction is

$$H_{SOI} = \frac{1}{4m^2c^2} \frac{(\vec{M} \times \boldsymbol{\nabla} V) \cdot \vec{p}}{M_0} \tag{2.8}$$

provided that the electrons are polarized in the direction of the magnetization. Note that m is the mass of electron, c is the speed of light, $\vec{M}$ is the magnetic moment, V is the potential, $\vec{p}$ is the momentum and M_0 is the magnitude of saturated magnetic moment. The total Hamiltonian given by Eq. (2.7) effectively describes the system with spin-orbit interaction as well as magnetic order.

Letting $\left|n, \vec{k}\right\rangle$ be the eigenstates for $H_0 + H_{SOI}$, then the matrix elements of H_E can be written as

$$\begin{aligned} \left\langle n, \vec{k} \right| H_E \left| n', \vec{k}' \right\rangle &= -eE \left\langle n, \vec{k} \right| r \left| n', \vec{k}' \right\rangle, \\ \left\langle n, \vec{k} \right| H_E \left| n', \vec{k}' \right\rangle &= -eE \left(i\delta_{n,n'} \frac{\partial}{\partial k_b} \delta_{\vec{k},\vec{k}'} + i\delta_{\vec{k},\vec{k}'} J_b^{n,n'}(\vec{k}) \right), \end{aligned} \tag{2.9}$$

where

$$J_b^{n,n'}(\vec{k}) = \int_\Omega \mathrm{d}V u_{n,\vec{k}}^*(\vec{r}) \frac{\partial}{\partial k_b} u_{n',\vec{k}}(\vec{r}) \tag{2.10}$$

is integrated over the entire crystal volume and $u(\vec{r})$ is the periodic function found in the Bloch solution. We denote $H_E = H_E^r + H_E^a$ for the two terms found in Eq. (2.9). The first term, H_E^r, is a regular periodic function, and hence is absorbed into $H_0 + H_{SOI}$

as a perturbation. Consequently, the total Hamiltonian defined previously in Eq. (2.7) becomes

$$H_T = (H_0 + H_{SOI} + H_E^r) + H_E^a \equiv H_p + H_E^a, \tag{2.11}$$

where H_E^a represents the second term in Eq. (2.9). The density matrix is then written as

$$\rho = \rho_0(H_p) + \rho_1, \tag{2.12}$$

where $\rho_0(H_p)$ is the finite-temperature equilibrium density matrix, and ρ_1 is the correction which yields only the ordinary conductivity [21, 24]. The term $\rho_0(H_p)$ gives rise to the AHE, and by evaluating the average "anomalous" velocity, one finds

$$v_{avg} = \mathrm{Tr}[\rho_0 v_a] = -ieE \sum_{n,\vec{k}} \left[\frac{\partial}{\partial \epsilon_{n,\vec{k}}} \rho_0(\epsilon_{n,\vec{k}}) \right] v_n(\vec{k}) J_a^{n,n}(\vec{k}), \tag{2.13}$$

where $\epsilon_{n,\vec{k}}$ is the energy and $v_n(\vec{k})$ is the velocity.

If the spin-orbit interaction energy is much less than the Fermi energy, $H_{SO} \ll \varepsilon_F$, as is in the d-bands [24], then Eq. (2.8) implies that the AHE response is linear in $|\vec{M}|$ which is consistent with the empiric equation found in Eq. (2.6). Importantly, in this case, Karplus and Luttinger found that Eq. (2.13) can be expressed as a vector equation

$$\vec{v}_{avg} = -\frac{eE}{m\Delta^2} \sum_{n,\vec{k}} \left[\frac{\partial}{\partial \epsilon_{n,\vec{k}}} \rho_0(\epsilon_{n,\vec{k}}) \right] v_n(\vec{k}) \vec{F}_{n,\vec{k}}, \tag{2.14}$$

where Δ is the average interband energy separation and $\vec{F}_{n,\vec{k}} = i \left\langle n, \vec{k} \right| [H_{SOI}, \vec{p}\,] \left| n, \vec{k} \right\rangle$ is the force. Finally, from this Karplus and Luttinger derived that

$$R_s = \frac{2e^2 H_{SO}}{m\Delta^2} \delta \left\langle \frac{m}{m^*} \right\rangle \rho^2, \tag{2.15}$$

where δ is the number of incomplete d-bands, m^* is the effective mass and ρ is the resistivity. In particular, this shows that the anomalous Hall term in Eq. (2.6) can be viewed as a consequence of nothing more than the intrinsic nature of the crystal structure. This

was controversial at the time since all scattering and impurity effects were neglected, and this will be discussed in Section 2.2.3.

Many electronic properties can now be understood through the recently developed concept of Berry curvature [22, 28]. Notably, it can be shown that the anomalous velocity vector for the n-th band in Eq. (2.14) can be written as [28]

$$\vec{v}_n(\vec{k}) = -\frac{e}{\hbar}\vec{E} \times \vec{\Omega}_n(\vec{k}), \tag{2.16}$$

where

$$\vec{\Omega}_n(\vec{k}) = i\left\langle \boldsymbol{\nabla} u_n(\vec{k}) \right| \times \left| \boldsymbol{\nabla} u_n(\vec{k}) \right\rangle \tag{2.17}$$

is the Berry curvature of the n-th band. This Berry curvature has important consequences to the electronic properties of materials and is complementary to the semiclassical framework of electron transport. Intuitively, the Berry curvature can be viewed as a magnetic field in the parameter space, and when it is integrated over a closed surface, it gives rise to quantized Chern numbers that captures the topology of the system, which, in turn, are responsible to the widely known quantum Hall phenomenon [28].

This reconciliation between Eq. (2.14) and Eq. (2.16) expands upon the original theory proposed by Karplus and Luttinger. In particular, the Hall conductivity,

$$\sigma_{xy} = \frac{e^2}{\hbar}\int \frac{\mathrm{d}\vec{k}}{(2\pi)^d} f(\epsilon_{\vec{k}})\Omega_{k_x,k_y}, \tag{2.18}$$

with $f(\epsilon_{\vec{k}})$ as the Fermi-Dirac distribution and d as the dimensionality of the system, can be viewed as an unquantized version of the quantum Hall effect, which is obtained by simply applying Eq. (2.16) to a two-dimensional band insulator. The latter yields

$$\sigma_{xy} = \frac{e^2}{2\pi h}\int \mathrm{d}\vec{k}\Omega_{k_x,k_y},$$

where the integration is over the Brillouin zone and gives only integer (Chern number) multiples of 2π. Thus, the intrinsic anomalous Hall effect can be considered an unquantized version, or a *precursor*, to the quantum anomalous Hall effect as we will further

discuss in Section 2.2.5.

Interestingly, the reformulation of the intrinsic AHE mechanism in terms of Berry curvature also facilitates symmetry analyses. Under time reversal, $\vec{v}_n \mapsto -\vec{v}_n$ and $\vec{k} \mapsto -\vec{k}$. Under spatial inversion symmetry, we would have additionally $\vec{E} \mapsto -\vec{E}$. From Eq. (2.16), these allow us to obtain

$$\vec{\Omega}_n(-\vec{k}) = -\vec{\Omega}_n(\vec{k}) \qquad \text{(Time reversal)}$$

$$\text{and} \qquad \vec{\Omega}_n(-\vec{k}) = \vec{\Omega}_n(\vec{k}). \qquad \text{(Spatial inversion)}$$

Together, it is obvious that the Berry curvature is zero whenever a system preserves both time-reversal symmetry and spatial inversion symmetry. On the other hand, if either of these symmetries is broken, the use of Eq. (2.16) becomes necessary to analyze the system [28].

2.2.3 Extrinsic Mechanisms

As previously mentioned, a significant limitation of the intrinsic mechanism is that it completely ignores the effects of scattering, focusing solely on the perfect crystal Hamiltonian. However, experiments have shown that the AHE can also occur in dilute Kondo systems, where magnetic impurities like Fe, Mn, or Cr are doped into a non-magnetic host such as Au or Cu [21], and therefore scattering effects should be relevant to the anomalous Hall effect. Furthermore, Eq. (2.15) from the KL theory suggests that the anomalous Hall resistivity ρ_{xy} would scale with ρ^2, whereas the skew scattering mechanism proposed by Smit predicts $\rho_{xy} \propto \rho$, which aligns with numerous experimental observations [21]. Throughout the latter half of the 20$^{\text{th}}$ century, extensive studies on the AHE were conducted across various systems, yet the debate over whether the AHE arises from a scattering-independent mechanism or extrinsic mechanisms remained unresolved. In this section, these scattering-dependent mechanisms will be discussed.

Semiclassically, the Boltzmann transport equation for the electron distribution $f(\vec{r}, \vec{k})$

is

$$\frac{\partial f}{\partial t} + \vec{v} \cdot \frac{\partial f}{\partial \vec{r}} + \frac{1}{\hbar}\vec{F} \cdot \frac{\partial f}{\partial \vec{k}} = \left(\frac{\partial f}{\partial t}\right)_{\text{collision}}, \tag{2.19}$$

where t is the time, $\vec{r}$ is the position, $\vec{v}$ is the velocity, $\vec{k}$ is the momentum, and $\vec{F} = -e\left(\vec{E} + \frac{\vec{v}}{c} \times \vec{H}\right)$ is the Lorentz force. The collision term $\left(\frac{\partial f}{\partial t}\right)_{\text{collision}}$ is related to the transition probability $W_{\vec{k}\to\vec{k}'}$ between two states $\vec{k}$ and $\vec{k}'$. Specifically, we have

$$\left(\frac{\partial f}{\partial t}\right)_{\text{collision}} = \sum_{\vec{k}'} \left[W_{\vec{k}'\to\vec{k}} f(\vec{k}')(1 - f(\vec{k})) - W_{\vec{k}\to\vec{k}'} f(\vec{k})(1 - f(\vec{k}'))\right]. \tag{2.20}$$

According to Fermi's golden-rule, the transition probabilities are symmetric since

$$W_{\vec{k}'\to\vec{k}} = \frac{2\pi}{\hbar}\left|\left\langle \vec{k} \right| V \left| \vec{k}' \right\rangle\right|^2 \delta(E_{\vec{k}} - E_{\vec{k}'}) = W_{\vec{k}\to\vec{k}'},$$

where V is the perturbation inducing the transition. However, if spin-orbit interaction is included, then the scattering would depend on the direction of the magnetization. Notably, the asymmetric part (hence the name *skew scattering*) of the transition probability is

$$W^A_{\vec{k}\to\vec{k}'} = -\frac{1}{\tau_A}\vec{k} \times \vec{k}' \cdot \vec{M}_s, \tag{2.21}$$

where τ_A is the transport lifetime and $\vec{M}_s$ is the spontaneous magnetization. It can be observed from Eq. (2.21) that the scattered carrier has a momentum $\vec{k}'$ perpendicular to both the original momentum $\vec{k}$ and the magnetization $\vec{M}_s$, leading to a transverse current proportional to the longitudinal current. As a result, both conductivities should be proportional to the transport lifetime and therefore proportional to the longitudinal resistivity, *i.e.* $\sigma_{xy} \propto \tau \propto \rho^{-1}$ and $\sigma_{xx} \propto \tau \propto \rho^{-1}$. Importantly, because the Hall resistivity is related to the conductivity via tensor inversion, we have $\rho_{xy} \simeq \sigma_{xy}\rho^2 \propto \rho$, thus confirming the scaling mentioned previously.

Smit also investigated other potential contributions to the anomalous Hall effect. In particular, he examined how a Gaussian wave packet would scatter off a spherical impurity in the presence of spin-orbit interactions [26]. This analysis predicted a transverse

anomalous velocity due to an external field. However, Smit argued that this extrinsic contribution would cancel out the intrinsic contribution, and as such it was rejected by Smit. Today, we know that this is not the case in materials with more complex band structures [21, 29].

In 1964, L. Berger reintroduced this term and called it the side-jump mechanism [27, 30]. Taking the spherical potential for the impurity as [21]

$$V(r) = \begin{cases} \frac{\hbar^2}{2m}(k^2 - k'^2) & r < R \\ 0 & r \geq R \end{cases} \tag{2.22}$$

and the spin-orbit term

$$H_{SOI} = \frac{1}{2m^2c^2}\left(\frac{1}{r}\right)\frac{\partial V}{\partial r} S_z L_z, \tag{2.23}$$

where $\hbar$ is the reduced Planck constant, m the mass of the carrier, k, k' are the incident and scattered momenta, R is the radius of the spherical potential well, S_z and L_z are respectively the spin and orbital angular momentum. Berger calculated that the wave-packet acquires a small displacement Δy (hence the name *side-jump*). Specifically, it was found that

$$\Delta y = \frac{1}{6}\frac{k\hbar^2}{m^2c^2} = \frac{1}{6}k\lambda_C^2,$$

where $\lambda_C = \hbar/mc$ is the Compton wavelength. In typical metals, $\Delta y \sim 10^{-16}$ m, but in dilute alloys, the band structure enhances the effective spin-orbit effects, yielding $\Delta y \sim 10^{-11}$ m [27]. At this scale, the side-jump becomes observable and contributes to the anomalous Hall effect.

Interestingly, the side-jump mechanism of the AHE is fully compatible with the intrinsic mechanism. It can be viewed as a quasi-particle experiencing an electric field due to an impurity, as long as the impurity's potential is "smooth" enough. Consequently, this also leads to an anomalous velocity [21, 29]. In terms of the Berry curvature, the intrinsic mechanism requires the integration of the entire Fermi sea while for the side-

jump mechanism, Sinitsyn *et al.* showed that it would only depend on the properties close to the Fermi surface [31]. Given this fundamental similarity between the intrinsic and the side-jump mechanisms, early studies of the AHE could overlook the effect of impurities, allowing Karplus and Luttinger to develop the first theoretical model for the AHE.

We close this section by highlighting an important feature of the side-jump mechanism. Although it arises form scattering, the side-jump mechanism is independent of the transport lifetime τ, and hence has the same dependence on the longitudinal resistivity as the intrinsic KL theory, namely, proportional to ρ^2. This similarity makes it challenging to experimentally distinguish the intrinsic and side-jump mechanisms, which is the topic of Section 2.2.4 where we discuss how to distinguish the different types of the AHE.

2.2.4 Parsing the Anomalous Hall Effect

So far, we have established that the intrinsic and side-jump mechanisms yield $\rho_{xy} \propto \rho^2$ whereas Smit's skew-scattering mechanism gives $\rho_{xy} \propto \rho$. This is indeed an effective and powerful way to analyze the different mechanisms, and experiments also appear to consistently produce Hall resistivity in the form of $\rho_{xy} \propto \rho^\gamma$ with either $\gamma = 1$ or $\gamma = 2$ [21]. Experimentally, however, the differentiation between the intrinsic KL mechanism and the extrinsic side-jump mechanism is far less straightforward.

While studying various thicknesses of Fe films, Tian *et al.* [32] proposed to analyze the longitudinal resistance ρ dependence by including the residual resistivity ρ_0. Under the assumption that phonon can be neglected, which is relevant to the bismuth system as demonstrated in Chapter 5, the anomalous Hall resistivity ρ_{AHE}, defined as the y-intercept of a linear fit to the saturated part of ρ_{xy} vs H (which equals $R_s M_z$ in Eq. (2.6)) was empirically found to be [32]

$$\rho_{\mathrm{AHE}} = (\alpha\rho_0 + \beta\rho_0^2) + b\rho_{xx}^2, \tag{2.24}$$

where ρ_{xx} is the longitudinal resistivity and α, β and b are parameters for the skew scattering, side-jump and intrinsic terms, respectively. This allows experimentalists to empirically study the different AHE contributions provided that ρ_0 can be tuned by, for example, changing the film thickness. Equivalently, Eq. (2.24) can be rewritten in terms of the conductivities as

$$\sigma_{\mathrm{AHE}} = -(\alpha\sigma_0^{-1} + \beta\rho_0^{-2})\sigma_{xx}^2 - b, \tag{2.25}$$

provided that $\rho_{xx} \gg \rho_{\mathrm{AHE}}$, as it is the case in bismuth (see Chapter 4 and Chapter 5). This equation has the advantage that the b term for the intrinsic contribution can be easily isolated as the y-intercept. In the literature, conductivity is also the preferred notation for analyzing the AHE as the different conductivity contributions would simply be expressed as a sum

$$\sigma_{\text{total}} = \sigma_{\text{int}} + \sigma_{\text{skew}} + \sigma_{\text{s-j}},$$

where σ_{total} is the total anomalous Hall conductivity, σ_{int} is the intrinsic contribution, σ_{skew} is the skew scattering contribution and $\sigma_{\text{s-j}}$ is the side-jump contribution.

Until now, experiments on the AHE have been conducted for well over a century, and vast amount of data on diverse materials were collected. From these, three regimes with different dominant mechanisms have been identified [21]:

(i) the high conductivity regime ($\sigma_{xx} > 10^6\ \Omega^{-1}\,\mathrm{cm}^{-1}$): $\sigma_{\mathrm{AHE}} \propto \sigma_{xx}$ and thus the skew scattering mechanism dominates,

(ii) the good-metal regime ($10^4\ \Omega^{-1}\,\mathrm{cm}^{-1} < \sigma_{xx} < 10^6\ \Omega^{-1}\,\mathrm{cm}^{-1}$): σ_{AHE} remains constant, and thus the intrinsic or side-jump mechanisms dominate,

(iii) the bad-metal–hopping regime ($\sigma_{xx} < 10^4\ \Omega^{-1}\,\mathrm{cm}^{-1}$): $\sigma_{\mathrm{AHE}} \propto \sigma_{xx}^{1.6-1.8}$, in which case a minimal model cannot describe the AHE well.

While these identified regimes based on the longitudinal conductivities provide a good way to predict the type of AHE in different materials, formally the ρ_{xy}^{AHE} ($\sigma_{xy}^{\mathrm{AHE}}$)

dependence on ρ_{xx} (σ_{xx}) found in Eqs. (2.24) and (2.25) should be carefully studied for a given system. Alternatively, the temperature dependence also gives an excellent indication of the dominant mechanism at play. If phonons or impurity scattering were present, then σ_{AHE} should have a strong temperature dependence. On the other hand, the intrinsic AHE should not depend on the temperature. Details of the AHE temperature dependence is thoroughly discussed in Chapter 5 and Chapter 6.

2.2.5 Quantum Anomalous Hall Effect

We now return briefly to the intrinsic mechanism of the AHE. As this intrinsic contribution is a property of the Berry curvature, it can lead to the quantized version of the anomalous Hall effect in the 2D limit. When the Fermi level lies within a gap of the bulk band structure, and the band exhibits a non-zero Berry curvature, the intrinsic mechanism does not contribute to the conductivity but produces a quantized contribution on the edge in units of e^2/h at $T = 0$ [21, 29]. If the system is bulk and not in the 2D limit, it can be viewed as a stack of many 2D layers, the anomalous Hall conductivity would then be $\sim e^2/(ha)$ where a is the lattice constant. This result is consistent with numerous experimental observations [21].

In 1988, Haldane proposed a toy model for realizing the quantum anomalous Hall effect (QAHE) which partly led to his winning of the Nobel prize in 2016. In this model, he examined a 2D honeycomb lattice with broken time-reversal symmetry. When the system exhibits strong spin-orbit interaction, the anomalous Hall effect would become quantized [33]. Interestingly, pure bismuth in the 2D limit known as bismuthene, possesses a honeycomb structure similar to graphene, except it is buckled as illustrated in Fig. 2.4. Additionally, bismuth, being a heavy atom with high atomic number Z, has one of the highest spin-orbit coupling among all elements. This raises the question of whether bismuthene could be a suitable platform for exploring the quantum anomalous Hall effect, despite it appears to be missing the necessary condition of time-reversal symmetry breaking. This will be further discussed in Chapter 6.

2.2.6 Summary

Despite over a century of research, it was only with recent advances in topology that we began to have a strong grasp of the mechanisms responsible for the anomalous Hall effect. In particular, the Berry curvature is crucial for understanding the intrinsic mechanism of the AHE. This mechanism only depends on the crystal's Hamiltonian and serves as a precursor to the quantum anomalous Hall effect. Conversely, the side-jump mechanism, while fundamentally compatible with the intrinsic contribution, can be seen as arising from a quasi-particle influenced by an electric field due to impurities. Both mechanisms are independent of the transport lifetime τ, resulting in $\rho_{xy} \propto \rho^2$, whereas the skew scattering mechanism yields $\rho_{xy} \propto \rho$ due to asymmetries in the transition probability.

Identifying the exact mechanism at play can be challenging, especially given the identical ρ dependence of both the intrinsic and side-jump mechanisms. However, as discussed in Section 2.2.4, researchers have been able to distinguish regimes where skew scattering dominates from those where intrinsic and/or side-jump contributions are more significant, based on the value of σ_{xx} and the temperature dependence of ρ_{AHE}. Importantly, in the scenario where phonons can be neglected, the parameters for each mechanism can be fully extracted from Eq. (2.24) or Eq. (2.25). Parsing the AHE represents only one of the experimental challenges, some of which will be addressed in the next section as we shift the focus to transport measurements.

2.3 Transport Measurement

While textbooks often provide a solid theoretical foundation on a given topic, mastering measurement techniques is typically a skill developed over time in the laboratory, often through hands-on experience and overcoming practical challenges. In this section, we examine the van der Pauw geometry and the Onsager reciprocity theorem, both crucial for accurately isolating the Hall and longitudinal signals that were experimentally obscured in our bismuth device.

2.3.1 van der Pauw Geometry

A narrow Hall bar is frequently used to simultaneously measure the Hall effect and resistivity of a sample. However, this method can be impractical as it requires at least six contacts and typically demands an elongated geometry. In contrast, the van der Pauw geometry allows for the measurement of both the Hall effect and resistivity using only four contacts on a sample of arbitrary shape. Consequently, the van der Pauw method is often preferred for smaller samples, or when practical considerations make the Hall bar approach less feasible. Some of the common van der Pauw geometries are shown in Fig. 2.6.

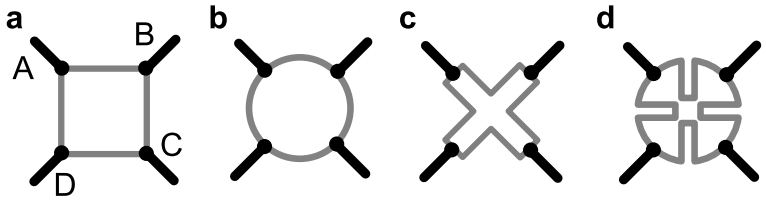

Figure 2.6: Common van der Pauw geometries: **a**. square, **b**. circle, **c**. Greek cross and **d**. cloverleaf. Each contact is labeled with the letter A, B, C or D as illustrated in **a**.

With this approach, the resistivity can be extracted through the formula [34]

$$\rho = \frac{\pi t}{\ln 2} \frac{R_{AB,CD} + R_{BC,DA}}{2} f \tag{2.26}$$

where t is the thickness, $R_{AB,CD}$ ($R_{BC,DA}$) is the measured four-terminal resistance under the notation $R_{I+I-,V+V-}$[2] and f is a prefactor defined by the solution of the equation

$$\cosh\left(\frac{\ln 2}{f} \frac{R_{AB,CD}/R_{BC,DA} - 1}{R_{AB,CD}/R_{BC,DA} + 1}\right) = \frac{1}{2} e^{\ln 2/f}. \tag{2.27}$$

Note that $R_{AB,CD}$ and $R_{BC,DA}$ are related by a 90-degree rotation. While the van der Pauw method minimizes the importance of sample geometry, it requires multiple measurements to determine the resistivity. Additionally, specific conditions must be met for this method to be applicable: the contacts must be placed on the sample's perimeter

[2]Thus, $R_{AB,CD} = V_{CD}/I_{AB}$ and $R_{BC,DA} = V_{DA}/I_{BC}$.

and be very small relative to the sample size, the sample must not contain holes, and its thickness must be uniform. Some of these requirements can be relaxed. For example, different pre-factors can be introduced when the contacts are large compared to the sample size [35,36]. Recent developments have also addressed cases with a single hole in the van der Pauw geometry [37, 38]. Nevertheless, deviations from these ideal constraints generally introduce some error into the van der Pauw method.

2.3.2 Onsager's Reciprocity Relations

In van der Pauw geometry, another challenge arises when contacts are not infinitesimally small and/or not placed on the sample's perimeter - this can result in the mixing of the measured longitudinal and Hall voltages. However, Onsager's reciprocity relations provide a powerful tool to separate them.

Onsager developed a series of reciprocal relations by combining the theory of fluctuations with time-reversal considerations [39]. These relations are of paramount importance, enabling the thermodynamic study of irreversible processes and finding applications across numerous fields. For this reason, Onsager's relations are sometimes referred to as the "Fourth Law of Thermodynamics", a discovery that earned Lars Onsager the Nobel Prize in Chemistry in 1968.

Among the many applications of Onsager's reciprocity theorem, Meixner applied the concept to electrical conduction and made extensive studies in this area [40]. For Hall and resistivity measurements in an ohmic system, it is well understood that inverting the current and voltage probes in a four-terminal measurement transposes the measured resistance tensor, as dictated by the reciprocity relation [41]. Mathematically, this means

$$R(B) = \begin{pmatrix} R_{xx} & R_{xy} \\ -R_{xy} & R_{xx} \end{pmatrix} \quad \xrightarrow[I_+ \leftrightarrow V_+]{V_- \leftrightarrow I_-} \quad \begin{pmatrix} R_{xx} & -R_{xy} \\ R_{xy} & R_{xx} \end{pmatrix}.$$

As a result, provided that we make both measurements for the Onsager pair (upon

interchanging $I_+ \leftrightarrow V_+$ and $V_- \leftrightarrow I_-$), the longitudinal resistance R_{xx} and the Hall resistance R_{xy} can be separated upon symmetrization and anti-symmetrization giving

$$R_{xx} = \frac{R + R'}{2},$$
$$\text{and} \qquad R_{xy} = \frac{R - R'}{2},$$

where R and R' form an Onsager reciprocal pair. In contrast to the usual symmetrization and anti-symmetrization methods, which rely on the evenness and oddness of the resistances, $R_{xx}(B) = R_{xx}(-B)$ and $R_{xy}(B) = -R_{xy}(-B)$, the Onsager reciprocal relations offer a more powerful framework for capturing behaviors across the entire B-field [41–43].

2.4 Summary

In conclusion, bismuth remains an exciting platform for solid-state physics to this day. The historical snapshots presented in Section 2.1 highlight effects that are well understood within established theoretical frameworks. However, some phenomena are still the subject of active research. One such example is the semimetal-to-semiconductor transition,whose understanding presents challenges due to the interplay between quantum confinement effects and changes in the surface band structure of bismuth.

Similarly, more experiments are needed to fully understand the anomalous Hall effect. An extreme case of the intrinsic AHE is the quantum anomalous Hall effect, which, as predicted by Haldane, can occur in a honeycomb system with time-reversal symmetry breaking. At first glance, bismuth, which is diamagnetic in nature, seems an unlikely candidate for exploring the QAHE. However, as we will demonstrate in Chapter 4 and Chapter 5, we have unambiguously observed the AHE in thin bismuth flakes. This suggests the existence of a hidden mechanism for breaking time-reversal symmetry, indicating that bismuth could indeed be a platform for realizing the QAHE.

In the following manuscript-based chapters, Chapter 3 details the fabrication of the

thin bismuth flakes, Chapter 4 presents our first report on the anomalous Hall effect observed in these flakes, and finally in Chapter 5, we demonstrate that the observed AHE in bismuth is surprisingly temperature independent.

3

Exfoliation of Thin Bismuth Flakes

3.1 Introduction

The existence of graphene was predicted decades before its successful isolation in 2004 [44]. This breakthrough with graphene opened the door to the world of 2D materials. Since then, there has been an enormous effort to produce and study various 2D materials, as their properties can be "exotic" and significantly different from their bulk counterparts. Generally, the fabrication of these single-layer materials can follow either top-down or bottom-up approaches. The state-of-the-art method for bottom-up fabrication is the molecular beam epitaxy (MBE), which provides exceptional control over thickness and composition at the atomic level. Meanwhile, other bottom-up techniques like chemical vapor deposition (CVD) and physical vapor deposition (PVD) offer better scalability, though achieving uniform film thickness can often be challenging [45].

These bottom-up approaches can be financially burdensome for researchers and may require an incredible amount of time to perfect the optimal parameters. In contrast, the top-down approach involves exfoliating a bulk crystal down to atomic layer thickness. A prime example is the adhesive-tape method first used to exfoliate graphene. Due to the low van der Waals (vdW) forces between graphene layers, the adhesion of the tape is strong enough to separate individual layers. Surprisingly, even such a simple technique can produce materials in the 2D limit of exceptionally high quality.

This technique has been used to fabricate numerous 2D materials, including the successful isolation of phosphorene in 2014, making it the second 2D elemental allotrope produced after graphene [46]. As seen in Section 2.1, bulk bismuth with a surface in the (111) direction shares a similar honeycomb structure with graphene and phosphorene. The (111) surface is the natural cleavage plane, where the layers are bonded by van der Waals forces. However, as discussed in Section 3.2.2, the increased atomic size of bismuth leads to greater polarizability, making the adhesive-tape mechanical exfoliation method inefficient for isolating thin layers of bismuth.

Several research groups have explored other techniques, such as liquid exfoliation, through which bismuthene has been successfully prepared [47–50]. Interestingly, some highly creative methods were employed, including the use of a kitchen blender [49]. However, these approaches can pose challenges due to the chemicals involved. When the surface-to-volume ratio is significantly increased, the thin layers can become highly reactive. This is the case of phosphorene, which rapidly transforms into phosphoric acid upon exposure to air. For this reason, traditional mechanical exfoliation is preferred, especially in environments that can be carefully controlled such as with the use of a glovebox.

In this chapter, we present the manuscript entitled “Method of mechanical exfoliation of bismuth with micro-trench structures” which proposes the design of a new mechanical exfoliation method that can be adapted for use in an isolated environment. Note that the full manuscript below is identical to the published version in the *Journal of Applied Physics* [52]. The figure labels and reference numberings are also aligned with

those of the published manuscript and are independent from the rest of the thesis. The Supplemental Information of the manuscript is presented in Appendix A.

3.2 Manuscript

3.2.1 Abstract

The discovery of graphene led to a burst in search for 2D materials originating from layered atomic crystals coupled by van der Waals force. While bulk bismuth crystals share this layered crystal structure, unlike other group V members of the periodic table, its interlayer bonds are stronger such that traditional mechanical cleavage and exfoliation techniques have shown to be inefficient. In this work, we present a novel mechanical cleavage method for exfoliating bismuth by utilizing the stress concentration effect induced by micro-trench SiO_2 structures. As a result, the exfoliated bismuth flakes can achieve thicknesses down to the sub-10 nm range which are analyzed by AFM and Raman spectroscopy.

3.2.2 Introduction

Since the discovery of graphene earlier this century [1], two dimensional (2D) materials have been intensively studied and have become a topic of broad and current interest. In 2014, black phosphorus, a group V member, was successfully exfoliated and as such is the second elemental allotrope that can be exfoliated mechanically [2–6]. Similar to phosphorus, bismuth is also a member of the group V column and shares a similar layered crystal structure, as shown in Fig. 1. In particular, bismuth has attracted more attention in solid state physics, as it displays noteworthy features, such as extremely large diamagnetism [7], high Seebeck coefficient [8, 9] and outstanding electronic transport properties [10–13]. Most notably, the Shubnikov-de Haas oscillation and de Haas-van Alphen effect were also first observed in bismuth [14, 15]. However, most of these interesting properties have been only explored in bulk bismuth before the successful growth of single-layer bismuthene on SiC substrate in 2017 [16], and the free-standing

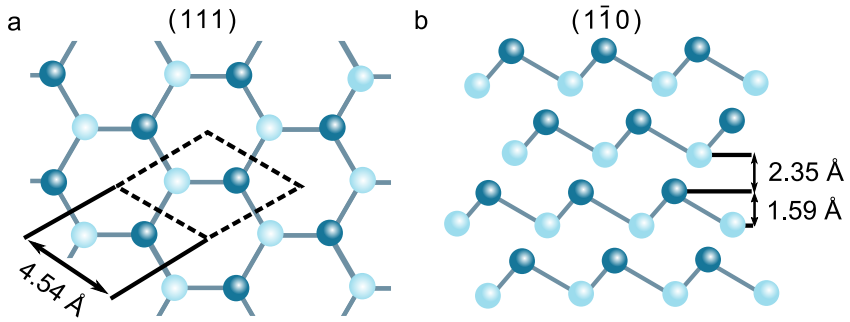

Figure 1: Layered bismuth crystal: (a) top view of (111) and (b) its side view, equivalent to (1$\bar{1}$0). Note that different color shadings are used to highlight the buckled honeycomb structure [11].

unsupported bismuthene with the buckled honeycomb structure was only grown in 2020 [17]. Such a breakthrough opens doors for experimenting the electronic transport properties of 2D bismuthene since it has been predicted and shown to manifest new properties such as being a higher order topological insulator (HOTI) [18, 19] and to host intrinsic superconductivity at temperatures below $T_c \approx 0.5$ mK [20].

Between its bulk form and its 2D form, bismuth thin film demonstrates tunable band gap due to the quantum confinement effects [21, 22]. It has been theoretically predicted and experimentally proved that, a transition from the semimetal phase with negative gap to the semiconductor phase with positive gap occurs as bismuth film's thickness reaches smaller than $\sim 30\,\mathrm{nm}$ [23–25]. In spite of these advances, as of today no transport measurements have been carefully performed in the thin film regime because of the difficulties in fabrication such as oxidization and small size of the exfoliated flakes.

To obtain bismuth thin flakes, one would naturally expect to exfoliate bismuth in a similar fashion as its partners in the group V given that they share similar crystal structures. Unfortunately, conventional mechanical exfoliation/cleavage fails for the bismuth samples, because the van der Waals (vdW) force increases with increasing atomic weight. This is exemplified by He-He (0.0218 kcal/mol) versus Xe-Xe (0.5614 kcal/mol) vdW interactions [26]. Furthermore, the Bi-Bi covalent bond (197 kJ/mol) is weaker than the P-P covalent bond (490 kJ/mol) [27], and combined with the increas-

ing vdW force, the anisotropy in bond strength is reduced which makes the exfoliation process difficult. Indeed, almost all the high quality samples have been prepared through molecular beam epitaxy (MBE) [28–33], but MBE growth requires significantly more complex infrastructure than exfoliation based methods. Conversely, recently reported exfoliation techniques for bismuth use liquid sonication which is detrimental to the electronic properties due to high humidity and oxidation [34, 35].

In this work, we improve the traditional mechanical cleavage technique ("drawing with chalk on a blackboard" [36] or the scotch tape method [1]) by fabricating micro-trench structures used as stress concentration area to break the bonds between bismuth atomic layers. The principle of this process is similar to a "cheese grater", where flakes are broken off as the bulk crystal is pushed against the micro-trench structures. Our experiment demonstrates that this exfoliation technique can be used to obtain ultra-thin bismuth flakes as thin as 2 nm.

3.2.3 Exfoliation Method

As mentioned, to exfoliate bismuth, it is necessary to mechanically break the strong bonds between its atomic layers. To break the interlayer van der Waals bonds, we utilize the micro-structures to locally induce a stress concentration which then produces inter-layer fractures in the bismuth. The fabricated device used to perform such exfoliation task is hence composed of two parts: a micro-trenched SiO_2 "file" or "grater", and a metal pen used to hold the bulk bismuth crystal. The latter is scratched against the file through pressure applied by the metal pen as depicted in Fig. 2. Note that the hardness of bismuth, 2.25 Mohs [37], is significantly lower than that of silica, 7.0 Mohs, enabling SiO_2 to be an effective medium to scratch bismuth.

A pen was fabricated to hold a small bismuth crystal at its tip. It is important to note that we prepare the bismuth crystal in a way to carefully to control the orientation of the exfoliated flakes. This is achieved by cutting the bismuth sample from a larger bismuth single crystal while ensuring the top and bottom surfaces are both (111) cleavage planes.

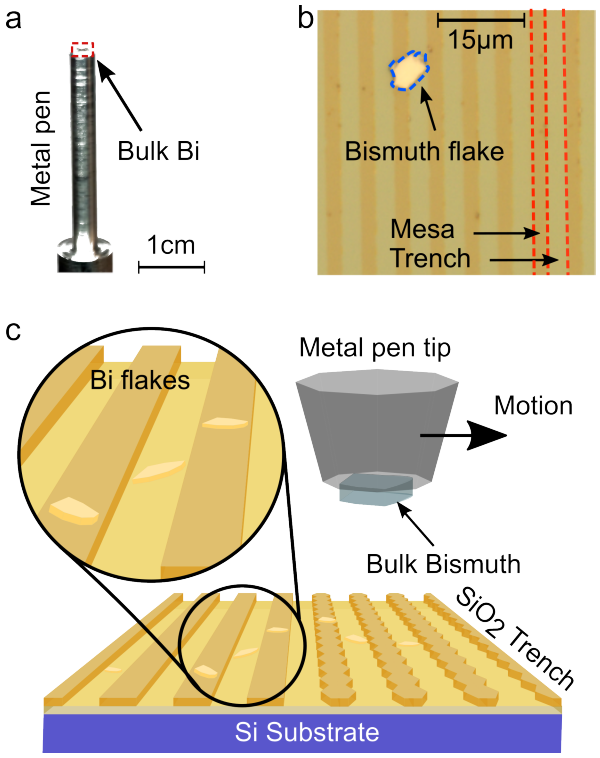

Figure 2: (a) Photograph of the metal pen with a bulk bismuth single crystal sample glued to its tip. (b) Photograph of the micro-trench structure on the SiO_2 substrate. The exfoliated flake is traced in blue and the red lines indicate the trench and mesa. (c) Schematic drawing which describes the exfoliation process: the metal pen holding the bismuth sample is scratched against the hard SiO_2 micro-trench structure in a way to break the bismuth into thin flakes.

The small sample is then glued to the tip of the metal pen with a thin layer of epoxy glue. With this pen-shaped sample holder, we can conveniently control the contact pressure and the scratching speed during the exfoliation process. In our case, the bulk bismuth has a contact area of 3 mm by 3 mm and the force applied by hand is estimated to be 10 to 30 N, yielding a mean pressure of 1 to 3 MPa, which can be increased in localized regions by the micro-trenches and bismuth surface topography. To ensure the exfoliated flakes are free of oxide, the entire process of the exfoliation is performed in a nitrogen-filled glovebox (with water and O_2 concentrations less than 1 ppm). Atomic force microscopy (AFM) was carried out in this nitrogen environment, and the substrate was spincoated with polymethylmethacrylate (PMMA) before exposing the flakes to air for Raman spectroscopy in order to prevent possible oxidation. The details of these characterizations are discussed later in this article.

An optical microscope image of the micro-trench structures on the SiO_2 file and an exfoliated flake are shown in Fig. 2(b). The mesa and trench part are shown between the dotted red lines. To form these trenched structures, a 425 μm Si wafer with 300 nm SiO_2 thermal oxidation layer was used. The trenches were then patterned with conventional photolithography on the oxide layer using Microposit® S1813 positive photoresist spun at 4000 RPM for 30 s. With the developed photoresist as a mask, the selected region of the oxide layer was partially removed with reactive ion etching (RIE). The recipe used was 100 mTorr pressure with CHF_3 at 45 sccm, CF_4 at 7 sccm, Ar at 70 sccm and power of 720 W for 5 s, yielding a trench of 25 nm deep. The remaining photoresist was removed with Microposit® Remover 1165, and the micro-trench structures are then completed. In our experiments, we designed two types of trenches: straight-edge and jagged-edge, both shown in the schematic in Fig. 2(c). The depths of these trenches are fixed at 25 nm and their widths vary from 3 μm to 100 μm.

Figure 2(c) also summarizes the entire exfoliation process. The key feature of the trenched micro-structures for bismuth exfoliation is the stress concentration effect. As the SiO_2 is much harder than bismuth, the bismuth surface in contact with the trenched micro-structures is deformed as the metal pen is pushed against the fabricated file with appropriate pressure, and the area contacting the trench edge then becomes a stress concentrated region. Fig. 3(b) and Fig. 3(c) illustrate this described mechanical process for the straight-edge and jagged-edge types of trenches respectively. It is important to note that the jagged-edge trenches can induce higher stress concentration on the bismuth surface than the straight-edge trenches. This is because the sharp corners of the jagged-edge trenches can concentrate the stress to a point in addition to the stress concentration lines of the straight-edge trenches. Finally, as illustrated in Fig. 3(a), while the bismuth held by the metal pen moves across the trenches, the stress concentration lines successively scan the bismuth surface, and this induces numerous fractures near the surface. From the perspective of damage mechanics, these fractures are most likely to be formed along the (111) cleavage plane, which, as we have carefully arranged, is parallel to the bismuth surface. As a consequence, the stress concentrates in the fractures, and hence

thin layers of bismuth flakes are stripped away from the bulk sample, leaving a trace of bismuth films with thicknesses varying from 10 nanometers to several hundred nanometers. This process is analogous to writing with a carbon lead pencil, except the lead is bulk bismuth crystal instead of graphite and the paper has a micro-trench file.

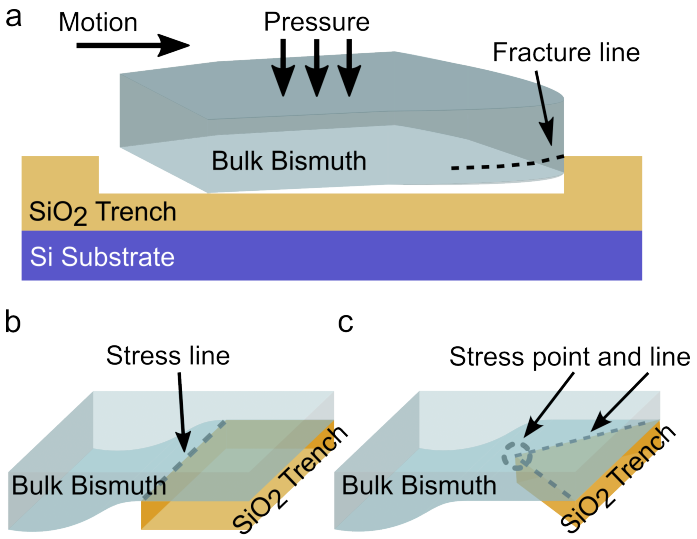

Figure 3: (a) Schematic of the bismuth crystal scratching against the SiO_2 micro-trench structure. Microscopically, the stress is concentrated near the trench edge and fractures the bulk crystal. (b) Bismuth crystal pressed against a straight-edge trench which results in a stress concentration line. (c) Bismuth crystal pressed against a jagged-edge trench which results in a stress concentration point.

3.2.4 Result and Discussion

Per the exfoliation method described above, we succeeded to produce bismuth flakes of various sizes and thicknesses. While our method is effective for producing thin bismuth flakes, we observed no difference in the performance of the straight-edge and jagged-edge types of trenches. We attribute this observation to the fact that the edges only introduce fractures to the bulk crystal and do not shave the crystal directly. Furthermore, the exfoliated flakes do not prefer to fall into the trenches and are observed in the trenches as well as on the mesas. This also affirms that fractures are only introduced by the micro-trench structures and that the actual exfoliation of flakes is responsible by the "writing" process. Fig. 2(b) shows the optical microscope image of a typical flake on the SiO_2 file. Note that this flake has a height over 100 nm giving a good visibility, and

thus can be easily identified with an optical microscope. In the *Supplemental Material*, we calculate the optimal filter required to maximize the contrast of a sub-10 nm bismuth flake on the micro-trench structures.

Ultra-thin bismuth flakes were also obtained with our exfoliation technique. Figure 4 shows three different flakes of average thickness 4 ± 2 nm, 7 ± 4 nm and 12 ± 4 nm. The average thickness is obtained by averaging the height of the flake and subtracting the average substrate height. The AFM scans are shown in Fig. 4(a), (b) and (c), and a profile is selected and plotted in Fig. 4(d), (e) and (f). Their optical microscopic images taken at $100\times$ magnification are shown in insets of Fig. 4(a), (b) and (c). Note that given the poor optical contrast of these ultra-thin flakes, the colors in these images are adjusted to enhance the visibility of these flakes by tuning the contrast, white balance and color levels.

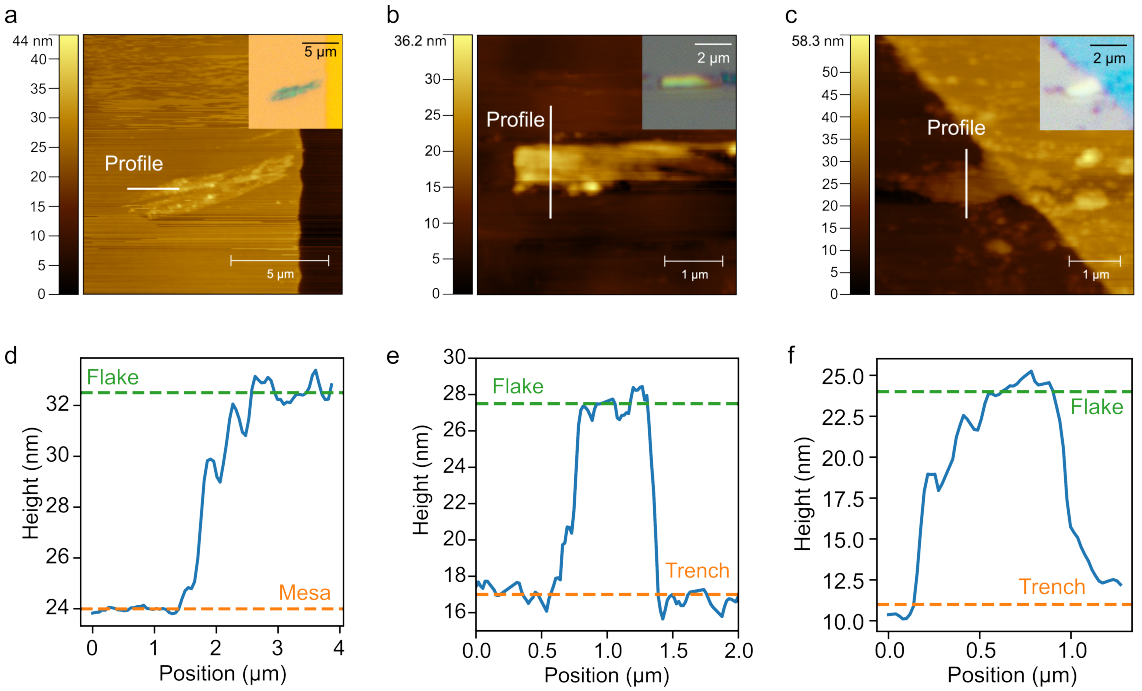

Figure 4: (a,b,c) AFM scans of ultra-thin bismuth flakes of average thickness 4 ± 2 nm, 7 ± 4 nm and 12 ± 4 nm. The optical images after contrast, balance and color level adjustments are shown in the insets. (d,e,f) AFM profile of exfoliated flakes along the line scans indicated in the respective AFM images.

As to other types of exfoliation techniques, our method can produce flakes with various sizes and thicknesses. We have analyzed AFM images of 469 flakes and recorded

their height and surface area. To better reveal the trend, these data were binned logarithmically by area and are shown on a logarithmic scale in Fig. 5. A clear linear trend is observed on this log-log scale, suggesting a power-law relationship $\propto$ area$^{0.38}$. As the data demonstrates, the flake thickness decreases as the surface area decreases, however, it is possible to obtain large area flakes with relatively small thicknesses in the sub-100 nm range. To fabricate a four terminal device for exploring electrical transport properties, a flake area of 1 µm^2 would be necessary. As it is seen in Fig. 4, for an area larger than 1 µm^2, we can obtain flakes as thin as 10 nm and often in the tens of nanometer range which is ideal to explore, among other predictions, the semi-metal to semi-conductor transition of bismuth [24].

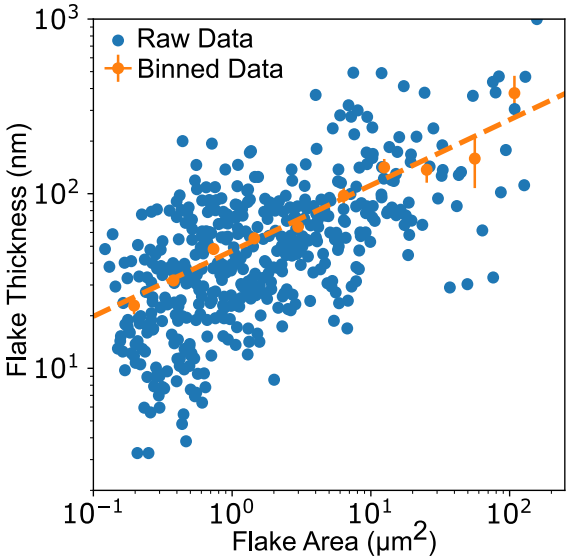

Figure 5: Flake height versus flake area in log-log scale. Binned (logarithmically) data with error bars given by the standard error. The fit reveals that thickness $\propto$ area$^{0.38}$.

3.2.5 Raman Characterization

Raman spectroscopy was performed in air on exfoliated flakes protected by a polymethylmethacrylate (PMMA) cap layer that was spun coated in a nitrogen glove box environment, as well as on the bulk crystal for benchmarking. The laser wavelength is 785 nm with 50$\times$ objective and 25 µm aperture diameter. Fig. 6(a) shows the Raman spectra of the bulk crystal's surface before and after it was freshly cleaved. Both bismuth Raman shift peaks at 70 cm^{-1} and 97 cm^{-1} for the E_g and A_{1g} vibrational modes, and as

well as the overtone at 187 cm^{-1}, are clearly observed [28,38], as expected for bismuth crystal. However, only the Raman spectrum on the surface of the bulk crystal clearly demonstrates the characteristic Raman shifts at 125 cm^{-1} and 313 cm^{-1} for the Bi-O bonds in β-phase bismuth oxide where the latter is commonly formed at lower temperatures under the 300°C range [39–41]. In contrast, after cleaving the bulk bismuth specimen and exposing its interior, the bismuth oxide peak disappeared, indicating that the oxidation is only present on the surface of the bulk crystal. Consequently, our mechanical exfoliation process is done in a glovebox, provoding a nitrogen-only environment with O_2 and water concentrations less than 1 ppm, hence avoiding oxidation of the exfoliated thin bismuth flakes.

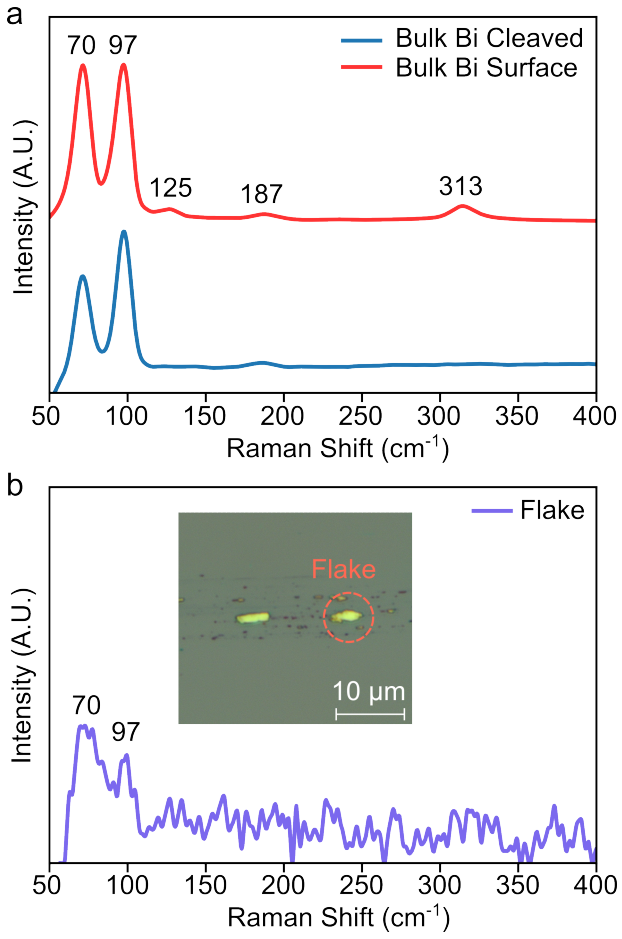

Figure 6: Raman spectroscopy of the bulk bismuth. The bismuth Raman peaks at 70 cm^{-1} and 97 cm^{-1}, and the β-phase of bismuth oxide's Raman peak at 313 cm^{-1} are shown.

To confirm this, a small flake of thickness 160 nm obtained from grating the bulk

crystal against micro-trench structures was also analyzed with Raman spectroscopy where the Raman shifts is shown in Fig. 6(b) along with the optical image of the flake in the inset. Given the small thickness and area of the flake, its signal is rather small. Nevertheless, the Raman peaks for bismuth at 70 cm^{-1} and 97 cm^{-1} are still observed unambiguously, confirming the presence of bismuth in the exfoliated flakes. The Raman peaks for β-phase bismuth oxide could not be observed within the detection limit of our Raman apparatus. This indicates that there is little or no sign of oxidation of the exfoliated flake. Indeed, given the small size of the flake, we expect the oxidation to be throughout the flake instead of only on its surface, hence the oxide peaks would dominate the Raman spectrum.

3.2.6 Conclusion

In this work, we described a novel exfoliation technique based on stress concentration effects induced by micro-trench structures. Previous mechanical cleavage methods use adhesion to a flat surface to exfoliate a layered crystal, or take advantage of the weak van der Waals force between atomic layers where bulk crystals are rubbed against a solid surface as in "drawing with chalk". In contrast, our approach uses the shear stress produced by scratching the bulk crystal against the hard SiO_2 substrate with micro-trench structures, acting as a "cheese grater". Such shearing motion produces stress concentration in the bulk crystal in contact with the trench edge, and consequently fractures are produced along the stress concentration line/point to strip thin layers.

We have shown that flakes as thin as $\sim$10 nm can be obtained with this exfoliation method, albeit they become barely visible under an optical microscope. In the *Supplemental Material*, we studied the contrast for ultra-thin bismuth flakes and showed that a red filter between the range of 500 - 570 nm greatly improves the flake visibility in the sub-10 nm range.

Most importantly, our work demonstrates the concept of using stress concentration to mechanically exfoliate crystals with strong bonds between interlayers. In the future,

this technique could prove useful to fabricate devices with 2D materials thought not possible to exfoliate via traditional mechanical exfoliation method.

3.2.7 References

[1] K.S. Novoselov, A.K. Geim, S.V. Morozov, D. Jiang, Y. Zhang, S. V. Dubonos, I.V. Grigorieva, and A.A. Firsov, "Electric Field Effect in Atomically Thin Carbon Films," Science **306**, 666 (2004).

[2] A. Castellanos-Gomez, L. Vicarelli, E. Prada, J.O. Island, K.L. Narasimha-Acharya, S.I. Blanter, D.J. Groenendijk, M. Buscema, G.A. Steele, J.V. Alvarez, H.W. Zandbergen, J.J. Palacios, and H.S.J. van der Zant, "Isolation and characterization of few-layer black phosphorus," 2D Mater. **1**, 025001 (2014).

[3] L. Li, Y. Yu, G.J. Ye, Q. Ge, X. Ou, H. Wu, D. Feng, X.H. Chen, and Y. Zhang, "Black phosphorus field-effect transistors," Nature Nanotech **9**, 372 (2014).

[4] H. Liu, A.T. Neal, Z. Zhu, Z. Luo, X. Xu, D. Tománek, and P.D. Ye, "Phosphorene: An Unexplored 2D Semiconductor with a High Hole Mobility," ACS Nano **8**, 4033 (2014).

[5] S.P. Koenig, R.A. Doganov, H. Schmidt, A.H. Castro Neto, and B. Özyilmaz, "Electric field effect in ultrathin black phosphorus," Appl. Phys. Lett. **104**, 103106 (2014).

[6] L. Kou, C. Chen, and S.C. Smith, "Phosphorene: Fabrication, Properties, and Applications," J. Phys. Chem. Lett. **6**, 2794 (2015).

[7] P. Curie, "Propriétés magnétiques des corps à diverses temperatures," *Ann. Chim. Phy.* **7**, 289 (1895).

[8] T. J. Seebeck, "Magnetische polarisation der metalle und erze durch temperaturdifferenz", p. 289 (Abh. Akad. Wiss. Berlin, Berlin, 1822-1823).

[9] A. v. Ettingshausen and W. Nernst, "Ueber das Auftreten electromotorischer Kräfte in Metallplatten, welche von einem Wärmestrome durchflossen werden und sich im magnetischen Felde befinden," Ann. Phys. Chem. **265**, 343 (1886).

[10] C.F. Gallo, B.S. Chandrasekhar, and P.H. Sutter, “Transport Properties of Bismuth Single Crystals,” J. Appl. Phys. **34**, 144 (1963).

[11] P. Hofmann, “The surfaces of bismuth: Structural and electronic properties," Prog. Surf. Sci. **81**, 191 (2006).

[12] Y. Liu, and R.E. Allen, “Electronic structure of the semimetals Bi and Sb," Phys. Rev. B **52**, 1566 (1995).

[13] X. Gonze, J.-P. Michenaud, and J.-P. Vigneron, “First-principles study of As, Sb, and Bi electronic properties," Phys. Rev. B **41**, 11827 (1990).

[14] L. Schubnikow, and W. J. de Haas, “A New Phenomenon in the Change of Resistance in a Magnetic Field of Single Crystals of Bismuth,” Nature **126**, 500 (1930).

[15] W. J. de Haas, and P. M. van Alphen, “The dependence of the susceptibility of diamagnetic metals upon the field,” Proc. Acad. Sci. Amst. **33**, 1106 (1930).

[16] F. Reis *et al.*, “Bismuthene on a SiC substrate: A candidate for a high-temperature quantum spin Hall material,” Science **357**, 287-290 (2017).

[17] F. Yang, A.O. Elnabawy, R. Schimmenti, P. Song, J. Wang, Z. Peng, S. Yao, R. Deng, S. Song, Y. Lin, M. Mavrikakis, and W. Xu, “Bismuthene for highly efficient carbon dioxide electroreduction reaction,” Nat. Commun. **11**, 1088 (2020).

[18] L. Aggarwal, P. Zhu, T.L. Hughes, and V. Madhavan, “Evidence for higher order topology in Bi and $Bi_{0.92}Sb_{0.08}$,” Nat. Commun. **12**, 4220 (2021).

[19] F. Schindler, Z. Wang, M.G. Vergniory, A.M. Cook, A. Murani, S. Sengupta, A.Yu. Kasumov, R. Deblock, S. Jeon, I. Drozdov, H. Bouchiat, S. Guéron, A. Yazdani, B.A. Bernevig, and T. Neupert, “Higher-order topology in bismuth,” Nat. Phys. **14**, 918 (2018).

[20] O. Prakash, A. Kumar, A. Thamizhavel, and S. Ramakrishnan, “Evidence for bulk superconductivity in pure bismuth single crystals at ambient pressure,” Science **355**, 52 (2017).

[21] M.-Y. Liu, Y. Huang, Q.-Y. Chen, Z.-Y. Li, C. Cao, and Y. He, "Strain and electric field tunable electronic structure of buckled bismuthene," RSC Adv. **7**, 39546 (2017).

[22] R. Gui, H. Jin, Y. Sun, X. Jiang, and Z. Sun, "Two-dimensional group-VA nanomaterials beyond black phosphorus: synthetic methods, properties, functional nanostructures and applications," J. Mater. Chem. A **7**, 25712 (2019).

[23] V. B. Sandomirskiĭ, "Quantum Size Effect in a Semimetal Film," Soviet Physics JETP **25**, 101 (1967).

[24] C.A. Hoffman, J.R. Meyer, F.J. Bartoli, A. Di Venere, X.J. Yi, C.L. Hou, H.C. Wang, J.B. Ketterson, and G.K. Wong, "Semimetal-to-semiconductor transition in bismuth thin films," Phys. Rev. B **48**, 11431 (1993).

[25] T. Hirahara, T. Shirai, T. Hajiri, M. Matsunami, K. Tanaka, S. Kimura, S. Hasegawa, and K. Kobayashi, "Role of Quantum and Surface-State Effects in the Bulk Fermi-Level Position of Ultrathin Bi Films," Phys. Rev. Lett. **115**, 106803 (2015).

[26] T.A. Halgren, "The representation of van der Waals (vdW) interactions in molecular mechanics force fields: potential form, combination rules, and vdW parameters," J. Am. Chem. Soc. **114**, 7827 (1992).

[27] N. A. Lange, *Lange's Handbook of Chemistry*, (McGraw-HIll, Toronto, 2005) p. 160.

[28] E.S. Walker, S.R. Na, D. Jung, S.D. March, J.-S. Kim, T. Trivedi, W. Li, L. Tao, M.L. Lee, K.M. Liechti, D. Akinwande, and S.R. Bank, "Large-Area Dry Transfer of Single-Crystalline Epitaxial Bismuth Thin Films," Nano Lett. **16**, 6931 (2016).

[29] T. Nagao, T. Doi, T. Sekiguchi, and S. Hasegawa, "Epitaxial Growth of Single-Crystal Ultrathin Films of Bismuth on Si(111)," Jpn. J. Appl. Phys. **39**, 4567 (2000).

[30] T. Nagao, J. Sadowski, M. Saito, S. Yaginuma, Y. Fujikawa, T. Kogure, T. Ohno, Y. Hasegawa, S. Hasegawa, and T. Sakurai, “Nanofilm Allotrope and Phase Transformation of Ultrathin Bi Film on Si(111)-7×7,” Phys. Rev. Lett. **93**, 105501 (2004).

[31] T. Nagao, S. Yaginuma, M. Saito, T. Kogure, J.T. Sadowski, T. Ohno, S. Hasegawa, and T. Sakurai, “Strong lateral growth and crystallization via two-dimensional allotropic transformation of semi-metal Bi film,” Surf. Sci. **590**, 247 (2005).

[32] T. Hirahara, G. Bihlmayer, Y. Sakamoto, M. Yamada, H. Miyazaki, S. Kimura, S. Blügel, and S. Hasegawa, “Interfacing 2D and 3D Topological Insulators: Bi(111) Bilayer on Bi_2Te_3,” Phys. Rev. Lett. **107**, 166801 (2011).

[33] F. Yang, L. Miao, Z.F. Wang, M.-Y. Yao, F. Zhu, Y.R. Song, M.-X. Wang, J.-P. Xu, A.V. Fedorov, Z. Sun, G.B. Zhang, C. Liu, F. Liu, D. Qian, C.L. Gao, and J.-F. Jia, “Spatial and Energy Distribution of Topological Edge States in Single Bi(111) Bilayer,” Phys. Rev. Lett. **109**, (2012).

[34] M. Ozhukil Valappil, A. Ganguly, J. Benson, V.K. Pillai, S. Alwarappan, and P. Papakonstantinou, “Bismuthene nanosheets produced by ionic liquid assisted grinding exfoliation and their use for oxygen reduction reaction," RSC Adv. **10**, 43585 (2020).

[35] B. Yang, X. Li, Y. Cheng, S. Duan, B. Zhao, W. Yi, C. Wang, H. Sun, Z. Wang, D. Gu, S. Chen, and X. Liu, “Liquid phase exfoliation of bismuth nanosheets for flexible all-solid-state supercapacitors with high energy density," J. Mater. Chem. C **8**, 12314 (2020).

[36] Y. Zhang, J.P. Small, W.V. Pontius, and P. Kim, “Fabrication and electric-field-dependent transport measurements of mesoscopic graphite devices," Appl. Phys. Lett. **86**, 073104 (2005).

[37] G.V. Samsonov, *Handbook of the Physicochemical Properties of the Elements: Mechanical Properties of the Elements*, (Springer, Boston, 1968), p. 387.

[38] C. Rodríguez-Fernández, K. Akius, M. Morais de Lima, A. Cantarero, J.M. van Ruitenbeek, and C. Sabater, “Raman signal reveals the rhombohedral crystallographic structure in ultra-thin layers of bismuth thermally evaporated on amorphous substrate," Mater. Sci. Eng. B **270**, 115240 (2021).

[39] F.D. Hardcastle, and I.E. Wachs, “The molecular structure of bismuth oxide by Raman spectroscopy," Journal of Solid State Chem. **97**, 319 (1992).

[40] A. J. Salazar-Pérez, A. J., M. A. Camacho-López, R. A. Morales-Luckie, V. Sánchez-Mendieta, F. Ureña-Núñez, and J. Arenas-Alatorre, “Structural evolution of Bi_2O_3 prepared by thermal oxidation of bismuth nano-particles,” *Superficies y Vacio* **18**, 4 (2005).

[41] J .A. Steele, and R. A. Lewis, “In situ micro-Raman studies of laser-induced bismuth oxidation reveals metastability of β-Bi_2O_3 microislands," Opt. Mater. Express **4**, 2133 (2014).

3.2.8 List of Figures

4

Anomalous Hall Effect in Thin Bismuth

4.1 Introduction

The development of this novel technique for exfoliating thin flakes of bismuth enables the study of their transport properties, which is the central focus of my PhD thesis. While most research on bismuth has concentrated on its bulk form, the properties of thin films or flakes remain largely unexplored, despite recent progress.

Even though the micro-trench exfoliation method successfully produced thin bismuth flakes, fabricating them into transport devices proved to be non-trivial. As discussed in Chapter 3, the flake size scales with thickness, meaning that thinner flakes inevitably have smaller surface areas, which complicates device fabrication — even with

high-precision patterning techniques like electron-beam lithography (EBL). Additionally, since the exfoliation tends to occur along the edges of the trench, the resulting thin flakes often have an elongated shape, making them unsuitable for fabricating devices with Hall bar or van der Pauw (vdP) geometries. Consequently, many of the fabricated thin bismuth devices are in a "comb" geometry, as shown in the Supplemental Information of the manuscript in the present chapter (Appendix B). While these "comb" devices are generally suitable for analyzing the longitudinal resistance, they are not ideal for Hall measurements.

More challenges arise when it comes to the actual measurements. In particular, many of the fabricated devices have a high two-point resistances on the order of megaohms to gigaohms, especially in thinner flakes under 100 nm. Furthermore, these devices usually demonstrate IV curves resembling a Schottky barrier formed at a metal-semiconductor junction. Recall that bismuth was predicted to have semimetal-to-semiconductor (SMSC) transition at around 30 nm which could explain such behavior, especially considering the use of gold contacts.

Devices displaying a Schottky barrier also frequently show unstable IV characteristics, which can be partially improved through current annealing. However, annealing usually fails to stabilize the device sufficiently for reliable analysis. Interestingly, no clear relationship exists between the thickness of the flakes and the two-point resistance, with resistance levels sometimes being similar across all devices from the same batch. This raises the possibility that the issue lies in contact resistance, possibly due to the limited overlap between the contacts and each flake. Plasma etching has been tested on some batches to remove potential PMMA residue, but this method has not yielded any noticeable improvement.

Another common issue is backgate leakage. The bismuth flakes are exfoliated onto a substrate consisting of 300 nm SiO_2 on top of doped Si, allowing the substrate to function as a backgate. However, the micro-trench patterns on the substrate require reactive ion etching (RIE), which likely degrades the quality of the SiO_2 layer. Additionally, mechanical pressure is applied to press the bulk bismuth crystal against the micro-trench

during exfoliation. This stress can further degrade the oxide layer, making gate leakage more likely.

Despite these challenges, a small subset of fabricated devices showed no gate leakage and became ohmic after intense current annealing. In three of these ohmic devices, a distinctive pattern emerged in the R_{xy} data when plotted against the magnetic field, resembling a magnetization curve. After two years of investigation, we concluded that we had discovered the anomalous Hall effect in thin bismuth. This finding is the focus of the manuscript entitled "Anomalous Hall Effect in Thin Bismuth". The full manuscript presented below is identical to the published version in *Physical Review B* [53]. The figure labels and reference numberings are also aligned with those of the published manuscript and are independent from the rest of the thesis. The Supplemental Information of this manuscript is presented in Appendix B.

4.2 Manuscript

4.2.1 Abstract

Bismuth, the heaviest of all group V elements with strong spin-orbit coupling, is famously known to exhibit many interesting transport properties, and effects such as Shubnikov-de Haas and de Haas-van Alphen were first revealed in its bulk form. However, the transport properties have not yet been fully explored experimentally in thin bismuth nor in its 2D limit. In this work, bismuth flakes with average thicknesses ranging from 29 to 69 nm were mechanically exfoliated by a micro-trench technique and were used to fabricate four-point devices. Due to mixing of components, Onsager's relations were used to extract the longitudinal (R_{xx}) and Hall (R_{xy}) resistances where the latter shows a Hall anomaly that is consistent with the Anomalous Hall Effect (AHE). Our work strongly suggests that that there could be a hidden mechanism for time-reversal symmetry breaking in pure bismuth thin films.

4.2.2 Introduction

The Anomalous Hall Effect (AHE) was discovered by Edwin Hall only a year after his discovery of the ordinary Hall Effect. However, unlike the classical Hall effect that was immediately rationalized, the mechanism for AHE remained the subject of debate for nearly a century. Today, it is believed that AHE has two types of contributions [1,2]: an *intrinsic*, scattering-free, mechanism originally proposed by Karplus and Luttinger [3] that can also be reconciled with the presence of a Berry curvature (see Fig. 1a), as well as scattering-dependent mechanisms known as *extrinsic* contributions (see Fig. 1b). Despite these advances in the 1950s, AHE remains poorly understood in certain systems such as, for example, spin glasses. Notably with the recent emergence of topologically non-trivial band structures, the study and understanding of AHE in these materials led to a renaissance of interest in the topic.

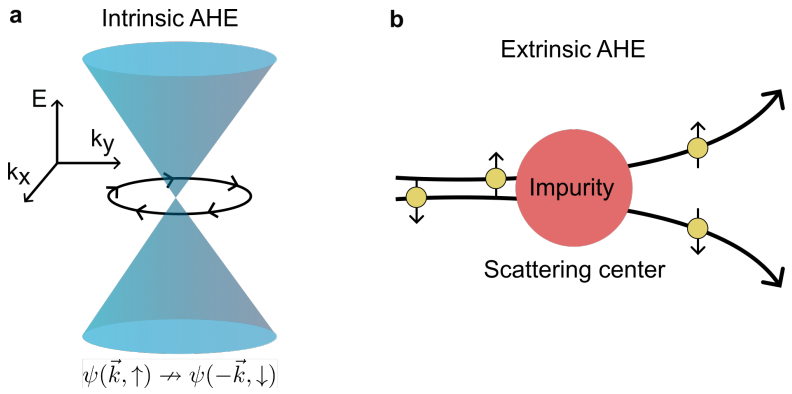

Figure 1: (a) Intrinsic AHE arises from time reversal symmetry (TRS) breaking intrinsic to electronic structure. (b) Extrinsic AHE arises from impurity scattering mechanisms that break TRS.

Bismuth is the heaviest group V element ($Z = 83$) and has therefore a very large atomic spin-orbit coupling (SOC) [4,5]. However, due to inversion symmetry in the bulk Bi crystal, the bulk itinerant carriers do not experience SOC, in contrast to the surface state carriers. Bismuth in the bulk form has been extensively studied and has a long history of exhibiting celebrated transport properties. Remarkably, effects such as the Shubnikov-de Haas (SdH) effect, the de Haas-van Alphen effect and the Nernst–Ettingshausen effect were first discovered in bismuth. Recently, in part due to the discovery of graphene,

interest in bismuth has been revived for its predicted properties in thin layered structures and in its 2D form known as bismuthene. For instance, a semimetal to semiconductor transition is predicted to occur when its thickness reaches 30 nm or less [6–8], but finding such transition has been proven to be experimentally difficult due to fabrication challenges and the potentially non-trivial contribution of surface states [4]. Yet, quantum confinement is important in understanding transport properties of films of thickness up to about 100 nm [9–11]. Furthermore, advances were made in isolating the single layer allotrope, bismuthene, and it was successfully grown for the first time on a SiC substrate in 2017 [12], albeit its transport properties still await to be unraveled experimentally. More recently, there has been a widespread interest in bismuth as there is substantial evidence for it to be a higher order topological insulator (HOTI) [13, 14] and to host intrinsic superconductivity where the transition occurs below $T_c \approx 0.5$ mK [10]. As such, this makes bismuth an excellent candidate to study AHE in a system that is topologically non-trivial.

If time-reversal symmetry (TRS) is broken in bismuth, then one would expect it to manifest the intrinsic AHE [1, 2]. For instance, the work of Y. Hirai *et al.* on 30 nm bismuth film experimentally demonstrated that circularly polarized light can open a gap in the bismuth's band structure, leading to time-reversal symmetry breaking which then leads to an AHE [16]. Moreover, in a model proposed by Haldane in 1988, he argues that TRS breaking on a honeycomb lattice can lead to a Quantum Anomalous Hall Effect (QAHE) [17]. QAHE was first observed by Chang *et al.* [18] in 2013, and in 2018 A. Young *et al.* [19] experimentally found QAHE in twisted bilayer graphene where TRS was broken when the interlayer twist angle in the moiré pattern is $\theta \approx 1.1°$. Here, we report on our work in sub-100 nm bismuth films whereby an unambiguous signature of the AHE was observed in electronic transport measurements. Bismuth is known to be a diamagnetic material and as such the manifestation of AHE requires the breaking of TRS which is to our knowledge unexpected. Our observation of the AHE in pure bismuth suggests that a hidden mechanism must be responsible for the TRS breaking. This discovery is not only important to further understand the already

extensively studied properties of bismuth, but also to extend our comprehension of the AHE.

4.2.3 Method

We developed a novel technique using micro-trench structure to mechanically exfoliate thin bismuth flakes [20]. The micro-trench structure was prepared by etching a SiO_2 thermal oxide layer above a degenerately doped silicon substrate, effectively turning it to a mechanical file. As shown in Fig. 2a, bulk bismuth crystal, with its orientation carefully chosen to be the (1,1,1) surface, was attached to the tip of a metal pen. By grating the bismuth crystal against the micro-trench file, thin flakes of bismuth were obtained and found to be as thin as $\sim$10 nanometers [20]. Such mechanical exfoliation provides a way to obtain ultra-thin bismuth flakes in a clean and controlled environment. In particular, compared to the recently reported exfoliation methods using liquid sonication [21, 22], water and oxygen that are detrimental to electronic properties can be avoided. While molecular beam epitaxy (MBE) techniques can produce films down to 3 nm [23], our method is far more straightforward to prepare high quality flakes down to comparable thicknesses.

Thin bismuth flakes with average thicknesses of 29 to 69 nm were obtained and characterized by atomic force microscopy (AFM), see *Supplemental Information*. Note that the flakes have height variations, and only the average height is quoted here. Ti/Au contacts were deposited *via* electron beam lithography (EBL) and electron beam vapor deposition. Note that the environment was carefully controlled with all fabrication steps performed in a vacuum, or in a nitrogen-filled glovebox. Lastly, a polymethyl methacrylate (PMMA) capping layer was spincoated for protecting the bismuth flake against oxidization. An optical image of a 68 nm device (see *Supplemental Information*) fabricated in the van der Pauw (vdP) geometry is shown in Fig. 2c, with the schematic shown in Fig. 2b. Two other devices fabricated in a comb geometry are shown in the *Supplemental Information*. Note that due to the small size of the flake ($\sim 1 \times 1$ μm), as we will discuss below, the ohmic contacts are subject to misalignments and hence

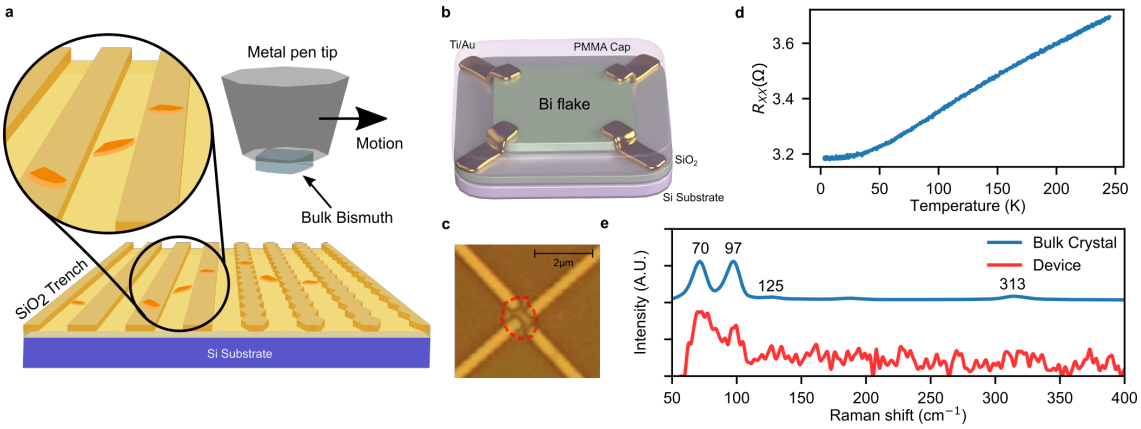

Figure 2: (a) Mechanical exfoliation of bismuth by grating bulk bismuth crystal against SiO_2 micro-trench structures. (b) Schematic of the device and (c) optical microscope image of the fabricated device in van der Pauw configuration where the red dashed lines indicate the perimeter of the flake as confirmed by AFM (see *Supplemental Information*). (d) Four-point resistance as a function of temperature. (e) Raman spectroscopy of the device compared to its bulk counterpart. Note that 70 and 97 cm^{-1} are Stokes shifts for pure bismuth whereas bismuth oxide β-Bi_2O_3 has a Raman peak at 313 cm^{-1} which was not observed for the device. Raman spectra were normalized to the bismuth peak of 70 cm^{-1}.

mixing of electronic transport components is to be expected.

The chemical nature of bismuth flakes was confirmed *via* Raman spectroscopy with a Bruker Senterra confocal Raman equipped with a 785 nm laser. The flake was compared to its bulk counterpart of the same crystal as a benchmark. The small Raman signal of the flake is due to its small size, however it was still possible to observe the 70 cm^{-1} and 97 cm^{-1} Raman shift peaks associated with pure bismuth [24,25], see Fig. 2e (red). Additionally, the most common type of bismuth oxide typically formed at lower temperatures ($\lesssim$300°C), β-Bi_2O_3, was observed in the bulk crystal (blue) at 125 cm^{-1} and 313 cm^{-1} [26–28] but not in the exfoliated flake.

The temperature dependence of the resistance of the van der Pauw device is plotted in Fig. 2d from 3 to 250 K, and is consistent with previously reported values for bulk semi-metallic bismuth [29,30] as well as thin films down to 500 nm [58].

4.2.4 Results and Discussions

The small size and the limitation imposed by EBL resulted in the van der Pauw contacts to be deposited relatively close to each other, as can be seen in Fig. 2c. Since the contacts are not exactly at the corners as depicted in Fig. 2b, the longitudinal (XX) and Hall (XY) resistances are expected to be mixed to some degree in every probe configuration. To overcome this mixing, we use the Onsager symmetrization to reconstruct the true longitudinal R_{xx} and Hall R_{xy} resistances. According to the Onsager's reciprocity theorem [41], inverting the current and voltage contacts in a linear system allows us to measure the transpose of the resistance tensor given by

$$R(B) = \begin{pmatrix} R_{xx} & R_{xy} \\ -R_{xy} & R_{xx} \end{pmatrix},$$

where B is the applied magnetic field. Consequently, by measuring the resistance in one configuration as well as its Onsager reciprocal, the true longitudinal R_{xx} and Hall R_{xy} resistances can be obtained by respectively symmetrizing and anti-symmetrizing the two configurations with

$$R_{xx} = \frac{R + R'}{2},$$
$$\text{and} \qquad R_{xy} = \frac{R - R'}{2},$$

where R and R' form an Onsager pair. For example, a four-point measurement configuration labeled ABCD (corresponding to probes I+/V+/V-/I-) would have its Onsager reciprocal with contact configuration BADC.

The resistances versus magnetic fields (with positive field defined as pointed into the page, see Fig. 3 insets) were measured at 15 mK and are shown in Fig. 3. We stress that mixing of the R_{xx} and R_{xy} was inevitably observed, however Fig. 3a and Fig. 3b are XY configurations that maximize the Hall signal and that are also Onsager reciprocals to one another. Similarly, Fig. 3c and Fig. 3d are the XX configurations that optimize

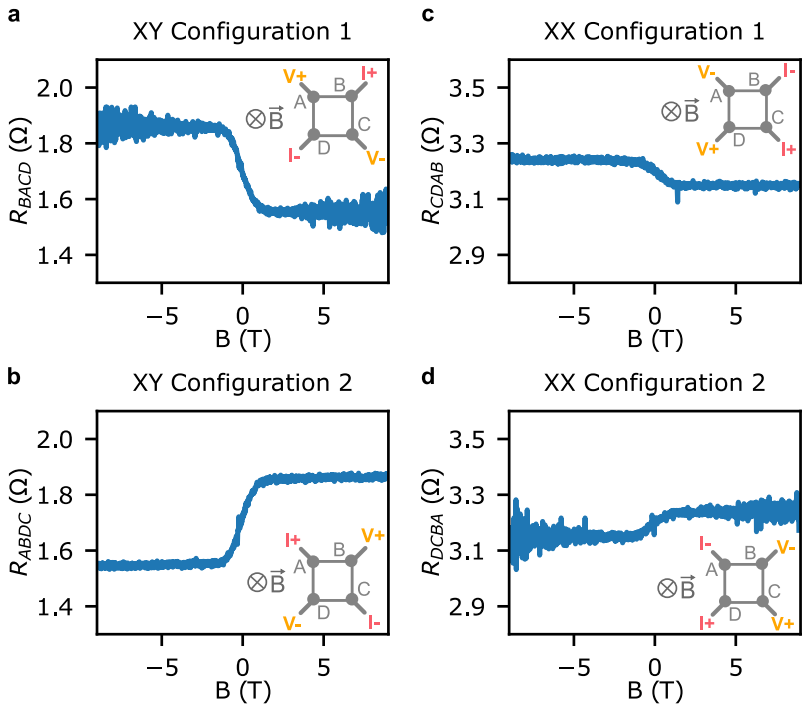

Figure 3: Four-point resistances of different probing configurations versus magnetic field B (positive defined as pointed into the page) at 15 mK. (a) and (b) are in the XY configurations and form an Onsager pair, and (c) and (d) are in the XX configurations and are Onsager reciprocals. The contacts configurations are shown in the insets.

the XX signal while also capturing a mixed Hall signal. The corresponding ideal probe configurations in the van der Pauw geometry are shown in the insets of Fig. 3.

Figure 4 summarizes our main result: the extracted true Hall and longitudinal resistances as a function of the magnetic field B. Figure 4a shows the anti-symmetrized signal from the XY configurations, and as expected it is greater than the anti-symmetrized signal from the XX configurations. Similarly, the true longitudinal signal symmetrized in a similar fashion is shown in Fig. 4b and Fig. 4c for the XX and XY configuration pairs, respectively. In particular, both true R_{xx} are constant as a function the magnetic field up to ± 9 T. The resistance values are 3.2 Ω (extracted from XX) and 1.7 Ω (extracted from XY). The difference in the extracted resistances is attributed to the contacts that are not equidistant from one another, as the ratio of the R_{xx} resistances is approximately equal to the ratio of the distances between the voltage probes.

From the Hall response shown in Fig. 4a, careful inspection of the data shows the

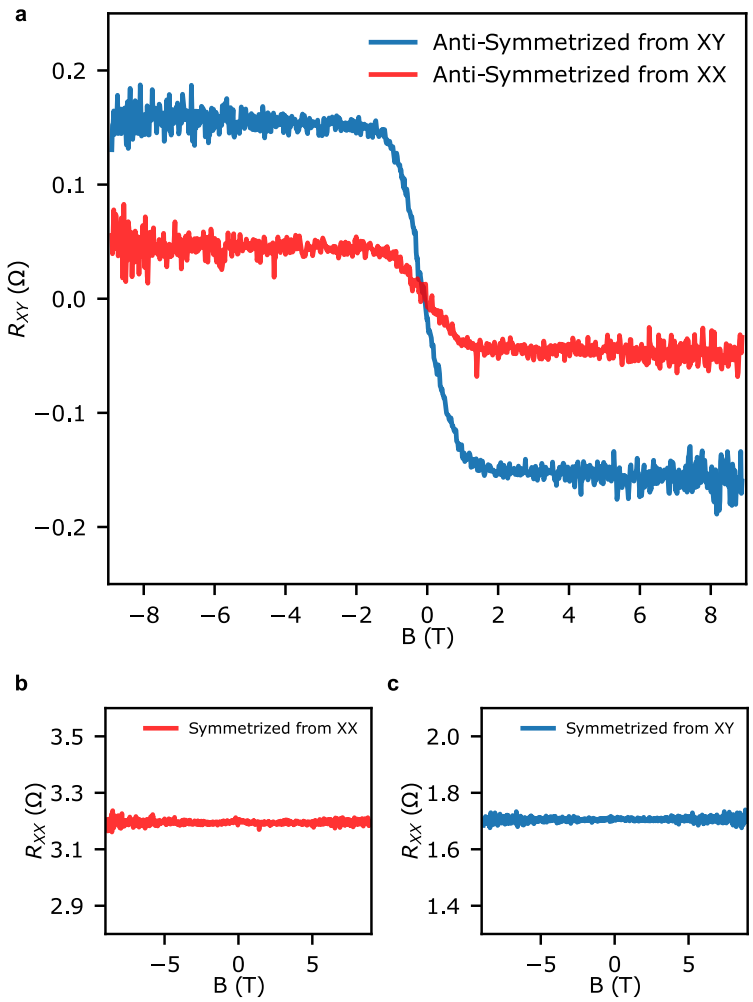

Figure 4: (a) R_{xy} extracted from XX and XY Onsager pairs through anti-symmetrization, showing the Hall anomaly. (b) and (c) are the extracted R_{xx} from the same Onsager pairs.

presence of a very small slope in the saturated regime of the Hall signal. In particular, for the XY configuration's saturated high-field region ($|B| \geq 2$ T), a fit to the linear slope yields the value $-0.0010(4)$ Ω/T, and similarly a linear fit to the XY configuration's low field region ($|B| \leq 0.5$ T) yields a slope of $-0.174(3)$ Ω/T, see *Supplemental Information* for the detailed extraction of these values. While the negative values found for both linear Hall signals support the electronic transport being hole-dominated, it is unfortunately not possible to reliably extract carrier densities and mobilities because the constancy of the R_{xx} shown in Fig. 4(a) and (b) is uncharacteristic of the multi-carrier model. Bismuth is known to host both electron and hole pockets in the bulk [33,34], as

well as in thin films [35–37]. If both carriers were present, R_{xx} can only saturate at high fields if the densities of electrons and holes were unequal, *i.e.* $n \neq p$. The characteristic field for this saturation is given by [38]

$$B^{\star} = \frac{n\mu_p + p\mu_n}{|n-p|\mu_n\mu_p},$$

where n and p are electron and hole densities, and μ_n and μ_p are electron and hole mobilities. Note that the reduced Hall slope observed at high fields in Fig. 4(a) implies that $|n-p| \ll 1$ which leads to a very high saturation field for R_{xx}. Under such saturation, R_{xx} would have a magnetic field dependence $\propto B^2$, and if R_{xy} is dominated by a low density, high mobility carrier at low fields, it would have a magnetic field dependence $\propto B^3$. Neither of these are observed in our work. Carrier density in bismuth can also have a field dependent effect [38–40], but the linearity of R_{xy} with B at high field implies that density variation is not responsible for the observations made here. Moreover, the elongated Fermi surface pockets known for bulk bismuth [4] can strongly affect the transport behavior. That being said, the multi-carrier model discussed above is valid as long as the Fermi surfaces are closed. Meanwhile, the possibility of an open orbit in the Fermi surface can be excluded because it is inconsistent with the saturation of R_{xx} at high field as observed in our experiments. All things considered, we cannot reconcile the multi-carrier model with the Hall and magnetotransport data presented in this work. Furthermore, in contrast to bulk bismuth where quantum oscillations can be observed well under 1 T [41], in our case we did not observe any SdH oscillations in the longitudinal resistance. As we will discuss below, this unexpected behaviour was nevertheless observed previously in a 100 nm thick film grown by MBE [58].

Using the device geometry and the longitudinal resistance measured in the absence of a magnetic field, the conductivity is calculated to be $\sigma_{xx} \sim 10^5\ (\Omega\,\mathrm{cm})^{-1}$ which places the bismuth device in a good-metal regime dominated by scattering-independent mechanisms [1]. It is indeed expected for bismuth to manifest the intrinsic AHE [1, 2] because of its high SOC. However, TRS breaking is a necessary condition for both intrinsic and extrinsic AHE, and as such, SOC alone is not sufficient to explain the

AHE signal observed here. Usually, intrinsic TRS breaking is achieved by ferro- or antiferromagnetism, but bulk bismuth is known to be the most diamagnetic element with a magnetic susceptibility value of -1.66×10^{-4} [42]. Consequently, unless a magnetic transition would occur as the thickness of bismuth is reduced, TRS breaking must originate from elsewhere. Interestingly, in their growth and characterization of bismuth thin films by MBE, Partin *et al.* found a Hall resistivity and magnetoresistivity nearly identical to our data for their thinnest 100 nm bismuth film (see Fig. 6 of [58]). Specifically, their magnetoresistivity in the 100 nm film was found to be independent of the magnetic field and the Hall resistivity shows a similar AHE behaviour with a saturation near 1 T, as is observed in our work. Importantly, the work of Partin *et al.* found more conventional behavior for films thicker than 100 nm, leading to the observation of SdH oscillations which is absent in the 100 nm film even for magnetic fields as high as 17 T. The complete featureless and flat trend observed in their and our works for bismuth of similar thicknesses remains an intriguing mystery.

More recently, B. C. Camargo *et al.* claimed to have observed the AHE in bulk bismuth but were unable to find the source of the TRS breaking either [43]. A portion of their work was dedicated to eliminate magnetic contamination and superconductivity, and it was concluded that the AHE may arise from the topologically non-trivial surface or hinge states rather than in the bulk. Such arguments align with our observation of the AHE in thin devices with average flake thicknesses of 68 nm (main text), 29 nm and 69 nm (see *Supplemental Information*). Strikingly, these two other devices were fabricated in a comb geometry, yet the four-probe resistances demonstrated a magnetic field response similar to that of AHE measured in the vdP device presented in the main section of our article. While the longitudinal resistances of the vdP and comb devices were different (2 to 32 Ω), the anomalous Hall responses were unexpectedly similar (0.1 to 0.4 Ω), hinting that the observed AHE does not arise from the bulk, but instead from the surface. The resistance's temperature dependence which is consistent with that of the bulk bismuth down to 500 nm also supports this observation as it suggests that the bulk is measured simultaneously with the surface or hinge states.

Finally, in addition to a non-trivial topology in bismuth [12–14, 44], there are also other prospect origins for spontaneous TRS breaking. These include band-flattening as in the case of twisted bilayer graphene, orbital magnetism of Dirac electrons that could arise in bismuth, and strain-induced band distortion [45–47] that could all lead to a broken TRS. There is a long sequence of works supporting an intrinsic AHE in bismuth. From Conn and Donovan's work in the late 1940s which found traces of AHE [43, 48, 49], to the recent work by B. C. Camargo for the bulk [43], as well as our own work in exfoliated bismuth that is consistent with Partin's MBE-grown 100 nm bismuth thin film, all these works point towards a *bona fide* intrinsic AHE occurring in bismuth with an unknown origin of broken TRS.

4.2.5 Conclusion

We successfully fabricated sub-100 nm bismuth devices and studied their electronic transport properties. Its measured Hall resistance is consistent with the Anomalous Hall effect despite bismuth being highly diamagnetic. Our results strongly suggest that there must exist a mechanism for breaking TRS in bismuth which needs to be further investigated and understood. In future works, we expect to explore the Hall anomaly at higher magnetic fields and at different field effect gate voltages to obtain a better understanding of its electronic band structure as well as a more profound comprehension of its predicted non-trivial topology. As such, and in spite of having been one of the most extensively studied materials since the 19$^{\text{th}}$ century, bismuth remains a fascinating elemental material that is yet to be fully understood.

4.2.6 References

[1] N. Nagaosa, J. Sinova, S. Onoda, A. H. MacDonald, and N. P. Ong, Anomalous Hall effect, Rev. Mod. Phys. **82**, 1539 (2010).

[2] D. Culcer, The Anomalous Hall Effect, arXiv:2204.02434, (2020).

[3] R, Karplus and J. M. Luttinger, Hall Effect in Ferromagnetics, Phys. Rev. **95**, 1154 (1954).

[4] Ph. Hofmann, The surfaces of bismuth: Structural and electronic properties, Prog. Surf. Sci. **81**, 191-245 (2006).

[5] X Gonze, J-P Michenaud, and J-P Vigneron, Ab initio calculations of bismuth properties, including spin–orbit coupling, Phys. Scr. **37**, 785 (1988).

[6] V. B. Sandomirskiĭ, Quantum Size Effect in a Semimetal Film, Soviet Physics JETP **25**, 101 (1967).

[7] C.A. Hoffman, J.R. Meyer, F.J. Bartoli, A. Di Venere, X.J. Yi, C.L. Hou, H.C. Wang, J.B. Ketterson, and G.K. Wong, Semimetal-to-semiconductor transition in bismuth thin films, Phys. Rev. B **48**, 11431 (1993).

[8] T. Hirahara, T. Shirai, T. Hajiri, M. Matsunami, K. Tanaka, S. Kimura, S. Hasegawa, and K. Kobayashi, Role of Quantum and Surface-State Effects in the Bulk Fermi-Level Position of Ultrathin Bi Films, Phys. Rev. Lett. **115**, (2015).

[9] Shunhao Xiao, Dahai Wei, and Xiaofeng Jin, Bi(111) Thin Film with Insulating Interior but Metallic Surfaces, Phys. Rev. Lett. **109**, 166805 (2012).

[10] N. Marcano, S. Sangiao, C. Magén, L. Morellón, M. R. Ibarra, M. Plaza, L. Pérez, and J. M. De Teresa, Role of the surface states in the magnetotransport properties of ultrathin bismuth films, Phys. Rev. B **82**, 125326 (2010).

[11] Zijian Jiang, V. Soghomonian, and J. J. Heremans, Carrier properties of Bi(111) grown on mica and Si(111), Phys. Rev. Materials **6**, 095003 (2022).

[12] F. Reis, G. Li, L. Dudy, M. Bauernfeind, S. Glass, W. Hanke, R. Thomale, J. Schäfer, and R. Claessen, Bismuthene on a SiC substrate: A candidate for a high-temperature quantum spin Hall material, Science **357**, 287-290 (2017).

[13] L. Aggarwal, P. Zhu, T. L. Hughes, and V. Madhavan, Evidence for higher order topology in Bi and $Bi_{0.92}Sb_{0.08}$, Nat. Comm. **12**, (2021).

[14] F. Schindler, Z. Wang, M. G. Vergniory, A. M. Cook, A. Murani, S. Sengupta, A. Yu. Kasumov, R. Deblock, S. Jeon, I. Drozdov, H. Bouchiat, S. Guéron, A. Yazdani, B. A. Bernevig, and T. Neupert, Higher-order topology in bismuth, Nat. Phys. **14**, 918–924 (2018).

[15] O. Prakash, A. Kumar, A. Thamizhavel, and S. Ramakrishnan, Evidence for bulk superconductivity in pure bismuth single crystals at ambient pressure, Science **335**, 52-55 (2017).

[16] Y. Hirai, N. Yoshikawa, M. Kawaguchi, M. Hayashi, S. Okumura, T. Oka, and R. Shimano, Anomalous Hall effect of light-driven three-dimensional Dirac electrons in bismuth, arXiv:2301.06072, (2023).

[17] F. D. M. Haldane, Model for a Quantum Hall Effect without Landau Levels: Condensed-Matter Realization of the "Parity Anomaly", Phys. Rev. Lett. **61**, 2015 (1988).

[18] C.-Z. Chang, J. Zhang, X. Feng, J. Shen, Z. Zhang, M. Guo, K. Li, Y. Ou, P. Wei, L.-L. Wang, Z.-Q. Ji, Y. Feng, S. Ji, X. Chen, J. Jia, X. Dai, Z. Fang, S.-C. Zhang, K. He, Y. Wang, L. Lu, X.-C. Ma, and Q.-K. Xue, Experimental Observation of the Quantum Anomalous Hall Effect in a Magnetic Topological Insulator, Science **340**, 167–170 (2013).

[19] M. Serlin, C. L. Tschirhart, H. Polshyn, Y. Zhang, J. Zhu, K. Watanabe, T. Taniguchi, K. Balents, and A. F. Young, Intrinsic quantized anomalous Hall effect in a moiré heterostructure, Science **367**, 900-903 (2019).

[20] Oulin Yu, R. Allgayer, S. Godin, J. Lalande, P. Fossati, Chunwei Hsu, T. Szkopek, and G. Gervais, Method of Mechanical Exfoliation of Bismuth with Micro-Trench Structures, J. Appl. Phys. **134**, 244302 (2023).

[21] M. Ozhukil Valappil, A. Ganguly, J. Benson, V.K. Pillai, S. Alwarappan, and P. Papakonstantinou, Bismuthene nanosheets produced by ionic liquid assisted grinding exfoliation and their use for oxygen reduction reaction, RSC Adv. **10**, 43585 (2020).

[22] B. Yang, X. Li, Y. Cheng, S. Duan, B. Zhao, W. Yi, C. Wang, H. Sun, Z. Wang, D. Gu, S. Chen, and X. Liu, Liquid phase exfoliation of bismuth nanosheets for flexible all-solid-state supercapacitors with high energy density, J. Mater. Chem. C **8**, 12314 (2020).

[23] E.I. Rogacheva, S.N. Grigorov, O.N. Nashchekina, S. Lyubchenko, and M.S. Dresselhaus, Quantum-size effects in n-type bismuth thin films, Appl. Phys. Lett. **82**, 2628–2630 (2003).

[24] C. Rodriguez-Fernandez, K. Akius, M. Morais de Lima, Andres Cantarero, J. M. van Ruitenbeek, and C. Sabater, Raman signal reveals the rhombohedral crystallographic structure in ultra-thin layers of bismuth thermally evaporated on amorphous substrate, Materials Science & Engineering B **270**, 115240 (2021).

[25] E. S. Walker, S. R. Na, D. Jung, S. D. March, J.-S. Kim, T. Trivedi, W. Li, L. Tao, M. L. Lee, K. M. Liechti, D. Akinwande, S. R. Bank, Large-Area Dry Transfer of Single-Crystalline Epitaxial Bismuth Thin Films, Nano Lett **16**, 6931–6938 (2016).

[26] F. D. Hardcastle and I. E. Wachs, The molecular structure of bismuth oxide by Raman spectroscopy, J. Solid State Chem. **97**, 319-331 (1992).

[27] A. J. Salazar-Pérez, M. A. Camacho-Lopez, R. A. Morales-Luckie, V. Sanchez-Mendieta, F. Urena-Nunez, and J. Arenas-Alatorre, Structural evolution of Bi_2O_3 prepared by thermal oxidation of bismuth nano-particles, Superficies y Vacio **18**, (2005).

[28] J. A. Steele and R. A. Lewis, *In situ* micro-Raman studies of laser-induced bismuth oxidation reveals metastability of β-Bi_2O_3 microislands, Opt. Mater. Express **4**, 2133-2142 (2014).

[29] C. A. Kukkonen and K. F. Sohn, The Low-Temperature Electrical Resistivity of Bismuth, J. Phys. F: Met. Phys. **7**, L193 (1977).

[30] R. A. Hoffman and D. R. Frankl, Electrical Transport Properties of Thin Bismuth Films, Phys. Rev. B **3**, 1825 (1971).

[31] D. L. Partin, J. Heremans, D. T. Morelli, C. M. Thrush, C. H. Olk, and T. A. Perry, Growth and Characterization of Epitaxial Bismuth Films, Phys. Rev. B **38**, 3818 (1988).

[32] H. H. Sample, W. J. Bruno, S. B. Sample, and E. K. Sichel, Reverse-field reciprocity for conducting specimens in magnetic fields, J. of Appl. Phys. **61**, 1079-1084 (1987).

[33] A. L. Jain and S. H. Koenig, Electrons and Holes in Bismuth, Phys. Rev. **127**, (1962).

[34] A. L. Jain, S. K. Suri, and K. Tanaka, Charge carrier densities and mobilities in bismuth, Phys. Lett. A **28**, 435-436 (1968).

[35] S. Kochowski and A. Opilski, Concentration and mobility of charge carriers in thin polycrystalline films of bismuth, Thin Solid Films **48**, 345-351 (1978).

[36] F. Gity, L. Ansari, M. Lanius, P. Schüffelgen, G. Mussler, D. Grützmacher, and J. C. Greer, Reinventing solid state electronics: Harnessing quantum confinement in bismuth thin films, Appl. Phys. Lett. **110**, 093111 (2017).

[37] Y. Zabila, M. Marszalek, M. Krupinski, A. Zarzychi, and M. Perzanowski, Magnetotransport Properties of Semi-Metallic Bismuth Thin Films for Flexible Sensor Applications, Coatings **11**, 175 (2021).

[38] Z. Zhu, B. Fauqué, K. Behnia, and Y. Fuseya, Magnetoresistance and valley degree of freedom in bulk bismuth, J. Phys.: Condens. Matter **30**, 313001 (2018).

[39] Z. Zhu, J. Wang, H. Zuo, B. Fauqué, R.D. McDonald, Y. Fuseya, and K. Behnia, Emptying Dirac valleys in bismuth using high magnetic fields, Nat Commun. **8**, 15297 (2017).

[40] A. Iwasa, A. Kondo, S. Kawachi, K. Akiba, Y. Nakanishi, M. Yoshizawa, M. Tokunaga, and K. Kindo, Thermodynamic evidence of magnetic-field-induced complete valley polarization in bismuth, Sci. Rep. **9**, 1672 (2019).

[41] L. S. Lerner, Shubnikov-de Haas Effect in Bismuth, Phys. Rev. **127**, 1480 (1962).

[42] S. Otake, M. Momiuchi, and N. Matsuno, Temperature Dependence of the Magnetic Susceptibility of Bismuth, J. Phys. Soc. Jpn. **49**, 1824 (1980).

[43] B. C. Camargo, P. Gierłowski, A. Alaferdov, I. N. Demchenko, M. Sawicki, K. Gas, and Y. Kopelevich, Anomalous Hall effect in bismuth, J. Magn. Magn. Mater. **525**, 167581 (2021).

[44] M.-Y. Yao, F. Zhu, C. Q. Han, D. D. Guan, C. Liu, D. Qian, and J.-F. Jia, Topologically nontrivial bismuth(111) thin films, Sci. Rep. **6**, 21326 (2016).

[45] M.-Y. Liu, Y. Huang, Q.-Y. Chen, Z.-Y. Li, C. Cao, and Y. He, Strain and electric field tunable electronic structure of buckled bismuthene, RSC Adv. **7**, (2017).

[46] B. Roy and V. Juricic, Unconventional superconductivity in nearly flat bands in twisted bilayer graphene, Phys. Rev. B **99**, 121407(R) (2014).

[47] C.-C. Hsu, M. L. Teague, J.-Q. Wang, and N.-C. Yeh, Nanoscale strain engineering of giant pseudo-magnetic fields, valley polarization, and topological channels in graphene, Sci. Adv. **6**, (2020).

[48] Donovan and G. T. Conn, LXIX. The electrical conductivity of bismuth fibres: II. Anomalies in the magneto-resistance, The London, Edinburgh, and Dublin Philosophical Magazine and Journal of Science **41**, (1950).

[49] G. T. Conn and B. Donovan, Anomalous Magneto-Resistance Effects in Bismuth, Nature **162**, 336 (1948).

4.2.7 List of Figures

5

Temperature Independence of the Anomalous Hall Effect

5.1 Introduction

The previous report contains two particularly unexpected findings. The first is the discovery of the anomalous Hall effect in thin bismuth, suggesting the presence of a hidden mechanism that breaks time-reversal symmetry. This phenomenon was not anticipated, even when considering the 2D limit of the (111) surface of bismuth as discussed in Chapter 2. However, in 2023, a study revealed that inversion symmetry breaking at the surface can lead to a non-zero Berry curvature on the (111) surface [54]. This finding offers a potential path of explanation for the AHE observed in thin bismuth. Additionally, as we will discuss in Chapter 6, a hysteresis loop was found in the R_{xy}

signal which further supports a time-reversal breaking in our sample.

The other surprising finding in [53] was the absence of any significant magnetoresistance up to ± 9 T, the highest magnetic field available at the Gervais Lab at McGill. Although some very small, but inconclusive deviations from constant magnetoresistance were barely detectable in the XX pairs, it remains unclear whether magnetoresistance was truly absent or if the effect was too subtle to be resolved at ± 9 T. This uncertainty prompted the need to conduct experiments at higher magnetic fields. Consequently, the sample was brought to the National High Magnetic Field Laboratory (NHMFL) in Tallahassee, Florida, where fields of up to ± 30 T were accessible. Additionally, the resistive magnet at the NHMFL is equipped with a variable temperature insert (VTI), allowing for the investigation of temperature dependence as well.

As detailed in the manuscript below, we were once again surprised when the magnetoresistance showed no dependence with the magnetic field even up to ± 30 T. What was even more unexpected was that the experiments conducted at various temperatures, from 15 mK up to 300 K revealed almost no change in the AHE signal within the uncertainty. This strong temperature independence suggests that scattering and phonons likely do not contribute to the observed AHE, pointing instead to an intrinsic mechanism as the most plausible explanation.

The full manuscript presented below is entitled "Observation of Temperature Independent Anomalous Hall Effect in Thin Bismuth from Near Absolute Zero to 300 K Temperature". It is identical to the posted version on the *arXiv* [55] which has been submitted and is currently under review. In the Supplemental Material of the manuscript, shown in Appendix C, we further substantiate the intrinsic nature of the AHE through the analysis of the ratio $\Delta R_{\mathrm{AHE}}/R_{\mathrm{AHE}}(300K)$ versus temperature and the scaling equation shown in Eq. (2.24) discussed in Chapter 2. The figure labels and reference numberings are also aligned with those of the posted manuscript and are independent from the rest of the thesis.

5.2 Manuscript

5.2.1 Abstract

We report our discovery of a temperature independent anomalous Hall effect (AHE) from 15 mK to 300 K temperature occurring in a pure bismuth transport device whose average thickness is 68 nm. This surprising behaviour is accompanied with an expected temperature dependent longitudinal resistance consistent with semi-metallic bismuth, however it surprisingly showed no hint of a magnetoresistance for magnetic fields between ± 30 T. Even though bismuth is a diamagnetic material which *a priori* does not break time-reversal symmetry (TRS), our analysis of the reconstructed conductivities points towards the AHE to be of the intrinsic type, which does not emanate from magnetic impurities. Finally, as pure bismuth has been shown numerically to host a Berry curvature at its surface which breaks inversion symmetry, we propose it as a possible explanation for the temperature independent AHE observed here.

5.2.2 Introduction

Ever since Faraday's discovery of its diamagnetism in the mid-19$^{\text{th}}$ century, elemental bulk bismuth has been extensively studied and has been a wonder material for exploring new physical properties and phenomena such as the Shubnikov-de Haas (SdH), de Haas-van Alphen and Nernst–Ettingshausen effects. More recently, there has been a revival of experimental and theoretical work on single crystalline bismuth as it has demonstrated evidence for superconductivity at temperatures below $T_c \approx 0.5$ mK [1], as well as edge and hinge states that are consistent with models of higher-order topology [2, 3]. These discoveries make elemental bismuth an interesting platform for exploring exotic physical properties. For instance, a non-linear Hall effect was recently discovered in bismuth which showed tunability even at room temperature [4]. Additionally, being a material with high spin-orbit coupling, bismuth is known to host a buckled honeycomb lattice making it a suitable candidate to study the parity anomaly

predicted by Haldane [5].

While bismuth has been extensively studied in its bulk form, the exploration of its two-dimensional form has been limited due to fabrication challenges. Unlike graphite or other group V elements such as black phosphorus, the strong interlayer bonds make it difficult to mechanically exfoliate thin bismuth. Recent works on thin bismuth largely rely on molecular beam epitaxy (MBE) [6–8] or more creative methods such as the use of nano-molds [9] to press bulk bismuth down to 10 nm. These methods are not widely accessible compared to the simpler mechanical exfoliation, leaving the electronic transport properties of single crystal bismuth below 100 nm largely unexplored. In this letter, by making use of a newly developed mechanical exfoliation technique based on micro-trenches [10], we successfully fabricated thin bismuth devices and carried out transport measurements in a magnetic field B ranging from -30 T to 30 T and from near absolute zero to 300 K temperature. Strikingly, the anomalous Hall effect (AHE) discovered in our 68 nm van der Pauw (vdP) device [11] with an average thickness of 68 is found to be temperature independent, while the magnetoresistance is found to be entirely featureless. Both are remarkably surprising given the wide temperature range of investigation and the large applied magnetic fields.

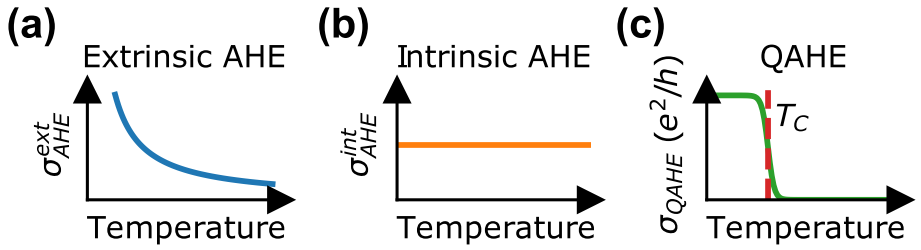

Figure 1: **(a)** Example of Hall conductivity due to the extrinsic contributions. Note that the $\sigma_{\mathrm{AHE}}^{ext}$ could be increasing or decreasing with temperature depending upon the material [17]. **(b)** Hall conductivity due to the intrinsic contribution. **(c)** Below the critical temperature T_C, the QAHE yields exactly one conductance quantum e^2/h per edge or surface state.

5.2.3 Anomalous Hall Effect

It is widely accepted in the literature that the total anomalous Hall conductivity (AHC) can be expressed as [12]

$$\sigma_{\mathrm{AHE}} = \sigma_{sk} + \sigma_{sj} + \sigma_{int}, \tag{5.1}$$

where σ_{AHE} is the total AHC and σ_{sk}, σ_{sj}, σ_{int} are the skew-scattering, side-jump, and intrinsic contributions respectively. One way to parse the mechanisms responsible for the AHE is to study how the AHC scales with the longitudinal conductivity $\sigma_{xx}(T)$ [12–15]. Since the skew-scattering and side-jump mechanisms both depend on impurities, the intrinsic contribution is, in principle, the only term that is temperature independent [16]. A hallmark of the intrinsic contribution σ_{int} is that it does not scale with the longitudinal conductivity $\sigma_{xx}(T)$ as described by the semi-empirical relation [12,14]

$$-\sigma_{\mathrm{AHE}}(T) = (\alpha\sigma_{xx0}^{-1} + \beta\sigma_{xx0}^{-2})\sigma_{xx}^{2}(T) + \sigma_{int}, \tag{5.2}$$

where α and β are coefficients for the skew-scattering and side-jump mechanisms, respectively, σ_{xx0} is the zero-field residual conductivity as $T \to 0$, and σ_{int} is the intrinsic AHC that remains constant. The expected temperature dependences for the extrinsic and intrinsic dominated AHE are shown in Fig. 1**(a)** and **(b)**, respectively. Depending on the material studied and the temperature range of investigation [17], the extrinsic AHE $\sigma_{\mathrm{AHE}}^{ext}$ can increase or decrease with temperature. For comparison, the expected temperature dependence for the QAHE is also shown in Fig. 1**(c)**. It is known that the intrinsic AHE is a precursor of the QAHE [14, 18, 19] which yields an anomalous conductance of exactly e^2/h per edge or surface state and is temperature independent below a critical temperature T_C [20].

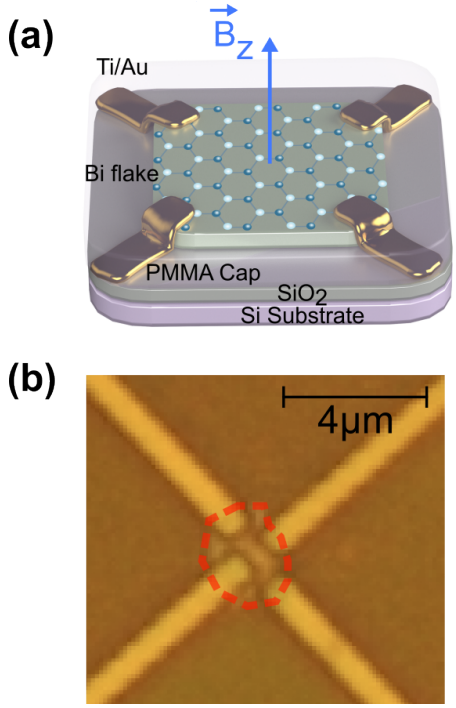

Figure 2: **(a)** Schematic of the device with an arrow showing the direction of the applied magnetic field $\vec{B}_z$. **(b)** Optical microscope image of the fabricated device where the flake is circled by the red dashed line.

5.2.4 Methods

Details of the fabrication process can be found in the *Supplemental Material* (SM) and in Yu *et al.* [10] which also includes the AHE observations in two other bismuth devices in a comb geometry with average thicknesses of 29 nm and 69 nm. The exfoliated bismuth flakes are produced in such way to favor its orientation in the (111) plane, as discussed in the SM. The illustration and the optical image of vdP device with an average thickness of 68 nm is shown in Fig. 2**(a)** and **(b)**, respectively (see SM for more details). Transport measurements (details found in the SM) are performed in a perpendicular magnetic field with field strengths up to ± 30 T and temperatures ranging from 1.4 K to 300 K in a resistive magnet. The lowest temperature data at $T = 15$ mK was measured between ± 9 T in a dilution refrigerator [11] showing identical behaviors [11] , though for the remainder of the manuscript, we will focus only on the 1.4 K to 300 K data as they were taken during a single cooldown.

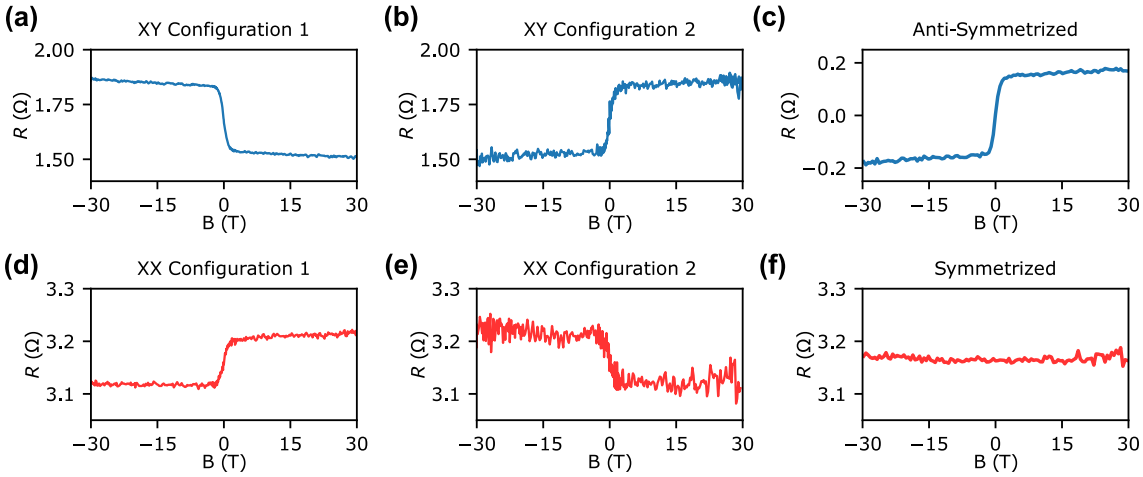

Figure 3: Resistances as a function of the magnetic field at $T = 1.4$ K. **(a)**, **(b)** Onsager configurations optimizing the XY or Hall measurements. **(d)**, **(e)**, Onsager configurations optimizing the XX or the longitudinal measurements. **(c)** Anti-symmetrized data that shows the extracted Hall resistance from the XY configurations shown in **(a)**, **(b)**. **(f)** Symmetrized data that shows the extracted longitudinal resistance from the XX configurations shown in **(d)**, **(e)**. Note that the noise in **(c)** and **(f)** are different due to the averaging process required for the anti-symmetrization and symmetrization.

5.2.5 Onsager Symmetrization

As shown in Fig. 2**(b)**, the Ohmic contacts deposited on the bismuth flake are located close to one another due to the small size of the flake. An ideal vdP geometry would have the contact electrodes located at each corner of a square sample, as depicted in the insets of Fig. 3, and this is not the case here. Consequently, in our measurements, the Hall (R_{xy}) and longitudinal (R_{xx}) resistances are inevitably mixed and are measured simultaneously regardless of the probe configuration. To remedy this, we made use of Onsager's reciprocity theorem [21] to reconstruct the Hall and longitudinal resistances, as discussed in detail in the SM.

The resistances as a function of the magnetic field were measured in two different Onsager pairs: one that maximizes the Hall signal (XY configurations 1 and 2) as shown in Fig. 3**(a)** and **(b)**, and one that maximizes the longitudinal signal (XX configurations 1 and 2) as shown in Fig. 3**(d)** and **(e)**. The XY Onsager pair's data was then anti-symmetrized to obtain the Hall resistance, shown in Fig. 3**(c)**. Similarly, the XX

Onsager pair's data was symmetrized to extract the longitudinal resistance, as shown in Fig. 3**(f)**.

5.2.6 Hall and Longitudinal Resistances

As previously reported [11] and as shown in Fig. 3**(c)**, the AHE is unambiguously observed in our elemental bismuth device. Hints of the AHE and/or anomaly in electronic magnetotransport occurring in bismuth fibres were reported in the 1940's by Conn and Donovan [22, 23], as well as recently in its bulk form by Camargo *et al.* [24] who eliminated the possibility of magnetic contaminants and speculated that the AHE arises from the surface. In bismuth thin films, the AHE has been demonstrated by Hirai *et al.* by opening a gap in bismuth's band structure with intense circularly polarized light [25]. Another more recent instance of the AHE in bismuth is in the work by Abdelbarey *et al.* [7] where the authors clearly observed a non-linearity of the Hall signal near zero-field.

Interestingly, in Partin *et al.*'s work on MBE-grown bismuth films [26], although it was overlooked by the authors, their 100 nm film displayed a Hall response and a completely featureless longitudinal response up to 17 T that agreed with what we have found in our 68 nm device between a magnetic field of ± 30 T (see Fig. 3**(f)**). While their film were unlikely to be protected by an encapsulating layer, all of our devices were capped by a PMMA layer in order to avoid oxidization and aging. These converging observations indicate that the AHE in elemental bismuth is genuine, yet as of today its exact mechanism remains unclear. Furthermore, it is not yet clear at what critical thickness bismuth thin films would exhibit a predominant AHE, but previous and current data would locate it in the vicinity of 100 nm.

The complete absence of magnetoresistance and SdH oscillations is particularly puzzling since diamagnetic and semi-metallic materials typically have a magnetoresistance that scales with B^2 [27–34]. Meanwhile, SdH oscillations were observed in bulk bismuth for magnetic fields as low as 1 T [35], and in a more recent work on growing 10 to

20 nm thin bismuth in nano-molds at magnetic fields as low as 5 T [9]. As pointed out in the SM and in our previous report at lower magnetic field [11], our observation of a featureless longitudinal magnetoresistance for magnetic fields between ± 30 T cannot be explained by a multi-carrier model and rather points toward an unknown mechanism being at play.

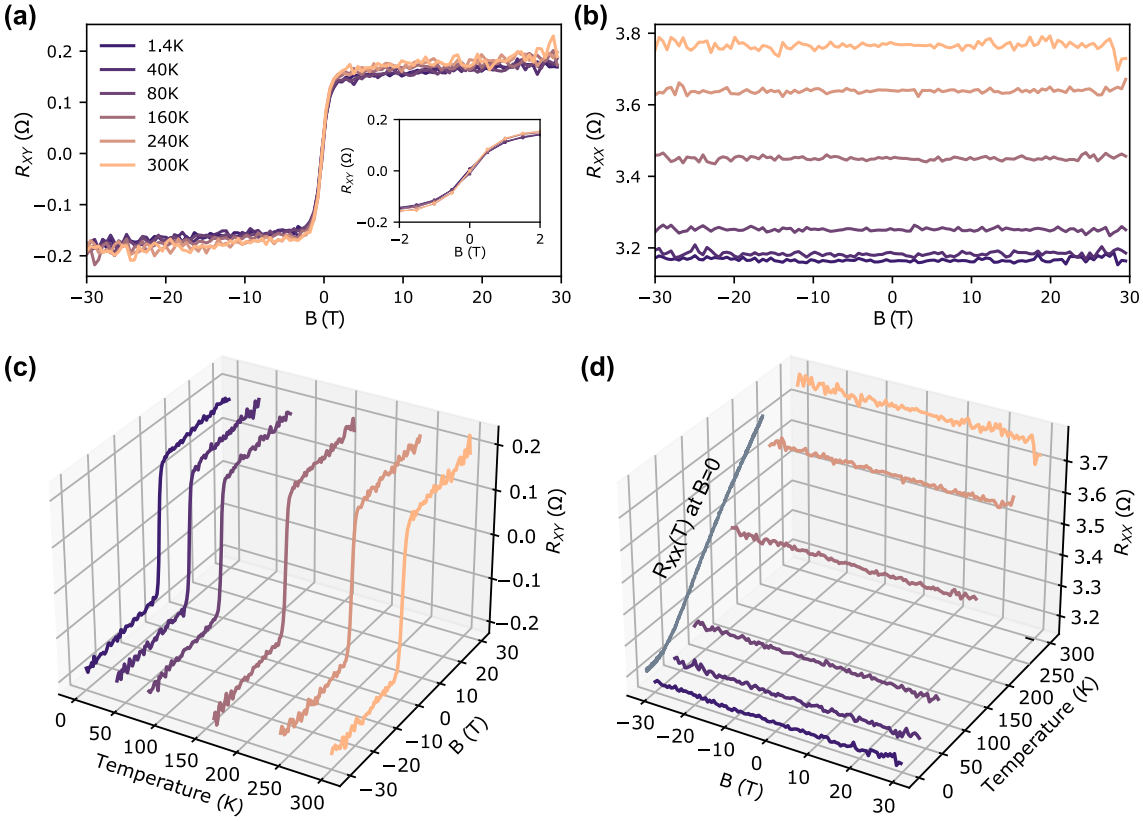

Figure 4: **(a)** Hall and **(b)** longitudinal resistances as a function of the magnetic field at various temperatures ranging from 1.4 K to 300 K. The inset in **(a)** is the zoom-in for the data between ± 2 T. **(c)**, **(d)**, 3D plots of the same curves in **(a)** and **(b)** respectively. The longitudinal resistance $R_{xx}(T)$ for the XX configuration 1 is shown in the background of **(d)** for comparison.

5.2.7 Temperature Independence of the AHE in Thin Bismuth

The main result of this work is shown in Fig. 4. The resistances versus magnetic field for all vdP configurations shown in Fig. 3 were measured at temperatures of 1.4 K, 40 K, 80 K, 160 K, 240 K and 300 K during a single cooldown. The Hall resistances R_{xy}

extracted via anti-symmetrization are shown in the main panel of Fig. 4**(a)** where the inset shows a zoom-in at magnetic fields between ± 2 T. The same R_{xy} data is shown in three dimensions in Fig. 4**(c)**. Similarly, the longitudinal resistance extracted from the XX Onsager pair is plotted in Fig. 4**(b,d)**. In Fig. 4**(d)**, the zero field ($B = 0$ T) temperature dependence of $R_{xx}(T)$ for the XX configuration 1 between 3 K and 260 K is shown in gray in the background. This increasing resistance with increasing temperature is consistent with the semi-metallic nature of bulk and thin bismuth [26, 36, 37].

Most strikingly, our data shown in Fig. 4**(a,c)** demonstrates the observed AHE to be, within noise, entirely independent of temperature. The negligible temperature dependence is particularly notable in the low field region of $|B| < 2$ T where the $R_{xy}(B)$ data completely overlap for all temperatures investigated. This was further verified down to 15 mK in a dilution refrigerator during a separate cooldown [11]. In the high field regions where the AHE is saturated, the anomalous Hall resistance R_{AHE} can be extracted via the zero field intercept of a linear fit (see SM). At first sight, this lack of temperature dependence may seem surprising. However, an important feature of the intrinsic AHE is that it is temperature independent [12, 14], as illustrated in Fig. 1**(b)**. This is further expected in our case since the estimated longitudinal conductivity of our device is in the good-metal regime $\sigma_{xx} \sim 10^4 - 10^6\ \Omega^{-1}\,\mathrm{cm}^{-1}$, which is typical for materials exhibiting an AHE that is intrinsic in nature [14]. Furthermore, our analysis on the relation found in Eq. (5.2) (see SM) shows the proper linear scaling between $-\sigma_{\mathrm{AHE}}$ and σ_{xx}^2, further pointing the observed AHE towards the intrinsic type.

The underlying mechanism of the AHE in bismuth is, in our view, unlikely due to magnetism of any kind given the lack of temperature dependence. Furthermore, as discussed in more detail in the SM, elemental bismuth is known to be a diamagnetic material which *a priori* does not break TRS and has a relatively weak temperature dependent susceptibility that varies by a factor of two from 540 K to low temperatures [38]. In contrast, an intrinsic AHE can originate from a non-zero Berry curvature [13, 14] with the necessary condition of breaking either TRS or inversion symmetry (IS) [39]. In bismuth, IS is preserved in the bulk but broken at the surface [40], thus a non-zero Berry

curvature could be present at the surface without breaking TRS. Recent first principle calculations by Wawrzik *et al.* [54] confirmed this by showing that while bismuth has a zero Berry curvature in the bulk, its surface nevertheless hosts a non-zero Berry curvature. This serves as the basis for understanding the room temperature non-linear Hall effect observed very recently by Makushko et al. [4]. We propose that bismuth's non-zero Berry curvature at its surface could explain the temperature independent AHE observed in our work. Future theoretical and experimental work is nevertheless required to pinpoint and gain knowledge on the exact mechanism being here at play.

5.2.8 Conclusion

In this work, we measured the resistances of a bismuth transport device with an average thickness of 68 nm in different vdP configurations for magnetic fields between ± 30 T and temperatures between 15 mK and 300 K. The extracted longitudinal resistance was observed to be completely featureless for all investigated temperatures. The extracted Hall resistance clearly demonstrates an anomaly consistent with the anomalous Hall effect, and was observed to be entirely independent of temperature. Most, if not all mechanisms, except for the Berry curvature responsible for the intrinsic AHE, are temperature dependent in the range of investigation. We are unaware of any model that could explain simultaneously the observed Hall and longitudinal signals, nor any other material that exhibit an electronic Hall transport that is so insensitive to temperature for such a wide range. This makes bismuth an intriguing material that is still not well understood. Looking forward, given that intrinsic AHE is the precursor of QAHE [18, 19], we speculate whether bismuth could be a suitable platform to explore the QAHE given its buckled honeycomb crystal structure and high spin-orbit coupling, both being important ingredients for the parity anomaly predicted by Haldane [5]. If this is the case for bismuth, then this also raises the fascinating question of whether the QAHE could be observable at much higher temperatures than it currently has been.

5.2.9 References

[1] O. Prakash, A. Kumar, A. Thamizhavel, and S. Ramakrishnan, Evidence for bulk superconductivity in pure bismuth single crystals at ambient pressure, Science **355**, 52(2017).

[2] L. Aggarwal, P. Zhu, T. L. Hughes, and V. Madhavan, Evidence for higher order topology in Bi and Bi0.92Sb0.08, Nat. Commun. **12**, 4420 (2021).

[3] F. Schindler, Z. Wang, M. G. Vergniory, A. M. Cook, A. Murani, S. Sengupta, A. Y. Kasumov, R. Deblock, S. Jeon, I. Drozdov, H. Bouchiat, S. Guéron, A. Yazdani, B. A. Bernevig, and T. Neupert, Higher-order topology in bismuth, Nat. Phys. **14**, 918 (2018).

[4] P. Makushko, S. Kovalev, Y. Zabila, I. Ilyakov, A. Ponomaryov, A. Arshad, G. L. Prajapati, T. V. A. G. de Oliveira, J.-C. Deinert, P. Chekhonin, I. Veremchuk, T. Kosub, Y. Skourski, F. Ganss, D. Makarov, and C. Ortix, A tunable room-temperature nonlinear Hall effect in elemental bismuth thin films, Nat. Electron. **7**, 207 (2024).

[5] F. D. M. Haldane, Model for a Quantum Hall Effect without Landau Levels: Condensed-Matter Realization of the "Parity Anomaly", Phys. Rev. Lett. **61**, 2015 (1988).

[6] S.-Y. Yang, K. Chang, and S. S. P. Parkin, Large planar Hall effect in bismuth thin films, Phys. Rev. Research **2**, 022029(R) (2020).

[7] D. Abdelbarey, J. Koch, Z. Mamiyev, C. Tegenkamp, and H. Pfnür, Thickness-dependent electronic transport through epitaxial nontrivial Bi quantum films, Phys. Rev. B **102**, 115409 (2020).

[8] D. Abdelbarey, J. Koch, P Kröger, P. Yogi, C. Tegenkamp, and H. Pfnür, Magnetoconductance in epitaxial bismuth quantum films: Beyond weak (anti)localization, Phys. Rev. B **104**, 075431 (2021).

[9] L. Chen, A. X. Wu, N. Tulu, J. Wang, A. Juanson, K. Watanabe, T. Taniguchi, M. T. Pettes, M. A. Campbell, M. Xu, C. A. Gadre, Y. Zhou, H. Chen, P. Cao, L. A. Jauregui, R. Wu, X. Pan, and J. D. Sanchez-Yamagishi, Exceptional electronic transport and quantum oscillations in thin bismuth crystals grown inside van der Waals materials, Nat. Mater. **23**, 741 (2024).

[10] O. Yu, R. Allgayer, S. Godin, J. Lalande, P. Fossati, C. Hsu, T. Szkopek, and G. Gervais, Method of mechanical exfoliation of bismuth with micro-trench structures, J. Appl. Phys. **134**, 244302 (2023).

[11] O. Yu, S. Vijayakrishnan, R. Allgayer, T. Szkopek, and G. Gervais, Anomalous Hall effect in thin bismuth, Phys. Rev. B **109**, L121406 (2024).

[12] Y. Tian, L. Ye, and X. Jin, Proper Scaling of the Anomalous Hall Effect, Phys. Rev. Lett. **103**, 087206 (2009).

[13] D. Culcer, in *Encyclopedia of Condensed Matter Physics (Second Edition)*, edited by T. Chakraborty (Academic Press, 2024), Vol. 1, p. 587.

[14] N. Nagaosa, J. Sinova, S. Onoda, A. H. MacDonald, and N. P. Ong, Anomalous Hall effect, Rev. Mod. Phys. **82**, 1539 (2010).

[15] S. Onoda, N. Sugimoto, and N. Nagaosa, Intrinsic Versus Extrinsic Anomalous Hall Effect in Ferromagnets, Phys. Rev. Lett. **97**, 126602 (2006).

[16] A. Shitade, and N. Nagaosa, Anomalous Hall Effect in Ferromagnetic Metals: Role of Phonons at Finite Temperature, J. Phys. Soc. Jpn **81**, 083704 (2012).

[17] T. Miyasato, N. Abe, T. Fujii, A. Asamitsu, S. Onoda, Y. Onose, N. Nagaosa, and Y. Tokura, Crossover Behavior of the Anomalous Hall Effect and Anomalous Nernst Effect in Itinerant Ferromagnets, Phys. Rev. Lett. **99**, 086602 (2007).

[18] H. Weng, R. Yu, X. Hu, X. Dai, and Z. Fang, Quantum anomalous Hall effect and related topological electronic states, Adv. Phys **64**, 227(2015).

[19] C.-X. Liu, S.-C. Zhang, and X.-L. Qi, The Quantum Anomalous Hall Effect: Theory and Experiment, Annu. Rev. Condens. Matter. Phys. **7**, 301 (2016).

[20] C.-Z. Chang, C.-X. Liu, and A. H. MacDonald, Colloquium : Quantum anomalous Hall effect, Rev. Mod. Phys. **95**, 011002 (2023).

[21] H. H. Sample, W. J. Bruno, S. B. Sample, and E. K. Sichel, Reverse-field reciprocity for conducting specimens in magnetic fields, J. Appl. Phys. **61**, 1079 (1987).

[22] B. Donovan, and G. K. T. Conn, LXIX. The electrical conductivity of bismuth fibres: II. Anomalies in the magneto-resistance, The London, Edinburgh, and Dublin Philosophical Magazine and Journal of Science **41**, 770 (1950).

[23] G. K. T. Conn, and B. Donovan, Anomalous Magneto-Resistance Effects in Bismuth, Nature **162**, 336 (1948).

[24] B. C. Camargo, P. Gierłowski, A. Alaferdov, I. N. Demchenko, M. Sawicki, K. Gas, and Y. Kopelevich, Anomalous Hall effect in bismuth, J. Magn. Magn. Mater. **525**, 167581 (2021).

[25] Y. Hirai, N. Yoshikawa, M. Kawaguchi, M. Hayashi, S. Okumura, T. Oka, and R. Shimano, Anomalous Hall effect of light-driven three-dimensional Dirac electrons in bismuth, arXiv:2301.06072, (2023).

[26] D. L. Partin, J. Heremans, D. T. Morelli, C. M. Thrush, C. H. Olk, and T. A. Perry, Growth and characterization of epitaxial bismuth films, Phys. Rev. B **38**, 3818-3824 (1988).

[27] M. Cabrera-Baez, K. V. R. A. Silva, P. R. T. Ribeiro, D. R. Ratkovski, E. L. T. França, A. Flessa-Savvidou, B. Casas, T. Siegrist, L. Balicas, S. M. Rezende, and F. L. A. Machado, Giant magnetoresistance in the crystalline YCd_6 intermetallic compound, Phys. Rev. B **107**, 144414 (2023).

[28] J. Juraszek, L. Bochenek, A. Rudenko, M. M. Hosen, M. Daszkiewicz, Z. Wang, J. Wosnitza, Z. Henkie, M. Samsel-Czekała, M. Neupane, and T. Cichorek, Nonsat-

urating extreme magnetoresistance and large electronic magnetostriction in LuAs, Phys. Rev. Research **1**, 032016(R) (2019).

[29] I. A. Leahy, Y.-P. Lin, P. E. Siegfried, A. C. Treglia, J. C. W. Song, R. M. Nandkishore, and M. Lee, Nonsaturating large magnetoresistance in semimetals, Proc. Natl. Acad. Sci. **115**, 10570 (2018).

[30] T. Liang, Q. Gibson, M. N. Ali, M. Liu, R. J. Cava, and N. P. Ong, Ultrahigh mobility and giant magnetoresistance in the Dirac semimetal Cd3As2, Nat. Mater. **14**, 280 (2014).

[31] M. N. Ali, J. Xiong, S. Flynn, J. Tao, Q. D. Gibson, L. M. Schoop, T. Liang, N. Haldolaarachchige, M. Hirschberger, N. P. Ong, and R. J. Cava, Large, non-saturating magnetoresistance in WTe2, Nature **514**, 205 (2014).

[32] C. Shekhar, A. K. Nayak, Y. Sun, M. Schmidt, M. Nicklas, I. Leermakers, U. Zeitler, Y. Skourski, J. Wosnitza, Z. Liu, Y. Chen, W. Schnelle, H. Borrmann, Y. Grin, C. Felser, and B. Yan, Extremely large magnetoresistance and ultrahigh mobility in the topological Weyl semimetal candidate NbP, Nat. Phys. **11**, 645 (2015).

[33] N. Kumar, Y. Sun, N. Xu, K. Manna, M. Yao, V. Süss, I. Leermakers, O. Young, T. Förster, M. Schmidt, H. Borrmann, B. Yan, U. Zeitler, M. Shi, C. Felser, and C. Shekhar, Extremely high magnetoresistance and conductivity in the type-II Weyl semimetals WP2 and MoP2, Nat. Commun. **8**, 1642 (2017).

[34] F. F. Tafti, Q. D. Gibson, S. K. Kushwaha, N. Haldolaarachchige, and R. J. Cava, Resistivity plateau and extreme magnetoresistance in LaSb, Nat. Phys. **12**, 272 (2015).

[35] L. S. Lerner, Shubnikov-de Haas Effect in Bismuth, Phys. Rev. **127**, 1480 (1962).

[36] R. A. Hoffman, and D. R. Frankl, Electrical Transport Properties of Thin Bismuth Films, Phys. Rev. B **3**, 1825 (1971).

[37] C. A. Kukkonen, and K. F. Sohn, The low-temperature electrical resistivity of bismuth, J. Phys. F: Met. Phys. **7**, L193 (1977).

[38] S. Otake, M. Momiuchi, and N. Matsuno, Temperature Dependence of the Magnetic Susceptibility of Bismuth, J. Phys. Soc. Jpn **49**, 1824 (1980).

[39] D. Xiao, M.-C. Chang, and Q. Niu, Berry phase effects on electronic properties, Rev. Mod. Phys. **82**, 1959 (2010).

[40] P. Hofmann, The surfaces of bismuth: Structural and electronic properties, Prog. Surf. Sci. **81**, 191 (2006).

[41] D. Wawrzika, J. I. Facioa, and J. van den Brink, Surface induced electronic Berry curvature in bulk Berry curvature free materials, Mater. Today Phys. **33**, 101027 (2023).

5.2.10 List of Figures

6

Discussion

In this chapter, I offer a comprehensive overview of the key findings, discuss the limitations encountered during research, and propose potential avenues for future investigation.

6.1 Mechanical Exfoliation and Device Fabrication

Chapter 2 highlighted the critical role of surface states in bismuth, where the significant departure in its band structure from the bulk gives rise to intriguing and unexplored properties. Given our laboratory's expertise in low temperature and high magnetic fields, we are naturally inclined to investigate the electronic transport properties of bismuth in the 2D limit.

The first manuscript presented in Chapter 3 laid the groundwork for obtaining high quality thin flakes of bismuth that are suitable for transport measurements, where these

results are presented in Chapter 4 and Chapter 5. This was a crucial development for our research, as discussed, because bottom-up approaches for obtaining thin bismuth flakes can be both financially difficult and time consuming, requiring extensive optimization to achieve high quality films. While many research groups have explored top-down approaches for producing thin bismuth flakes, these methods have also proved challenging and can result in quality degradation. Our technique, which employs a micro-trench structure to facilitate mechanical exfoliation, is highly effective due to its relatively low cost and ease of reproduction. Notably, this exfoliation method is not limited to bismuth and could be applied to a variety of 2D materials. Additionally, the use of a SiO_2 substrate to induce mechanical stress on bulk crystals is not a strict requirement. Other substrates may also be used, provided they are harder than the crystal used for exfoliation.

During the fabrication, preserving the high quality crystalline structure of the exfoliated thin flakes for subsequent transport measurements is equally important. While this is not trivial given the mechanical stress involved in exfoliation, we are confident that the crystalline quality has been maintained in the thin bismuth flakes. As discussed in Chapter 3, we used a high purity single crystal for exfoliation, carefully orienting the bulk bismuth glued to the pen along the (111) plane which is the natural cleavage plane. The Raman spectra of our exfoliated thin flakes exhibited shifts consistent with those of the bulk bismuth crystal, aligning with the spectra reported for 6–50 nm bismuth films grown in the (111) direction [56].

One might also question whether defects were introduced during exfoliation given the stronger interlayer bonding in bismuth. Investigating these potential defects is crucial for assessing the quality of the flakes, and this should be a focus of future work. For example, transmission electron microscopy (TEM) could be used to image the surface. However, this analysis was not performed in this thesis due to the complexity of sample preparation. The process requires capping the samples with a hard metal layer like tungsten, ion milling a cross-sectional slice through the bismuth flake, and finally polishing the surface with ions or electrons. Developing such a process for the compar-

atively 'soft' bismuth films, along with conducting control experiments to ensure that the TEM sample preparation does not introduce artifacts, was unfortunately beyond the scope of this project.

The exfoliated thin flakes are subsequently used to fabricate transport devices. The numerous challenges associated with the fabrication process, including characterization, patterning, gate leakage and contact resistance, were not covered in any of the manuscripts, but are crucial for future work. Therefore, we dedicate Appendix D to detailing these aspects, providing future researchers with the information needed to reproduce the results as efficiently as possible.

It is important to re-emphasize that both the exfoliation and characterization processes are conducted within a nitrogen glovebox to prevent humidity and oxidation. When substrates with flakes are removed from the glovebox, they are always coated with PMMA as a protective cap layer. Even the lift-off process following metal deposition is carried out inside the glovebox. Notably, there is only one instance where the bismuth flakes come into contact with air: during the development of the PMMA resist after the electron beam lithography (EBL) process. To minimize potential damage from this exposure, we transfer the substrate to the metal deposition machine as quickly as possible and immediately pump the chamber to vacuum. This approach has been effective in our group's previous work with black phosphorus [57], which is known to be highly unstable in ambient conditions involving air, O_2, and light. Based on this experience, we are confident that our bismuth devices did not suffer from oxidation. Indeed, as discussed in Chapter 3, Raman spectra showed no evidence of oxidation in our bismuth devices. Moreover, experiments conducted at intervals ranging from months to two years have shown no signs of aging effects.

Another logical question to consider is why no device was fabricated with flakes of smaller thickness when the thinnest flake reported in Chapter 3 was $\sim$2 nm. The challenge arises from the fact that, as the bismuth flakes become thinner, their areas unfortunately tend to become smaller as well. As such, the fabrication of devices becomes difficult, particularly in the four-terminal configuration, although it is not impossible.

Additionally, thinner flakes tend to exhibit very high contact resistance, resembling that of a Schottky barrier. While current annealing can improve the contact resistance, it is not sufficient unless a large amount of current is used. Unfortunately, this approach is not systematic, and we were unable to investigate it thoroughly.

In summary, the innovative method of using micro-trenches as a tool for mechanically exfoliating thin bismuth flakes has facilitated the fabrication of thin bismuth electronic transport devices. This approach has established a foundation for our future work where the transport properties of thin bismuth are explored.

6.2 Comparison with MBE-grown films

In the manuscript reporting the anomalous Hall effect and the subsequent manuscript reporting on its temperature independence, we consistently compared our results to those of Partin *et al.* [58]. In this section, we explicitly present their results to enable the direct comparison with our data, as discussed in Chapter 4 and Chapter 5. The original data from Partin *et al.* is shown below in Fig. 6.1.

In particular, we observe that the magnetotransport behavior of the 100 nm MBE-grown film reported by Partin *et al.* remarkably resembles ours at low temperatures. In fact, a digitalization of their Hall data reveals an AHE feature that is quantitatively similar to ours, including the saturating field of ~ 1 T and the ratio between the saturated $R_{xy}(B \gg 1)$ and R_{xx}. Notably, this ratio is approximately to 12% in Partin *et al.*'s work, and 11% in our work using the data symmetrized and anti-symmetrized from the XY configurations.

In addition, the magnetoresistivity for the 100 nm bismuth film shown in Fig. 6.1 is also completely featureless up to 17 T, identical to our data. Note that, as it is already discussed in Chapter 4, the multi-carrier model cannot reconcile both the R_{xy} and R_{xx} behaviors simultaneously. This limitation is not only theoretical but also practical, as the featureless R_{xx} prevents us from fitting the appropriate parameters for both the Hall resistance and the magnetoresistance. This has been attempted numerous times without

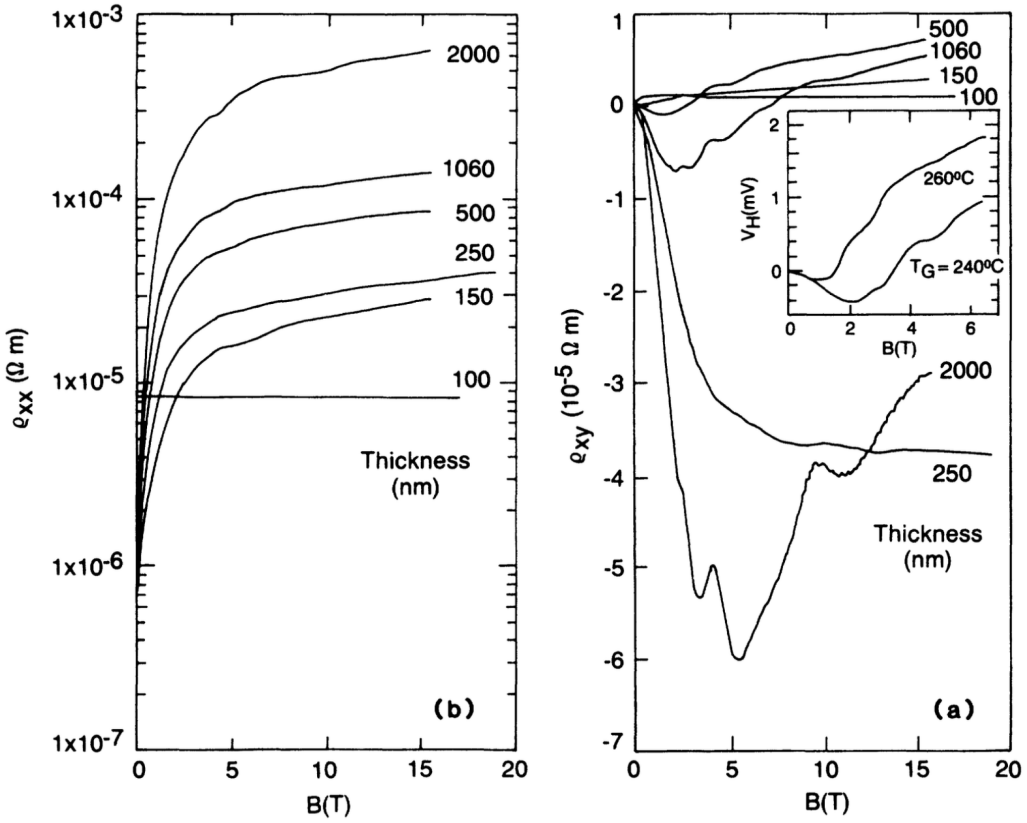

Figure 6.1: Original data from Partin *et al.* [58]. The left panel is the magnetoresistivity $\rho_{xx}(B)$ and the right panel is the Hall resistivity $\rho_{xy}(B)$. The figure is reproduced with permission from Reference [58].

success.

In the first report of the AHE in bismuth (Chapter 4), we did not comment on any geometrical effects which could occur. However, in our small $1\mu\text{m} \times 1\mu\text{m}$ device, we measured R_{xy} in various configurations without noting an explicit geometric contribution. This, along with the comb devices discussed in Appendix B, led us to conclude that geometric effects can be considered negligible. Note that in Partin *et al.*'s case, the geometry was an active channel of $40\mu\text{m} \times 200\mu\text{m}$, which is significantly larger than ours, yet they reported magnetotransport properties that are strikingly similar to ours in their 100 nm film.

In Fig. 6.1, it can be seen that thickness has important consequences on the measured Hall data. In the three bismuth devices we measured with varying thicknesses

(averaging from 29 to 69 nm), we did not observe a sign change in the Hall signal in contrast to Partin *et al.*'s work. This discrepancy may be attributed to differences in fabrication techniques; however, additional samples need to be prepared to draw definitive conclusions about thickness-dependent Hall resistance sign changes. Moreover, a key difference between these MBE films and our devices is that the former are not single crystals. In contrast, we used a single crystal with purity greater than 99% for mechanical exfoliation, rendering our exfoliated flakes likely to be single crystals.

Despite these differences, the convergence of results with samples fabricated in entirely different ways certainly points toward the *bona fide* nature of the AHE observed in the 100 nm film and at thicknesses less than 100 nm in our own work. It is not clear whether there is a critical thickness, and a subject of future work should be identifying a better estimate of this critical thickness. Meanwhile, the critical thickness for the SMSC transition was previously reported, but has discrepant conclusions depending on the study [59–61]. Indeed, the SMSC transition remains a controversial topic. However, in our system, based on our temperature dependence of the devices' resistance, we have strong reasons to believe that our devices are in the semi-metallic regime.

6.3 Geometric Factors and Extraction of Hall conductivity

In principle, Eq. (2.24) or Eq. (2.25) can be used to extract the intrinsic anomalous Hall resistivity or conductivity. However, this was not discussed in our manuscript (Chapter 5), nor in the Supplemental Material presented in Appendix C. Instead, Eq. (2.24) and Eq. (2.25) were only analyzed through dimensionless quantities that do not involve geometry factors. The reason for this omission is that we cannot extract the resistivity or conductivity in a reliable fashion.

A primary issue is that the flake has uneven thickness. However, we would like to emphasize that this height variation is unlikely to undermine the validity of our conclusions. Specifically, as mentioned in Chapter 2, size quantization effects are chal-

lenging to observe in bismuth. This is because the metallic surface states on Bi (111) likely contribute a density of states (and thus conductivity) that dominates over the bulk. Consequently, one does not observe a trivial decrease in conductivity due to a gap opening in the bulk for ultra-thin films.

If the charge transport was indeed dominated by a surface state, then it could be the bottom surface that predominates conduction over both the bulk and the non-uniform surface above. Thus, the actual thickness is less critical as long as it is "thin enough" that the bulk does not dominate. This is further confirmed by the observation of the AHE in the comb devices. All three devices, in which we found the AHE, have different average thicknesses ranging from 29 nm to 69 nm.

A more significant issue is that the vdP theorem cannot be applied here, given that the contacts must be infinitesimally small and positioned on the boundary of the flake. Moreover, a closer examination of the optical image of the device reveals that its geometry resembles a Greek cross rather than the idealized vdP configuration due to the large size of contacts compared to the flake. This geometric discrepancy, which is briefly mentioned in Chapter 2, impacts our analysis. As a result, we analyze the resistivities ρ_{xx} and ρ_{xy} using three different approaches: the standard conversion formula given in Eq. (6.1), the vdP method, and a formula adapted for the Greek cross geometry.

Usually, we can convert from resistance to resistivity via

$$\rho_{xx} = \frac{R_{xx}A}{l} \approx R_{xx}t, \tag{6.1}$$

where R is the bulk resistance, ρ is the bulk resistivity, $A = wt$ is the area, w is the width, l is the length and t is the thickness. Note that the approximation in Eq. (6.1) assumes the flake is nearly square, as observed in the optical image.

In the vdP geometry, the calculation of ρ_{xx} would require using Eq. (2.26), where Eq. (2.27) is used to calculate the factor f. However, calculations show that $f \approx 1$ regardless of the configuration pairs (XX or XY) used. It is important to note that

applying the vdP theorem would yield ρ_{xx} values approximately 3-4 times larger than those obtained using the standard conversion in Eq. (6.1).

Additionally, an extension of the vdP geometry for finite contact size is the Greek cross geometry [35,36]. In this case, the geometric factors are different and are given by the equations

$$\rho_{xy} = \frac{1}{D(\lambda)} R_{xy} t \tag{6.2a}$$

$$\rho_{xx} = C(\lambda) R_{xx} t, \tag{6.2b}$$

where the parameters $\lambda = 0.8$, $D(\lambda) = 0.13$ and $C(\lambda) = 11.57$ are fitted numerically [35,36].

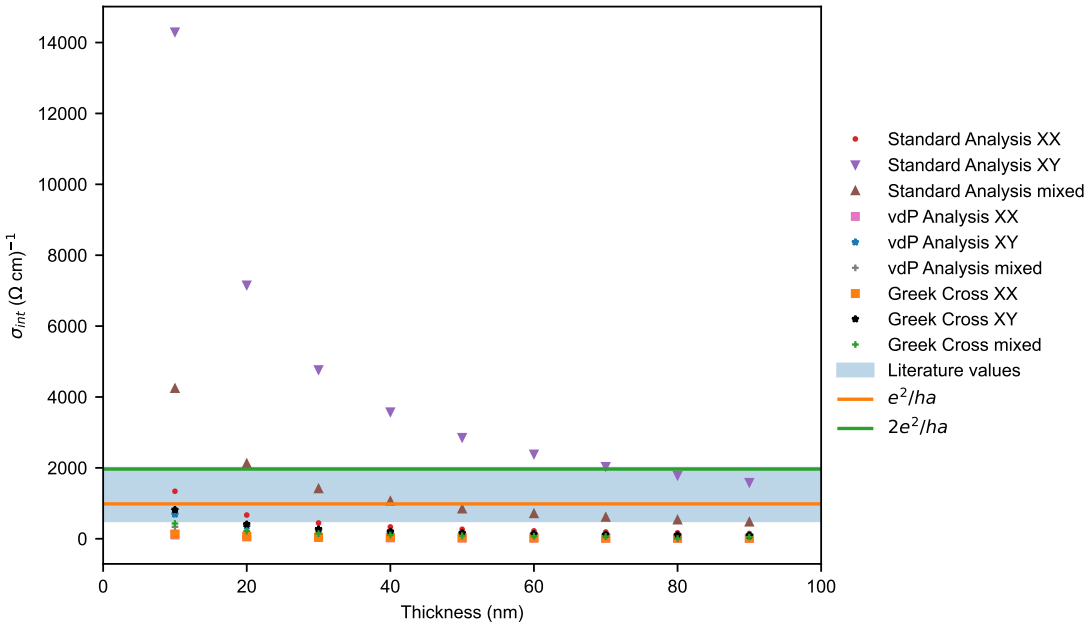

Figure 6.2: Assuming different thicknesses of the flake, σ_{int} is calculated from a 3D model using different XX pair and XY pair combinations, and ρ_{xx} and ρ_{xy} are converted from R_{xx} and R_{xy} using various methods.

We can convert the resistance to resistivity with these three methods and then calculate σ_{xy} which leads to σ_{int} defined as the y-intercept of linear fit to the saturated part of $\sigma_{xy}(B)$. However, σ_{xy} is calculated using tensor inversion from ρ_{xx} and ρ_{xy}. Since both the XX pair and XY pair can yield the even R_{xx} and the odd R_{xy} components after sym-

metrization and anti-symmetrization, determining the appropriate combination to use is unclear. Additionally, due to the uneven thickness of the flake, selecting the correct thickness is not trivial. We summarize these different combinations in Fig. 6.2

The values for $e^2/(ha)$ and $2e^2/(ha)$ are plotted in Fig. 6.2, where a was taken to be the lattice constant of bismuth perpendicular to the (111) plane. For comparison, the range of reported values for σ_{int} in the literature are also clearly shown [21]. From Fig. 6.2, it appears that only the standard conversion formula using Eq. (6.1) is consistent with literature values.

For completeness, we also examine the 2D model and compare it to e^2/h and $2e^2/h$, as shown in Fig. 6.3. The right panel of this figure provides a zoomed-in view of the left panel. In this model, it appears that the vdP method or the Greek cross method might be a better choice.

It is therefore challenging to draw a sound conclusion given the non-trivial flake geometry and the various possible considerations, including: (1) whether a 2D or 3D model should be used, (2) whether the conversion from R to ρ should use a standard formula, the vdP method or Greek cross method, and (3) which combination of the symmetrized R_{xx} and anti-symmetrized R_{xy} should be used, given that both the XX and XY pairs produce these values. These uncertainties highlight the need for fabricating new bismuth devices with geometry and sample thickness more suitable for a confident reconstruction of the resistivity.

6.4 Hysteresis Loop

As discussed numerous times in this thesis, time-reversal symmetry is a necessary ingredient for the anomalous Hall effect to occur. For the this reason, we concluded in our second manuscript, presented in Chapter 4, that there must exist a hidden mechanism for the TRS breaking. While we have learned more since its publication, the exact mechanism remains unknown. Nevertheless, we have observed a direct evidence of the TRS breaking in our system.

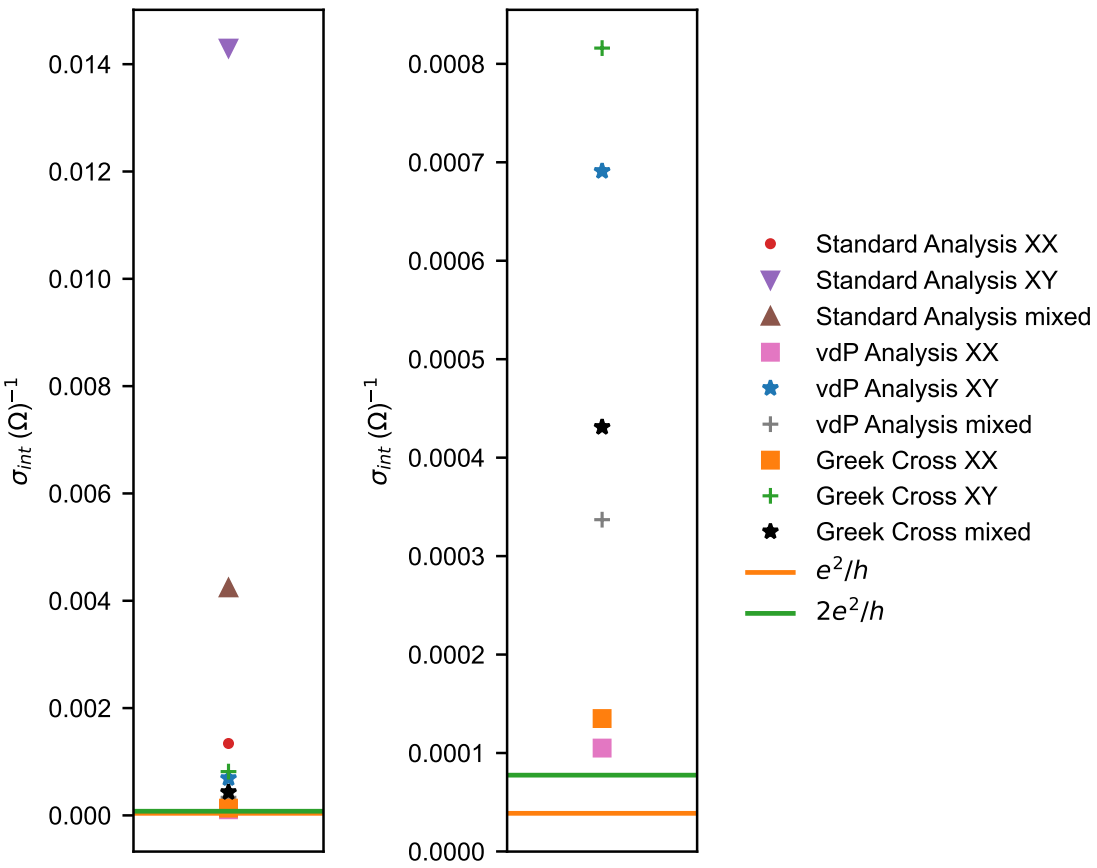

Figure 6.3: σ_{int} is calculated from a 2D model using different XX pair and XY pair combinations, where ρ_{xx} and ρ_{xy} are converted from R_{xx} and R_{xy} using various methods.

This was not trivial, and overlooked in our paper given that the hysteresis loop is small. Hence, the signal-to-noise ratio had to be significantly improved in order to properly resolve the hysteresis loop. For this reason, the investigation of the hysteresis loops required the magnetic field to be swept extremely slow, rendering us to only collect data between ± 1 T given the time limitations. We show below, for our least noisy configuration (XY1), the clear hysteresis that was found.

The same investigations were performed for all other configurations, specifically the XY2, XX1 and XX2 configurations. Importantly, in all configurations, the hysteresis was clearly observed, despite the XX configurations tended to be more noisy. Furthermore, it was found that the size of the hysteresis was independent of the sweep rate — the slowest sweep was more than a full day, while the fastest sweep was completed in

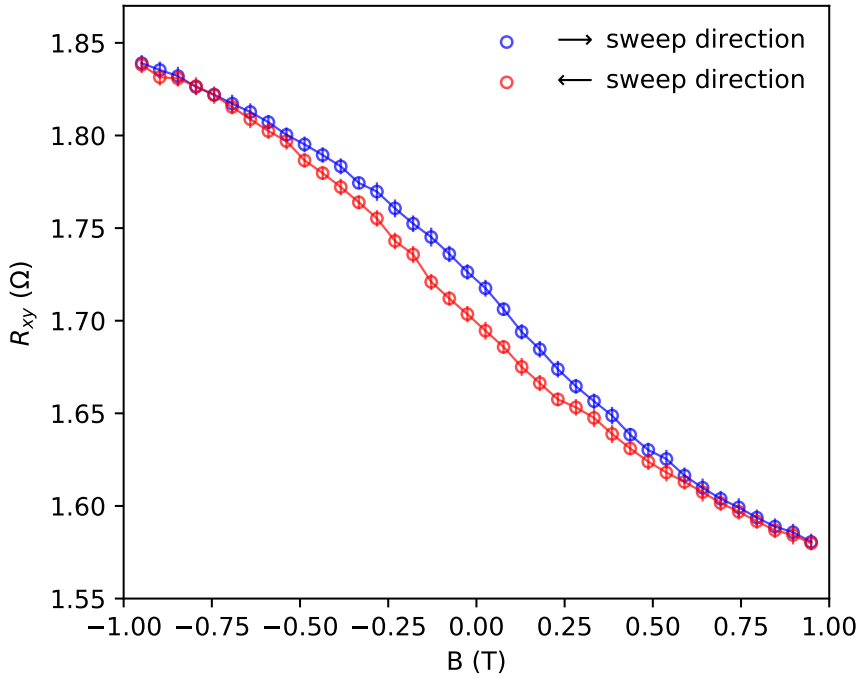

Figure 6.4: The hysteresis resolved for for the XY1 configuration. Note that the error bars are given by the standard deviation.

less than 30 min.

6.5 Summary

This chapter includes several supplementary yet crucial discussions related to the results presented earlier in this thesis. We document many challenges encountered during the fabrication process and suggest possible improvements. Appendix D is dedicated to these aspects. We also provide a thorough comparison with previous MBE-grown works, particularly those of Partin *et al.*. The intrinsic anomalous Hall conductivity was extracted based on various models, yet the existence of many kinds of models renders it difficult to draw an affirmative conclusion. Finally, we present the direct evidence that TRS is broken in our thin bismuth system through the observation of a hysteresis loop.

These additional discussions motivate several potential improvements. In the fol-

lowing concluding chapter of this thesis, we will address possible future research directions to further investigate the unexpected AHE in bismuth.

7

Conclusion

7.1 Conclusion

Motivated by the exotic and largely unexplored electronic transport properties of bismuth in the 2D limit, we present a novel method of mechanical exfoliation using a micro-trench structure to obtain ultra-thin bismuth flakes for the study of transport measurements. By applying this technique to single crystal bulk bismuth, we demonstrate that mechanical stress concentration can effectively cleave bismuth along the (111) plane, producing flakes as thin as 2 nm. From these flakes, we fabricated bismuth transport devices with average thicknesses ranging from 29 nm to 69 nm in both van der Pauw and comb geometries.

Remarkably, we unexpectedly observed the anomalous Hall effect in all devices, with extensive transport measurements conducted on a van der Pauw device with an

average thickness of 68 nm where the contacts remained ohmic throughout the entire range of investigated temperatures. Notably, the anomalous Hall signal remained temperature independent across the entire investigated temperature range, from 15 mK to 300 K. Although we were unable to reliably extract the anomalous Hall conductivity due to the unevenness of the flake's height profile and the large contact size relative to the sample area, we strongly believe that the observed AHE is genuine and intrinsic in nature, as suggested by its temperature independence. This phenomenon is further accompanied by a striking longitudinal resistance, which demonstrated a complete absence of magnetoresistance up to ± 30 T across all investigated temperatures.

The results presented in this thesis have significant implications for the field of solid-state physics. The mechanical exfoliation method we developed is easily reproducible and can be applied to other materials, particularly those that are more challenging to exfoliate. Our discovery of the anomalous Hall effect in thin bismuth also reshapes the understanding of its electronic properties, as diamagnetic materials are not typically expected to exhibit AHE. This suggests the existence of a hidden mechanism that breaks time-reversal symmetry in bismuth, although its origin remains unclear. Further investigation is needed to fully comprehend the AHE in thin bismuth, and in the following section, we propose possible directions for future research.

7.2 Future Work

While Chapter 6 already outlined potential avenues for future exploration, here we discuss them in greater detail.

Characterization

Additional characterization of the bismuth flakes is warranted. As previously mentioned, TEM can be employed to image the surface of the thin exfoliated flakes, allowing for a more precise assessment of their quality. Furthermore, conducting X-ray diffraction (XRD) studies on the exfoliated bismuth flakes would be beneficial for understand-

ing and confirming their crystal orientation.

Devices Towards the 2D Limit

Several factors have contributed to the difficulty in producing devices with thinner bismuth flakes. The primary challenge is that thin flakes are difficult to be visually detected during the initial screening stage, as discussed in Chapter 6. To improve the optical contrast, a red filter can be used, as mentioned in Appendix A. Additionally, this selection process can be automated using a motorized microstage, with artificial intelligence (AI) models applied to identify the desired flakes. This approach could significantly increase the yield within a given timeframe. Similarly, an automated scanning process would be beneficial for identifying ultra-thin flakes with relatively large surface areas, which is particularly important when fabricating devices where the contact size is small relative to the flake.

Finally, the possibility of etching the flakes after exfoliation should be explored. This approach could further reduce their thickness and provide more precise control. However, the etching process must be conducted carefully and thoroughly characterized, as it can potentially degrade the quality of the flakes.

Further Analysis

Besides fabricating additional devices, the existing ones should also continue to be investigated. This includes collecting in-plane data, such as studying the anisotropic magnetoresistance and the planar Hall effect. Subjecting the devices to more extreme conditions, such as in a pulsed magnetic field, can also yield interesting insights.

7.3 Closing Remarks

The experimental results we have discussed in this thesis is an addition to the recent resurgence in interest for bismuth in its 2D form. We have introduced a new, accessible method for obtaining thin bismuth flakes, which we hope will enable more research

groups around the globe to explore their properties. Furthermore, the anomalous Hall effect, likely arising from the surface, suggests that as bismuth becomes thinner, its properties can change drastically and unexpectedly. Importantly, even after hundreds of years of extensive study, bismuth continues to surprise the community and advance our understanding of solid-state physics.

A

Supplemental Information: Method of mechanical exfoliation of bismuth with micro-trench structures

A.1 Contrast Optimization

As noted in the main text, thin flakes become more difficult to observe as their thickness decreases. Since flakes are identified visually through an optical microscope, one can easily overlook flakes that are ultra-thin. To mitigate this, we studied the contrast for ultra-thin bismuth flakes on SiO_2 micro-trench structures following the work done by Blake *et al.* for graphene [1].

The contrast is defined as the normalized absolute difference between reflected light intensity in the presence and absence of a bismuth flake, specifically

$$C = \left| \frac{R - R_0}{R_0} \right|,$$

where C is the contrast, R_0 is the reflectivity in the absence of a bismuth flake and R is the reflectivity in the presence of a bismuth flake. We show in Fig. A.1(a) and Fig. A.1(b) the contrast colorplots for the mesa (300 nm SiO_2) and the trench (275 nm SiO_2), respectively. We chose to use the indices of refraction as in Palik [2] for Si and SiO_2 as well as Hagemann *et al.* [3] for bismuth. However we also compared to indices of refraction reported by Lenham *et al.* [4] and by Abu El-Haija *et al.* [5], and found negligible difference for the ultra-thin bismuth flakes analyzed here.

In both Fig. A.1(a) and (b), the bright yellow part shows high contrast for flakes larger than 25 nm in the optical wavelength range, however for flake thicknesses less than 20nm, the contrast decreases drastically. This makes the ultra-thin bismuth flakes very difficult to observe with the naked eye and often requires AFM imaging to confirm the presence of bismuth flake.

This can be improved by using filters. Based on the our calculations, the contrast for sub-10 nm bismuth flakes can be optimized with a filter of 503 nm and 567 nm for mesa and trench respectively, which corresponds to a red filter in the electromagnetic spectrum. This is shown in Fig. A.1(c) by the red lines where the contrast for these two wavelengths are compared to the contrast averaged over power spectral density of

the optical microscope's halogen bulb for both the mesa (300 nm) and trench (275 nm). Consequently, the use of a red filter improves the visibility of the sub-20 nm bismuth flakes.

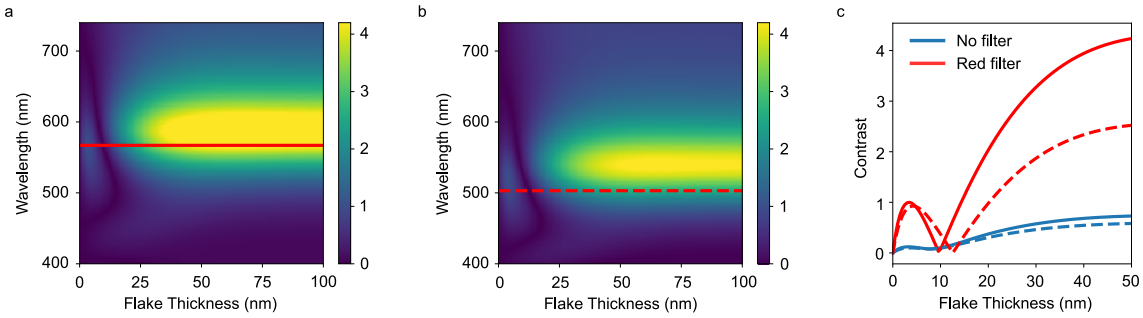

Figure A.1: Contrast plots for (a) 300 nm silicon oxide (mesa) and (b) 275 nm silicon oxide (trench). The red lines are the optimized wavelengths (567 nm for mesa and 503 nm for trench) for ultra-thin flake visiblility. (c) These optimal wavelengths are extracted and compared to the contrast given by the optical microscope's halogen bulb (blue line is for mesa, and dashed blue line is for trench).

A.2 References

[1] P. Blake, E.W. Hill, A.H. Castro Neto, K.S. Novoselov, D. Jiang, R. Yang, T.J. Booth, and A.K. Geim, "Making graphene visible," App. Phys. Lett. **91**, (2007).

[2] E. D. Palik, *Handbook of Optical Constants and Solids* (Academic Press, Cambridge, 1998) p. 173.

[3] H.-J. Hagemann, W. Gudat, and C. Kunz, "Optical constants from the far infrared to the x-ray region: Mg, Al, Cu, Ag, Au, Bi, C, and Al_2O_3," J. Opt. Soc. Am. **65**, 742 (1975).

[4] A.P. Lenham, D.M. Treherne, and R.J. Metcalfe, "Optical Properties of Antimony and Bismuth Crystals," J. Opt. Soc. Am. **55**, 1072 (1965)

[5] A.J. Abu El-Haija, A.A. Rousan, and L.H. Abuhassan, "The Basic Optical Properties, Optical Constants and Optical Conductivity of Bismuth Single Thin Films and Bismuth–Copper Bilayer Systems," Phys. Stat. Sol. (a) **168**, 505 (1998).

B

Supplemental Information: Anomalous Hall Effect in Thin Bismuth

B.1 Transport Measurements

The resistance of the thin bismuth device was measured with a voltage pre-amplifier using a quasi-DC technique at a frequency of 17.777 Hz and with an excitation current of 100 nA. The low-temperature measurements were performed in a Blufors BF-LD250 dilution refrigerator fitted with a 9 T magnet.

B.2 Temperature Dependence

Given that there are four different configurations used in the Onsager symmetrization, we show the resistance versus temperature traces for all of them for completeness. The R_{xx} and R_{xy} are shown in Fig. S1(a) and (b), respectively. Note that the trace for XX2 was shown in the main text of the manuscript.

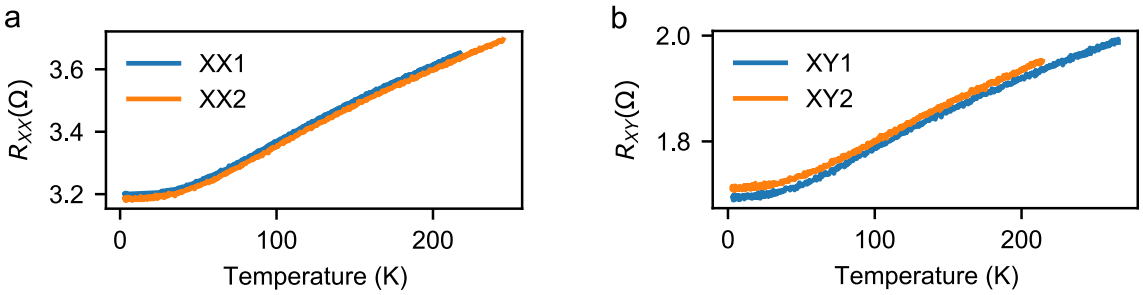

Figure B.1: Temperature dependence of the resistance for (a) R_{xx} Onsager pairs and (b) R_{xy} Onsager pairs.

B.3 Optical Images and AFM Scans

The optical image before contact patterning is shown below in Fig. S2(a). The corresponding AFM scan is shown in Fig. S2(b). A profile is selected across the flake where the height versus position graph is shown in Fig. S2(c). Note that the latter shows a non-negligible height variation, and we found an average height of 68 ± 47 nm. Despite this height variation, note that we have observed similar AHE in our comb devices (see below) of different thicknesses, and as such we do not expect the unevenness to play an important role in the soundness of our conclusion.

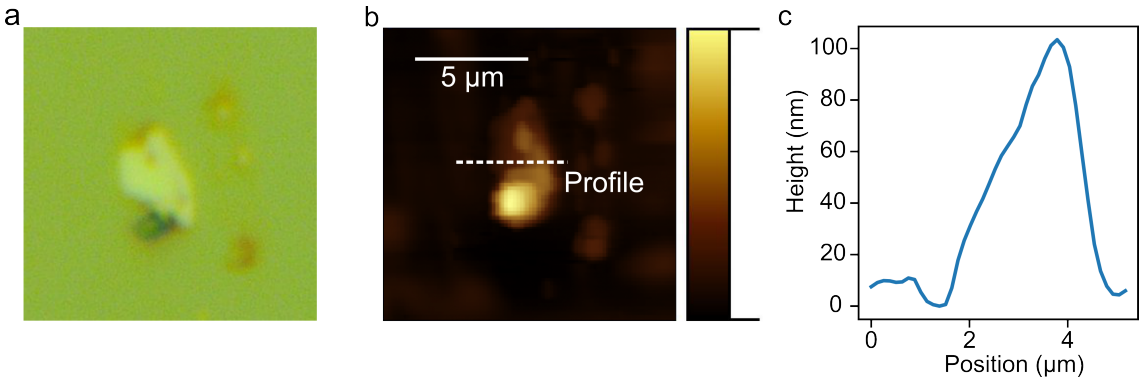

Figure B.2: (a) Original optical image of the flake. (b) The corresponding AFM scan of the same flake. (c) The height profile as selected in the AFM scan.

B.4 Additional Comb Devices

We have observed the Anomalous Hall Effect in two other devices which we label device A and device B. These two devices were fabricated in a comb geometry rather than in a van der Pauw geometry as for the device presented in the main text. We observed the AHE in these two comb devices because of the mixing of transport components due to imperfections in the contacts. The optical images of the devices are shown below in Fig. S3. The thicknesses for devices A and B are 69 ± 20 nm and 29 ± 19 nm, respectively. The resistances are 19 Ω and 32 Ω for devices A and B, respectively.

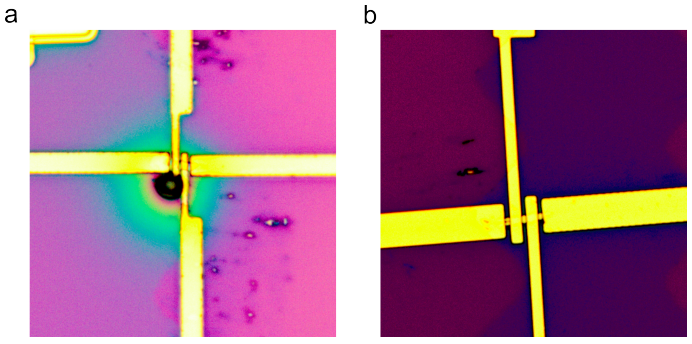

Figure B.3: (a) 69 nm thin device A and (b) 29 nm thin device B both patterned the comb geometry. Note that the black dot in (a) is likely to be a particle of insulating SiO_2 left on the surface after cleaving the substrate for packaging.

For device A, we present the raw measured four-point resistance versus the magnetic field, shown below in Fig. S4.

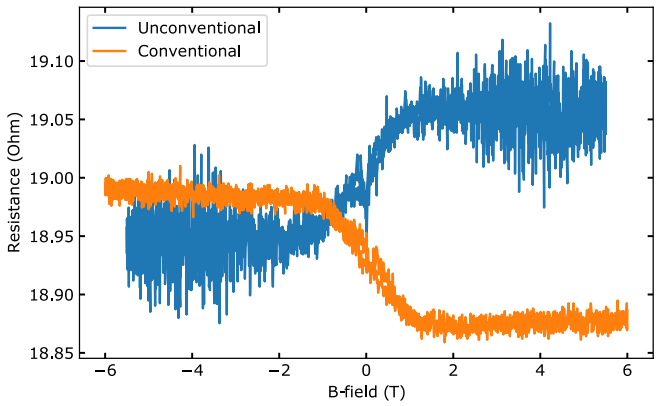

Figure B.4: Four-point resistance versus the magnetic field for device A.

The conventional configuration is the usual I+/V+/V-/I- configuration where the current contacts are on the outside of the comb geometry and the voltage probes are in the center. In contrast, the unconventional configuration is obtained by inverting I+ with V+ and I- with V-. This effectively becomes the Onsager reciprocal of the conventional setup. Although the AHE is clearly observed, the two curves do not cross at the origin which we attribute tentatively to the non-ideal configuration for Hall response used here.

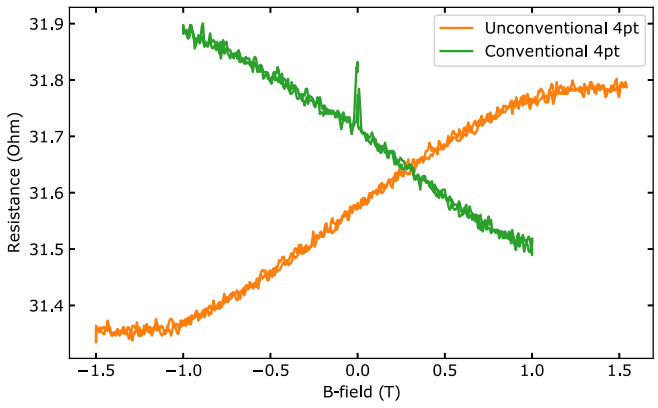

Figure B.5: Four-point resistance versus the magnetic field for device B.

In Fig. S5 below we show the resistance dependence on the magnetic field for device B. Similarly to device A, the AHE is clearly observed despite a vertical offset most likely due to the non-ideal configuration for measuring a Hall response.

B.5 Linear Fits of the Anomalous Hall Response

We perform linear fits on the anti-symmetrized data shown in the main text of the manuscript. The high-field region is chosen to be $|B| \geq 2$ T and the low field region is chosen as $|B| \leq 0.5$ T. The corresponding slopes are shown in Fig. S6.

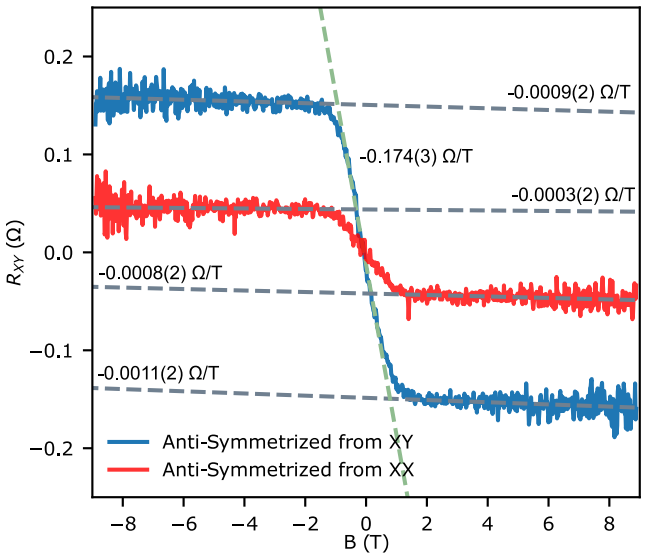

Figure B.6: Linear fit for the high and low field regions of the AHE data shown in the main text of the manuscript.

C

Supplemental Information: Observation of Temperature Independent Anomalous Hall Effect in Thin Bismuth from Near Absolute Zero to 300 K Temperature

C.1 Device Fabrication and Characterization

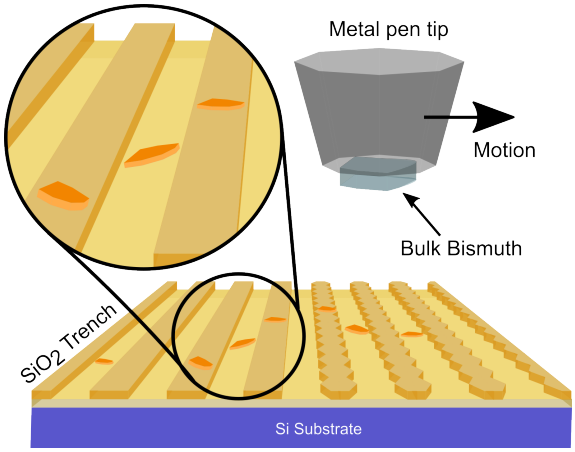

Figure C.1: Schematic of the mechanical exfoliation process that uses a micro-trench structure. A bulk single crystal bismuth is glued to a pen which is then used to grate against a SiO_2 surface with micro-trenches in order to exfoliate thin bismuth flakes.

Thin bismuth flakes were exfoliated with our newly-developed mechanical exfoliation technique that utilizes micro-trench structures [1]. To do so, a bulk bismuth single crystalline sample of 99.9% purity was attached to a metal pen as shown in Fig. C.1. The orientation of the sample was carefully chosen such that the bottom surface is the (111) crystal plane. This pen was then used to grate the bulk bismuth against a SiO_2 surface patterned with micro-trenches designed to facilitate the breakage of interlayer bonds in bismuth as depicted in Fig. C.1. With this method, it is possible to produce thin flakes with thicknesses down to the 2 nm range. Importantly, the entire exfoliation process was performed in a nitrogen-only glovebox with O_2 and water concentrations both less than 1 ppm, and as such oxidation of the exfoliated bismuth flakes was avoided. Additionally, a polymethyl methacrylate (PMMA) protection capping layer was deposited after the entire fabrication process in order to further protect the device from oxidation. Note that since the surface of contact is chosen to be the (111) crystal plane, and since the bond between these planes is the weakest, we naturally expect the resulting bismuth flakes to also have the (111) plane as their surface. The bismuth nature of the fabricated devices was confirmed with Raman spectroscopy and benchmarked with the parent bulk crystal as well as bismuth oxide. In particular, the Raman spectroscopy

showed no sign of bismuth oxide or aging effects for a period of more than two years since the devices' fabrication. Further details of our fabrication technique and pertaining to the Raman characterization can be found in Ref. [1,2]. As a final step, the selected flakes were patterned with 15nm/100nm Ti/Au contacts and then capped again with a PMMA protection layer.

The bismuth flakes were characterized with atomic force microscopy (AFM) in order to identify the most promising flakes for electronic transport devices. Figures C.2**(a)**,**(b)** show the optical microscopy image and the AFM measurement of the bismuth device presented in the main manuscript. In Fig. C.2**(b)**, a height profile is selected across the bismuth flake which is shown in Fig. C.2**(c)**. Note that the height profile shows a non-negligible height variation, and by comparing with the active channel in the final device (Fig. 2**(b)** of the manuscript), the average height is calculated to be 68 ± 47 nm. The large uncertainty is due to the wedge shape of the sample shown in Fig. C.2**(c)**. Despite this large uncertainty, we do not expect this height variation to impact the transport measurements in a significant way, because we also observed the anomalous Hall effect in other devices fabricated using the same technique, yet with different thickness (29 ± 19 nm and 69 ± 20 nm) [2].

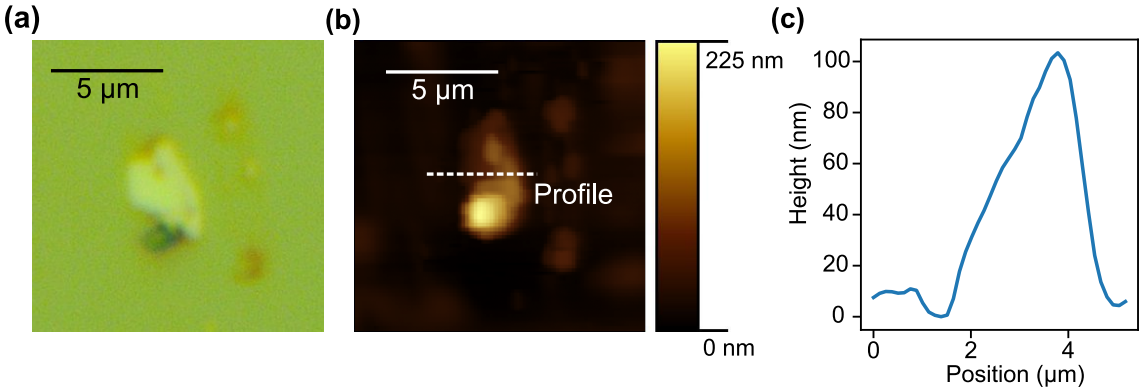

Figure C.2: **(a)** Original optical image of the device flake. **(b)** The corresponding AFM scan of the same flake. **(c)** The height profile as selected in the AFM scan.

C.2 Measurement Circuit

All the data in the manuscript is taken using the standard four-terminal method. This four-terminal resistance was measured using a quasi-DC (very low AC frequency) technique with a Stanford Research Systems SR560 low noise voltage preamplifier and a Stanford Research Systems SR830 lock-in amplifier. The frequency used was 17.671 Hz and the excitation current was set to 500 nA for all data presented between ± 30 T at and above 1.4 K. An excitation current of 100 nA was used for measurements taken at 15 mK and between ± 9 T during a separate cooldown in a dilution refrigerator [2].

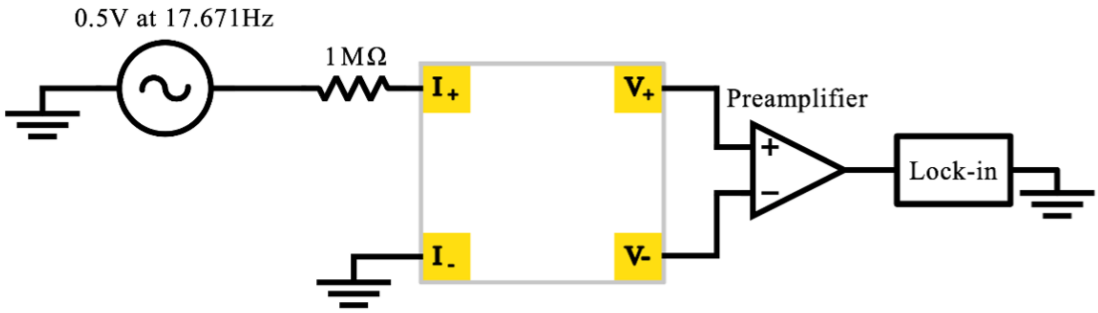

Figure C.3: The measurement circuit used to measure the four-terminal resistances for the XX1 configuration.

It is important to note that all the contacts are ohmic with contact resistances in the range of 56 to 106 Ω for a pair of contacts. The AC two point contact resistances versus I_{DC} is shown below for the four contact pairs and the XY1 configuration. This effectively shows that the device's contacts are ohmic at a base temperature of 15 mK.

Furthermore, all the consistency checks have been performed for different four-point resistance configurations. In particular, all the current reversal checks (*e.g.* $R_{12,34} = R_{21,43}$) and reciprocity theorem checks (*e.g.* $R_{21,34} + R_{12,43} = R_{43,12} + R_{34,21}$) have been performed, and are all found to be within 1.5% of one another.

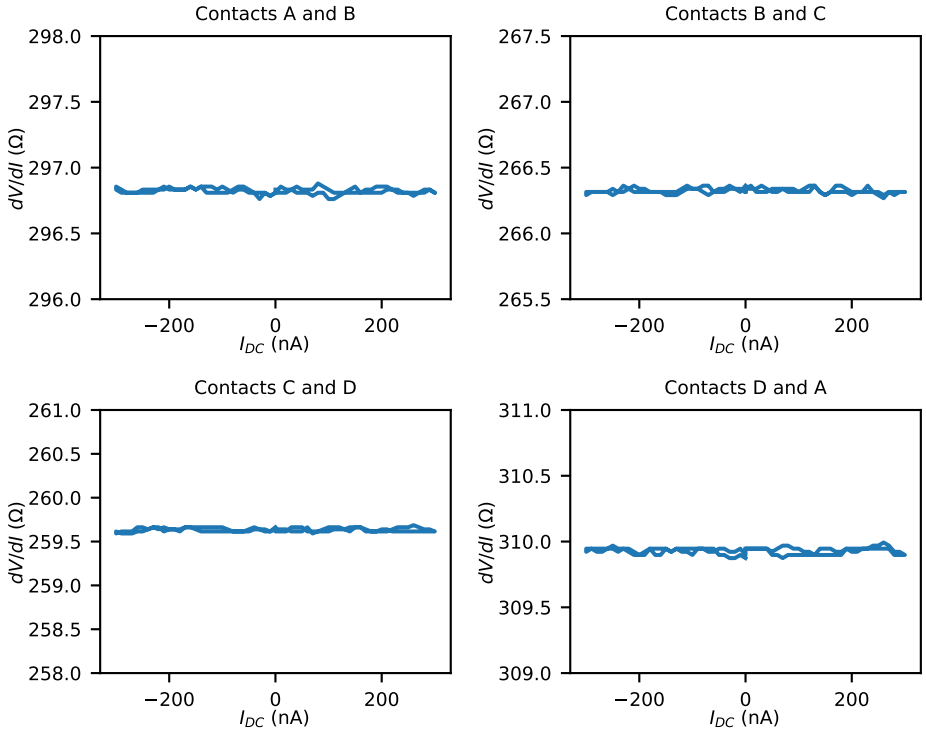

Figure C.4: dV/dI versus I_{DC} for the four contact pairs.

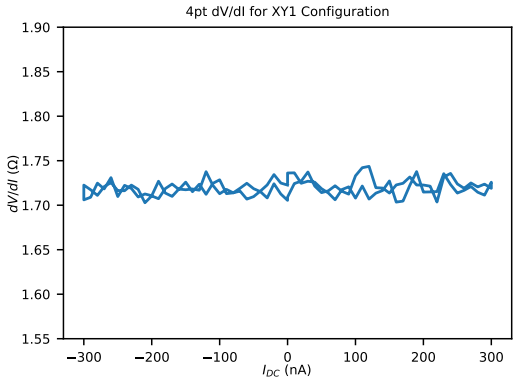

Figure C.5: dV/dI versus I_{DC} for the XY1 configuration.

C.3 Extraction of the Longitudinal and Hall Resistances

To extract the Hall and longitudinal resistances that were mixed due to the small size of the sample and contact misalignments, we use a symmetrization based on Onsager's reciprocal relations [3]. Specifically, Onsager symmetrization [3] states that in a linear

system, the resistance tensor

$$R = \begin{pmatrix} R_{xx} & R_{xy} \\ -R_{xy} & R_{xx} \end{pmatrix}$$

is transposed upon reversal of the current and voltage probes. Therefore, measuring the same contacts twice while reversing the current and voltage probes allows the decoupling of the longitudinal (R_{xx}) and the Hall (R_{xy}) resistances by symmetrizing and anti-symmetrizing the raw data. Specifically, this is achieved via the following formulas:

$$R_{xx} = \frac{R + R'}{2},$$
$$\text{and} \qquad R_{xy} = \frac{R - R'}{2},$$

where R and R' form an Onsager reciprocal pair whose voltage and current leads are reversed, *i.e.* $V_+ \longleftrightarrow I_+$ and $V_- \longleftrightarrow I_-$.

Note that for the symmetrization and anti-symmetrization, wed create $N = 120$ bins between $B = -30$ T and $B = 30$ T. R and R' are averaged for these bins, then plugged into the above equations to calculate R_{xx} and R_{xy}.

C.4 Temperature Dependence

Recall that Fig. 4**(d)** in the manuscript shows the dependence of longitudinal resistances on the magnetic field at various temperatures, and in the background, a raw XX four-point resistance's temperature dependence is shown for comparison. For completeness, here we show in Fig. C.6 the full temperature dependences for all XX and XY Onsager pairs that were used for the symmetrization and anti-symmetrization procedures to obtain the XX and XY electronic transport components (see Fig. 3**(c, f)** of the main manuscript).

In Fig. 3 of the manuscript, we present the raw resistances versus the magnetic field for XX and XY Onsager pairs at $T = 1.4$ K. For completeness, Fig. C.7 shows the raw

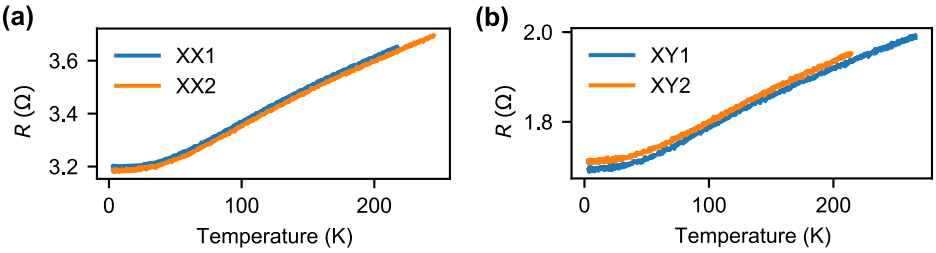

Figure C.6: Temperature dependence of the resistance for the **(a)** XX Onsager pairs and **(b)** XY Onsager pairs.

resistances versus the magnetic field for these Onsager pairs at temperatures 1.4 K, 40 K, 80 K, 160 K, 240 K and 300 K. We also show the data at 15 mK during a separate cooldown in a dilution refrigerator in Fig. C.10. The same AHE is observed, and is overlayed with data shown in Fig. 4(a) of the main text which were taken in a variable temperature insert (VTI) at the National High Magnetic Field Laboratory (NHMFL).

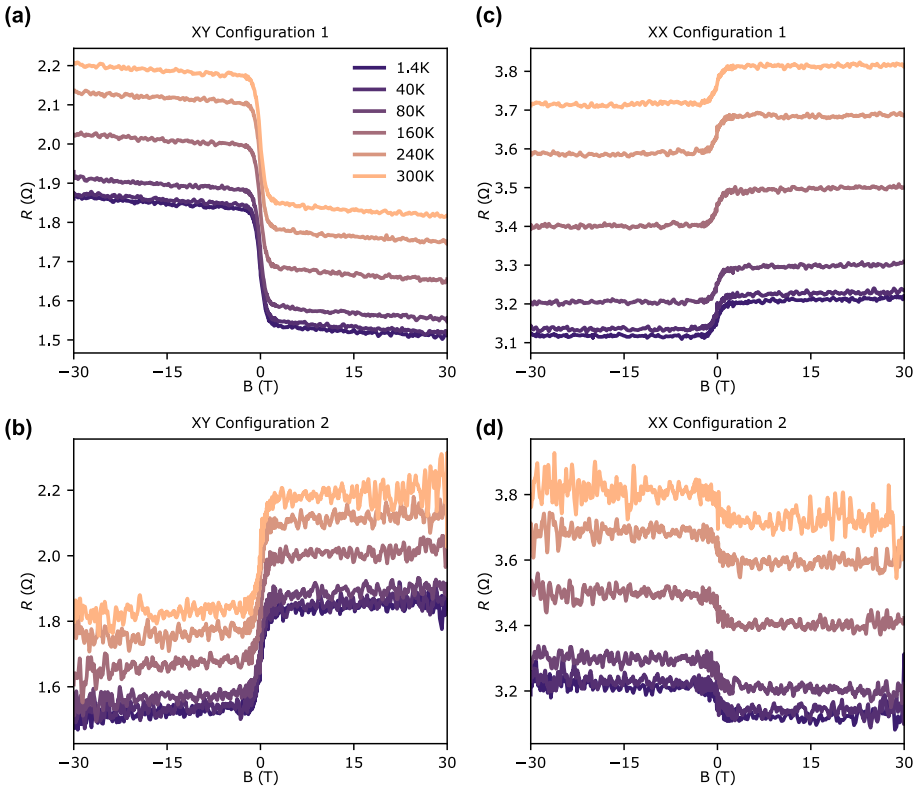

Figure C.7: Raw resistances versus the magnetic field for **(a, b)** the XY Onsager pairs and **(c, d)** the XX Onsager pairs.

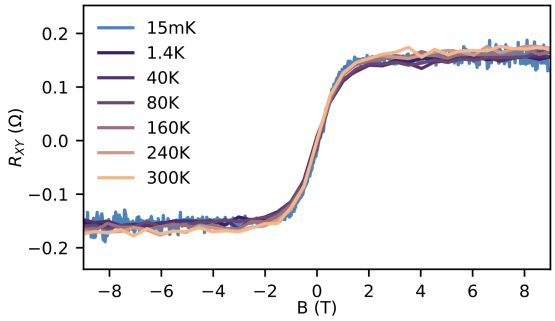

Figure C.8: Resistances versus magnetic field of the anti-symmetrized XY Onsager pairs, including the 15 mK data taken during a separate cooldown.

C.5 Multi-Carrier Model for the Hall and Longitudinal Resistances

While a single valley system can potentially explain the field-independent ρ_{xx} [13] observed in our work, this would lead to a Hall coefficient that is unreasonably small (for example $0.00106(13)\ \Omega\,\mathrm{T}^{-1}$ at 1.4 K). In addition, bulk bismuth is also known to host both electron and hole pockets [14, 15], and as a result a multi-carrier model can only exhibit a featureless ρ_{xx} at high magnetic fields when the carrier concentrations are different, *i.e.* when $n \neq p$ [13]. This occurs when the field strength exceeds a characteristic field

$$B^{\star} = \frac{n\nu + p\mu}{|n - p|\mu\nu}, \tag{C.1}$$

where n, p are the electron and hole concentrations and ν, μ are the electron and hole mobilities. When $|B| \leq B^{\star}$, a B^2 dependence [13] is nevertheless expected, and this is clearly not observed in the data presented in Fig. 3**(f)** of the main text. Furthermore, we note that it is not possible to fit the parameters mentioned above, because of the complete lack of explicit dependence on the magnetic field for ρ_{xx}, and therefore this is uncharacteristic of two carrier types that would be contributing to the electronic transport. We therefore believe that a more elaborate model is required to understand and explain both the longitudinal resistivity that shows no sign of magnetoresistance as well as the AHE observed in our work.

C.6 Effect of Diamagnetism of Bismuth

Since bismuth is diamagnetic, it induces an opposing magnetization M proportional to the external applied field $\mu_0 H$ given by $M = \chi H$ where χ is the magnetic susceptibility. The effective field B is then

$$B = \mu_0 H + \mu_0 M = \mu_0 H(1 + \chi).$$

In bismuth, as seen in Fig. C.9, χ depends on temperature and crystal direction. For temperatures below 300 K,

$$-2.4 \times 10^{-4} < \chi < -1.3 \times 10^{-4},$$

which gives,

$$0.99976 < 1 + \chi < 0.99987.$$

This small correction factor means that any modification taking into account the difference between the external and effective field falls within the noise of our signal.

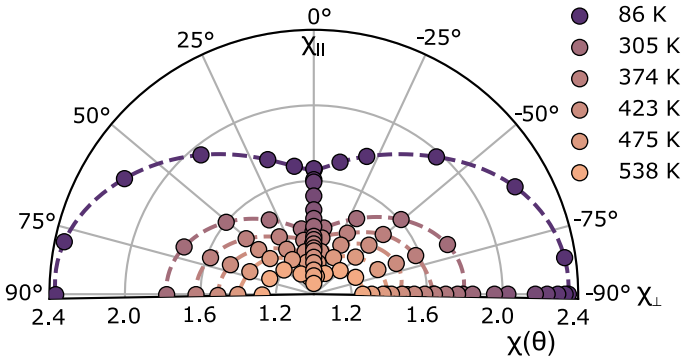

Figure C.9: The angular and temperature dependences of the diamagnetism of bismuth. Data digitized from Otake *et al.* [4].

C.7 Extraction of the Hall coefficient and Anomalous Hall Resistance

The anomalous Hall resistance is defined as the zero-field intercept of R_{xy}. To obtain this value, we fit the saturated part of R_{xy} ($|B| > 2$ T) and average the absolute values of the intercepts as shown in Fig. C.10 for $T = 1.4$ K, *i.e.*

$$R_{\text{AHE}} = \frac{0.147(1) + 0.146(1)}{2} = 0.146(2)\ \Omega,$$

where the errors are quoted from the linear regression fits and shown in parentheses. From the slopes fitted in Fig. C.10, we average the two slopes to find the Hall coefficient provided the main text, *i.e.*

$$R_H = \frac{0.00099(6) + 0.00114(7)}{2} = 0.00106(13)\ \Omega\,\text{T}^{-1}.$$

The same process was then repeated at all other temperatures chosen to perform the electronic transport measurements.

C.8 Scaling of the Anomalous Hall Effect

Given the non-trivial geometry in our transport device, it is challenging to extract confidently the geometric factor required to convert resistance to resistivity and conductance to conductivity. However, it can be observed in Fig. 3**(c, f)** of the manuscript that $\rho_{xx} \gg \rho_{xy}$, and in this regime, the intrinsic anomalous Hall resistivity $\rho_{\text{AHE}}^{\text{int}}$ is expected to scale with ρ_{xx}^2 [5, 6], *i.e.*

$$\rho_{\text{AHE}} = a_{sk}\rho_{xx} + b\rho_{xx}^2, \tag{C.2}$$

where the first term provides the skew-scattering contribution and the second term is the intrinsic contribution to the AHE. However, in some situations, the literature states that phonons can be neglected and in such case, the AHE conductivity can be written

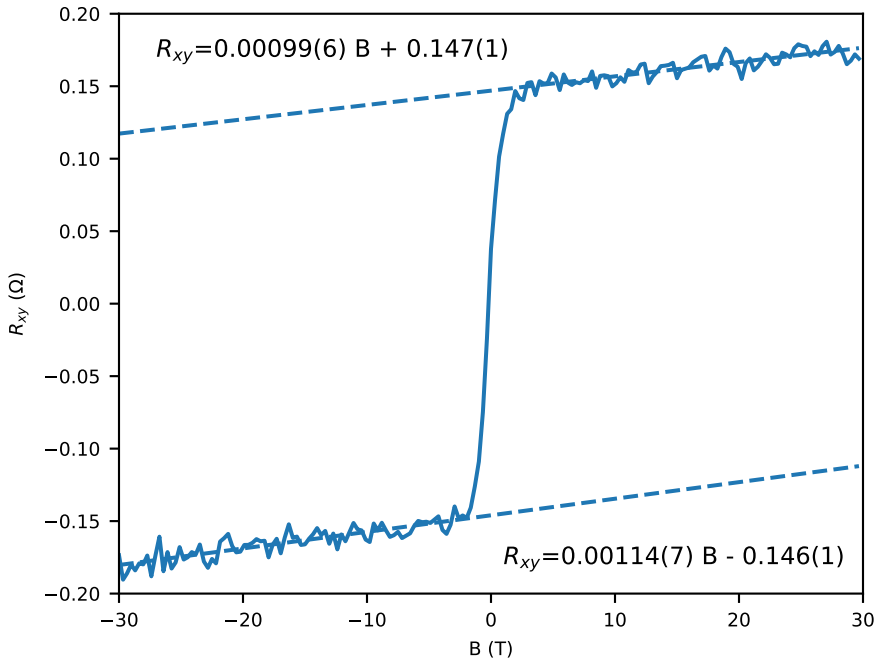

Figure C.10: Extraction of the Hall coefficient and R_{AHE} from $R_{xy}(B)$. The linear fits are restricted to the range $|B| > 2$ T. The fitted results are shown in the graph with the errors from the linear regression shown in parenthesis.

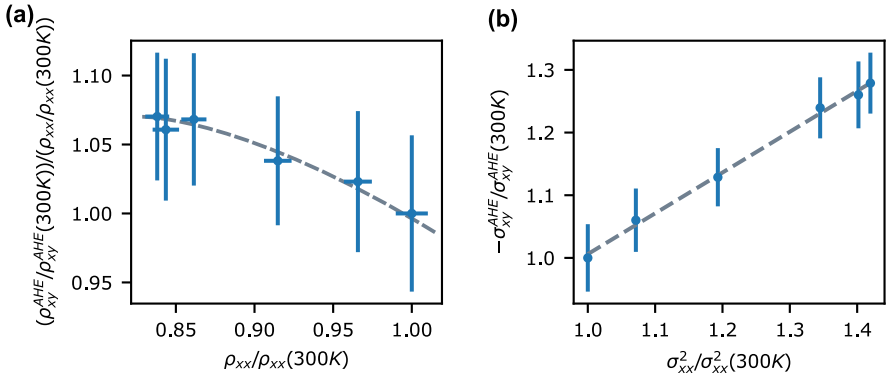

Figure C.11: **(a)** The departure from a linear $\rho_{\mathrm{AHE}}/\rho_{xx}$ versus ρ_{xx} indicates that Eq. (C.2) most likely does not apply in our case (see text below). The dashed gray line is a guide for the eye. **(b)** The linearity (with the linear fit shown by the gray line) of σ_{xy}^{AHE} vs σ_{xx}^2 confirms the validity of Eq. (C.3).

as [6]

$$-\sigma_{\mathrm{AHE}} = (\alpha\sigma_{xx0}^{-1} + \beta\sigma_{xx0}^{-2})\sigma_{xx}^2 + \sigma_{int}, \tag{C.3}$$

where α and β are coefficients for the skew-scattering and side-jump mechanisms respectively, σ_{xx0} is the residual conductivity and σ_{int} is the intrinsic anomalous Hall conductivity. In the spirit of not knowing the geometric factor for converting resistance to resistivity and then to conductivity, we can circumvent the verification of Eq. (C.2) and Eq. (5.2) in their normalized forms by dividing the 300 K data, as is shown in Fig. C.11. In particular, the normalized $\rho_{\mathrm{AHE}}/\rho_{xx}$ versus ρ_{xx} is shown in Fig. C.11**(a)**, and a clear deviation from linearity is observed with this formalism. Moreover, the fact that $\rho_{\mathrm{AHE}}/\rho_{xx}$ decreases with increasing ρ_{xx} implies that Eq. (C.2) does not model well our data. In contrast, Fig. C.11**(b)** shows that the normalized σ_{xy}^{AHE} scales linearly with the normalized σ_{xx}^2, indicating that Eq. (C.3) is a better model for the AHE observed in bismuth. Importantly, this shows that phonons induce a negligible effect on the skew-scattering term. In future works, when the resistivities will be confidently extracted, this model will allow us to quantify the intrinsic contribution of the AHE, and as such, the AHE observed in bismuth most likely emanates from an intrinsic mechanism related to a Berry curvature.

C.9 Temperature Dependence of the Anomalous Hall Resistivity

In Fig. C.12, we normalize the change in R_{AHE} defined by

$$\frac{\Delta R_{AHE}}{R_{AHE}(300\ \mathrm{K})} \equiv \frac{R_{AHE}(T) - R_{AHE}(300\ \mathrm{K})}{R_{AHE}(300\ \mathrm{K})},$$

and plot it versus the temperature to compare to other elemental materials also in the good-metal regime [7]. Note that the ρ_{AHE} of these materials was reconstructed from the tensor relation $\hat{\rho} = \hat{\sigma}^{-1}$. In our experiment, the sample was mounted on a rotating probe that is prone to a slight uncertainty in the angle which was estimated to be $\Delta\theta \approx 5^{\circ}$. From the angular dependence shown in the section below, the error bars from this angular uncertainty were then estimated for the bismuth data shown in Fig. C.12. We emphasize that our R_{AHE} is extremely insensitive to temperature variations even

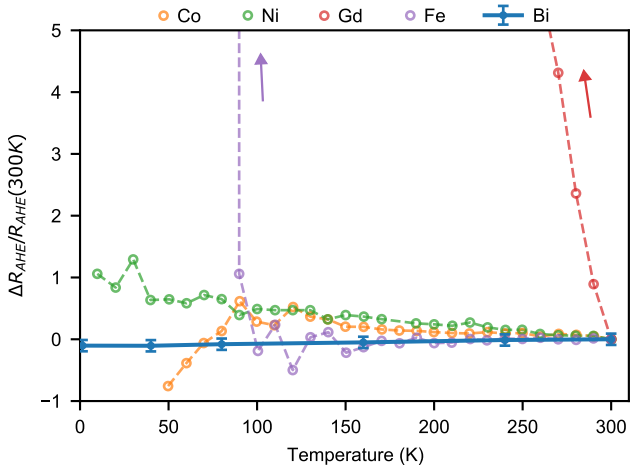

Figure C.12: The change in anomalous Hall resistance in our bismuth device compared with other elemental films also in the good-metal regime [7]. The uncertainty in our data is due to a uncertainty in the alignment of the magnetic field and the sample's plane. Within the observed noise and errors, the data shows negligible temperature dependence in the AHE from 1.4 K to 300 K.

compared to the materials shown in Fig. C.12 which are believed to exhibit the intrinsic type of the AHE. Such temperature independence is also reminiscent of the QAHE whose resistance is quantized to h/e^2 at temperatures below a critical temperature T_C. Curiously, bismuth has recently been reported to be a higher order topological insulator [8,9] and a Weyl semi-metal [10], and we note that both are systems that can exhibit the AHE and the QAHE [11, 12].

C.10 Resistance Uncertainty due to Angular Alignment

The angle of the magnetic field with respect to the device was varied between 0° and 90° by rotating the chip carrier on the probe of the variable temperature insert (VTI) (see Fig. **2(d)** of the main manuscript) while keeping the direction of the magnetic field fixed. We define 0° when the magnetic field is entirely perpendicular to the device that is in the (111) direction of the thin bismuth. As the angle θ is varied, upon reaching 90°, the magnetic field is entirely in the plane of the Si/SiO_2 substrate and hence our device. A schematic of the sample rotation with respect to the magnetic field is shown in the inset of Fig. C.13.

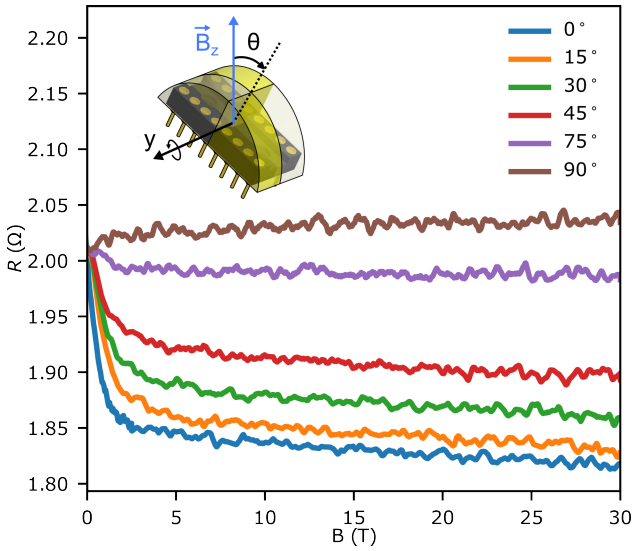

Figure C.13: Resistance versus the magnetic field for the XY1 configuration at 300 K. This angular dependence is used to estimate the error bars due to angle misalignment in Fig. C.12.

In the XY configuration 1, the Hall signal is measured at 300 K between 0 T to 30 T and for angles $0^\circ \leq \theta \leq 90^\circ$. The obtained curves are plotted in Fig. C.13. Note that due to the larger noise present at 300 K of the other XY configuration, we show the raw data that is not anti-symmetrized. However, the longitudinal resistance R_{xx} is field-independent (see Fig. 4 of the main manuscript), and the XY configuration 1 alone captures the essence of the Hall trend despite the mixing between R_{xy} and R_{xx}.

Finally, since the error bars in Fig. C.12 are dominated by the uncertainty in the angle, we can use Fig. C.13 to estimate the uncertainty in R_{AHE}. Focusing on $\theta = 0^\circ$ and $\theta = 15^\circ$, we estimate the change in the anomalous Hall resistance to be $0.001\ \Omega/\deg$. This was then used to calculate the error bars in Fig. C.12.

C.11 References

[1] Oulin Yu, R. Allgayer, S. Godin, J. Lalande, P. Fossati, Chunwei Hsu, T. Szkopek, and G. Gervais. Method of Mechanical Exfoliation of Bismuth with Micro-Trench Structures, J. Appl. Phys. **134**, 244302 (2023).

[2] Oulin Yu, Sujatha Vijayakrishnan, R. Allgayer, T. Szkopek, and G. Gervais, Anomalous Hall Effect in Thin Bismuth, Phys. Rev. B **109**, L121406 (2024).

[3] H. H. Sample, W. J. Bruno, S. B. Sample, and E. K. Sichel, Reverse-field reciprocity for conducting specimens in magnetic fields, J. of Appl. Phys. **61**, 1079 (1987).

[4] S. Otake, M. Momiuchi, and N. Matsuno, Temperature Dependence of the Magnetic Susceptibility of Bismuth, J. Phys. Soc. Jpn **49**, 1824 (1980).

[5] N. Nagaosa, J. Sinova, S. Onoda, A. H. MacDonald, and N. P. Ong, Anomalous Hall effect, Rev. Mod. Phys. **82**, 1539 (2010).

[6] Y. Tian, L. Ye, and X. Jin, Proper Scaling of the Anomalous Hall Effect, Phys. Rev. Lett. **103**, 087206 (2009).

[7] T. Miyasato, N. Abe, T. Fujii, A. Asamitsu, S. Onoda, Y. Onose, N. Nagaosa, and Y. Tokura, Crossover Behavior of the Anomalous Hall Effect and Anomalous Nernst Effect in Itinerant Ferromagnets, Phys. Rev. Lett. **99**, 086602 (2007).

[8] L. Aggarwal, P. Zhu, T. L. Hughes, and M. Vidya, Evidence for higher order topology in Bi and $Bi_{0.92}Sb_{0.08}$, Nat. Commun. **12**, 4420 (2021).

[9] F. Schindler, *et al*, Higher-order topology in bismuth, Nat. Phys. **14**, 918 (2018).

[10] Q. Lu, *et al.*, Observation of 2D Weyl Fermion States in Epitaxial Bismuthene, arXiv:2303.02971, (2023).

[11] A. A. Burkov, Anomalous Hall Effect in Weyl Metals, Phys. Rev. Lett. **113**, 187202 (2014).

[12] Y. Messica, D. B. Gutman, and P. M. Ostrovsky, Anomalous Hall effect in disordered Weyl semimetals, Phys. Rev. B **108**, 045121 (2023).

[13] Z. Zhu, B. Fauqué, K. Behnia, and Y. Fuseya, Magnetoresistance and valley degree of freedom in bulk bismuth, J. Phys. Condens. Matter **30**, 313001 (2018).

[14] A. L. Jain, S. Suri, and K. Tanaka, Charge carrier densities and mobilities in bismuth, Phys. Lett. A **28**, 435 (1968).

[15] A. L. Jain, and S. H. Koenig, Electrons and Holes in Bismuth, Phys. Rev. **127**, 442 (1962).

D

Supplemental Information: Device fabrication and its challenges

The exfoliation process described in Chapter 3 produced bismuth flakes across a wide range of thicknesses. The thinnest observed flake measures 2 nm, but the thicker flakes can easily exceed 100 nm and sometimes reach the micrometer range. This variability necessitates manual selection of the desired flakes for device fabrication, a process that can be both time consuming and labor intensive. The first step of the fabrication is to select the flakes visually, as their thickness affects their optical appearance on the substrate. However, very thin flakes become less visible, which prompted us to address the bismuth flakes' visibility and contrast optimization for the exfoliation process in Appendix A.

Anecdotally, with a pair of trained eyes one can easily spot flakes under 100 nm.

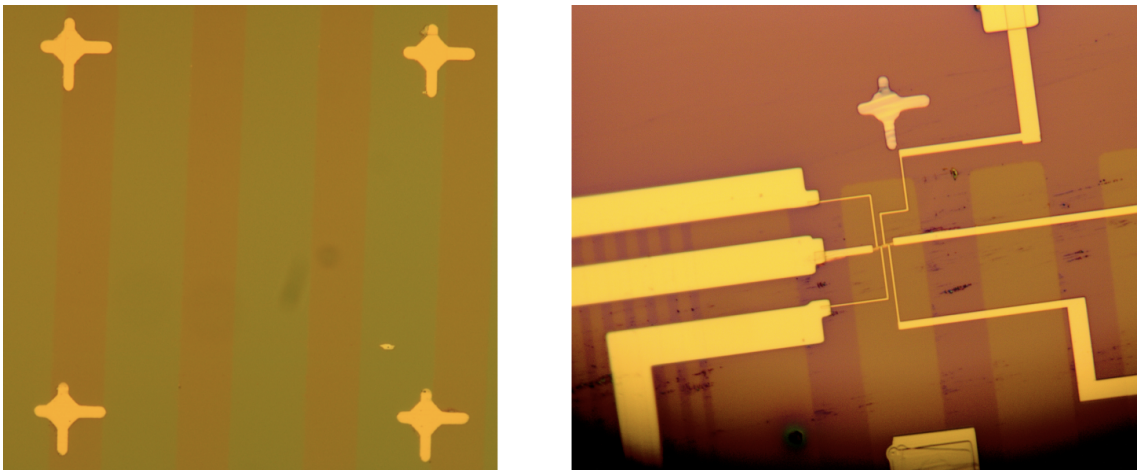

Figure D.1: (left) 100x magnification optical image showing a small bismuth flake, the micro-trenches and alignment marks. (right) a post fabrication device in the Hall bar geometry.

These candidates are then sent for AFM scanning, which serves two purposes: determining the exact thickness of the flakes and detecting any potential defects. This further refines the selection of flakes suitable for device fabrication. Once the flakes that are fit for patterning are identified, the substrate is spin-coated with PMMA. The exact thickness and type of PMMA are not critical, as long as it adequately covers the flakes, typically a few times thicker than the flakes themselves. We have also experimented with adding a second layer of methyl methacrylate (MMA) copolymer to facilitate the lift-off process. However, as we will discuss later, the use of MMA presents certain challenges.

It is important to capture the optical images of the flakes after spin-coating, as the process can occasionally shift the positions of the flakes. Note that the substrate contains alignment marks, which are crucial because the flakes are small, requiring the EBL pattern for the contacts to be aligned with high precision. This necessary precision is why the use of MMA has been avoided, as it increases the overall thickness of the photoresist, reducing the visibility of the alignment marks under the scanning electron microscope (SEM). An example of these alignment marks is shown in the left panel of Fig. D.1.

An automated software was developed to align each flake with the alignment marks. This process involves importing the optical image taken at 100x magnification, identi-

fying the coordinates of the alignment marks, and tracing the contour of the flake. The design is then exported as a GDSII/CSF file for further processing. Since each flake varies in size and location, the pattern design must be customized for each individual flake.

The EBL is carried out in two stages: first, a small aperture is used to achieve high precision for the fine features near the flake; then, to save time, a larger aperture is used to draw the contact pads, which will later be used for soldering. A standard recipe is followed for resist development, and the substrate is swiftly transferred to the metal deposition machine. This step must be done quickly to minimize the risk of flake oxidation.

Metal deposition is performed using a standard Ti/Au recipe, as discussed in previous manuscripts. The sample is then returned to the glovebox for lift-off using acetone, to prevent the bismuth flakes from coming into contact with air and humidity. Depending on how the lift-off progresses, an ultrasonic bath may be used briefly, typically for just a few seconds, to facilitate the process. Finally, another layer of PMMA is spin-coated onto the substrate as a protective cap layer before the sample is taken out of the glovebox for transport measurements. An optical image of the device after fabrication is shown in the right panel of Fig. D.1.

The resulting devices are first characterized on a probe station to measure two-point contact resistances and check for leakage. The yield success rate is low, as the devices often suffer from high contact resistance and leakage issues. Many ultra-thin devices exhibit high contact resistances, often in the tens of megaohms, and display Schottky behavior. Additionally, they frequently show unstable I-V characteristics. While current annealing can improve stability, the results remain inconsistent.

The promising devices are then mounted on G10 headers, with the pads leading to the devices soldered to the pins of the mount. Initially, a wirebonding technique was used, but many devices experienced gate leakage. A systematic test on raw microtrench substrates revealed that wirebonding significantly contributes to this leakage,

likely due to the degradation of the SiO_2 layer. This degradation is possibly caused by the RIE process during the micro-trench fabrication, as well as the mechanical stress from pressing bulk bismuth crystals against the substrate during exfoliation. To address this issue, the wirebonding process was replaced with indium soldering, which resulted in a higher device yield. As such, this concludes the fabrication and characterization process, and the devices are now ready for transport measurements.

References

[1] N. C. Norman, *Chemistry of Arsenic, Antimony, and Bismuth*, (Springer 1998), p. 41.

[2] R. Jackson, John Tyndall and the Early History of Diamagnetism, Ann Sci. **72**, 435 (2015).

[3] K. Sugihara, Thermomagnetic Effects in Bismuth. II. Nernst-Ettingshausen Effect, J. Phys. Soc. Jpn. **27**, 362 (1969).

[4] M. Z. Hasan, and J. E. Moore, Three-Dimensional Topological Insulators, Annu. Rev. Condens. Matter Phys. **2**, 55 (2010).

[5] S. P. Koenig, R. A. Doganov, H. Schmidt, A. H. Castro Neto, and B. Özyilmaz, Electric field effect in ultrathin black phosphorus, Appl. Phys. Lett **104**, 103106 (2014).

[6] Likai Li, Yijun Yu, Guo Jun Ye, Qingqin Ge, Xuedong Ou, Hua Wu, Donglai Feng, Xian Hui Chen, and Yuanbo Zhang, Black phosphorus field-effect transistors, Nat. Nanotechnol. **9**, 372 (2014).

[7] F. Reis, G. Li, L. Dudy, M. Bauernfeind, S. Glass, W. Hanke, R. Thomale, J. Schäfer, and R. Claessen, Bismuthene on a SiC substrate: A candidate for a high-temperature quantum spin Hall material, Science **357**, 287 (2017).

[8] L. Aggarwal, P. Zhu, T. L. Hughes, and V. Madhavan, Evidence for higher order topology in Bi and $Bi_{0.92}Sb_{0.08}$, Nat. Comm. **12**, (2021).

[9] F. Schindler, Z. Wang, M. G. Vergniory, A. M. Cook, A. Murani, S. Sengupta, A. Yu. Kasumov, R. Deblock, S. Jeon, I. Drozdov, H. Bouchiat, S. Guéron, A. Yazdani, B. A. Bernevig, and T. Neupert, Higher-order topology in bismuth, Nat. Phys. **14**, 918–924 (2018).

[10] O. Prakash, A. Kumar, A. Thamizhavel, and S. Ramakrishnan, Evidence for bulk superconductivity in pure bismuth single crystals at ambient pressure, Science **335**, 52-55 (2017).

[11] X. Gonze, J.-P. Michenaud, and J.-P. Vigneron, Ab initio calculations of bismuth properties, including spin–orbit coupling, Phys. Scr. **37**, 785 (1988).

[12] Ph. Hofmann, The surfaces of bismuth: Structural and electronic properties, Prog. Surf. Sci. **81**, 191-245 (2006).

[13] Y. Liu, and R.E. Allen, Electronic structure of the semimetals Bi and Sb, Phys. Rev. B **52**, 1566 (1995).

[14] Y. F. Ogrin, V.N. Lutskii, M.I. Elinson, Observation of quantum size effects in thin bismuth films, JETP Lett. **3**, 71 (1966).

[15] V. N. Lutskii, Features of optical absorption of metallic films in region where metal turns into a dielectric, Soviet Physics JETP Lett. **2**, 245 (1965).

[16] V. B. Sandomirskiĭ, Quantum Size Effect in a Semimetal Film, Soviet Physics JETP **25**, 101 (1967).

[17] A. L. Jain, and S. H. Koenig, Electrons and Holes in Bismuth, Phys. Rev. **127**, (1962).

[18] Y. Fuseya, M. Ogata, and H. Fukuyama, Transport Properties and Diamagnetism of Dirac Electrons in Bismuth, J. Phys. Soc. Jpn **84**, 012001 (2015).

[19] Zengwei Zhu, B. Fauqué, K. Behnia, and Y. Fuseya, J. Phys.: Condens. Matter **30**, 313001 (2018).

[20] E. H. Hall, On a New Action of the Magnet on Electric Currents, Am. J. Math **2**, 287 (1879).

[21] N. Nagaosa, J. Sinova, S. Onoda, A. H. MacDonald, and N. P. Ong, Anomalous Hall effect, Rev. Mod. Phys. **82**, 1539 (2010).

[22] M. V. Berry, Quantal phase factors accompanying adiabatic changes, Proc. R. Soc. Lond. A **392**, 45 (1984).

[23] Hongming Weng, Rui Yu, Xiao Hu, Xi Dai, and Zhong Fang, Quantum anomalous Hall effect and related topological electronic states, Adv. Phys. **64**, 227 (2015).

[24] R. Karplus, and J. M. Luttinger, Hall Effect in Ferromagnetics, Phys. Rev. **95**, 1154 (1954).

[25] J. Smit, The Spontaneous Hall Effect in Ferromagnetics I, Phys. **21**, 877 (1955).

[26] J. Smit, The Spontaneous Hall Effect in Ferromagnetics II, Phys. **24**, 39 (1958).

[27] L. Berger, Side-Jump Mechanism for the Hall Effect of Ferromagnets, Phys. Rev. B **2**, 4559 (1970).

[28] D. Xiao, M.-C. Chang, and Q. Niu, Berry phase effects on electronic properties, Rev. Mod. Phys. **82**, 1959 (2010).

[29] N. A. Sinitsyn, Semiclassical theories of the anomalous Hall effect, J. Phys.: Condens. Matter **20**, 023201 (2008).

[30] L. Berger, Influence of spin-orbit interaction on the transport processes in ferromagnetic nickel alloys, in the presence of a degeneracy of the 3d band, Physica **30**, 1141 (1964).

[31] N. A. Sinitsyn, Q. Niu, J. Sinova, and K. Nomura, Disorder effects in the anomalous Hall effect induced by Berry curvature, Phys. Rev. B **72**, 045346 (2005).

[32] Y. Tian, L. Ye, and X. Jin, Proper Scaling of the Anomalous Hall Effect, Phys. Rev. Lett. **103**, 087206 (2009).

[33] F. D. M. Haldane, Model for a Quantum Hall Effect without Landau Levels: Condensed-Matter Realization of the "Parity Anomaly", Phys. Rev. Lett. **61**, 2015 (1988).

[34] L. J. van der Pauw, A method of measuring specific resistivity and Hall effect of discs of arbitrary shape, Philips Res. Rep **13**, 1 (1958)

[35] W. Vernsel, Analysis of the Greek Cross, a Van der Pauw Structure with Finite Contacts, Solid-State Electron. **22**, 911 (1979).

[36] W. Vernsel, Analysis of Symmetrical Hall Plates with Finite Contacts, J. Appl. Phys. **52**, 4659 (1981).

[37] K. Szymański, J.L. Cieśliński, and K. Łapiński, Van der Pauw method on a sample with an isolated hole, Phys. Lett. A **377**, 651 (2013).

[38] K. Szymański, K. Łapiński, and J.L. Cieśliński, Determination of the Riemann modulus and sheet resistance of a sample with a hole by the van der Pauw method, Meas. Sci. Technol. **26**, 055003 (2015).

[39] H. B. G. Casimir, Reciprocity Theorems and Irreversible Processes, Proc. IEEE **51**, 1570 (1963).

[40] J. Meixner, Zur theorie der elektrischen transporterscheinungen im magnetfeld, Ann. der. Phys. **40**, 165 (1941).

[41] H. H. Sample, W. J. Bruno, S. B. Sample, and E. K. Sichel, Reverse-field reciprocity for conducting specimens in magnetic fields, J. of Appl. Phys. **61**, 1079-1084 (1987).

[42] M. Serlin, C. L. Tschirhart, H. Polshyn, Y. Zhang, J. Zhu, K. Watanabe, T. Taniguchi, K. Balents, and A. F. Young, Intrinsic quantized anomalous Hall effect in a moiré heterostructure, Science **367**, 900-903 (2019).

[43] Zhengguang Lu, Tonghang Han, Yuxuan Yao, A. P. Reddy, J. Yang, Junseok Seo, Kenji Watanabe, Takashi Taniguchi, Liang Fu, and Long Ju, Fractional quantum anomalous Hall effect in multilayer graphene, Nature **626**, 759 (2024).

[44] K. S. Novoselov, A. K. Geim, S. V. Morozov, D. Jiang, Y. Zhang, S.V. Dubonos, I. V. Grigorieva, and A. A. Firsov, Electric Field Effect in Atomically Thin Carbon Films, Science **306**, 666 (2004).

[45] V. Shanmugam, R. A. Mensah, K. Babu, S. Gawusu, A. Chanda, Y. Tu, R. E. Neisiany, M. Försth, G. Sas, and O. Das, A Review of the Synthesis, Properties, and Applications of 2D Materials, Part. Syst. Charact. **39**, 2200031 (2022).

[46] A. Castellanos-Gomez, L. Vicarelli, E. Prada, J. O. Island, K. L. Narasimha-Acharya, S. I. Blanter, D. J. Groenendijk, M. Buscema, G. A. Steele, J. V. Alvarez, H. W. Zandbergen, J. J. Palacios, and H. S. J. van der Zant, Isolation and characterization of few-layer black phosphorus, 2D Mater. **1**, 025001 (2014).

[47] Y. Huang, C. Zhu, S. Zhang, X. Hu, K. Zhang, W. Zhou, S. Guo, F. Xu, and H. Zeng, Ultrathin Bismuth Nanosheets for Stable Na-Ion Batteries: Clarification of Structure and Phase Transition by in Situ Observation, Nano Lett. **19**, 1118 (2019).

[48] Q.-Q. Yang, R.-T. Liu, C. Huang, Y.-F. Huang, L.-F. Gao, B. Sun, Z.-P. Huang, L. Zhang, C.-X. Hu, Z.-Q. Zhang, C.-L. Sun, Q. Wang, Y.-L. Tang, and H.-L. Zhang, 2D bismuthene fabricated via acid-intercalated exfoliation showing strong nonlinear near-infrared responses for mode-locking lasers, Nanoscale **10**, 21106 (2018).

[49] R. Gusmão, Z. Sofer, D. Bouša and M. Pumera, Pnictogen (As, Sb, Bi) Nanosheets for Electrochemical Applications Are Produced by Shear Exfoliation Using Kitchen Blenders, Angew. Chem. Int. Ed. **56**, 14417 (2017).

[50] A. C. Lazanas, K. Tsirka, A. S. Paipetis and M. I. Prodromidis, 2D bismuthene/-graphene modified electrodes for the ultra-sensitive stripping voltammetric determination of lead and cadmium, Electrochim. Acta **336**, 135726 (2020).

[51] L. Chen, A. X. Wu, N. Tulu, J. Wang, A. Juanson, K. Watanabe, T. Taniguchi, M. T. Pettes, M. A. Campbell, M. Xu, C. A. Gadre, Y. Zhou, H. Chen, P. Cao, L. A. Jauregui, R. Wu, X. Pan, and J. D. Sanchez-Yamagishi, Exceptional electronic

transport and quantum oscillations in thin bismuth crystals grown inside van der Waals materials, Nat. Mater. **23**, 741 (2024).

[52] Oulin Yu, R. Allgayer, S. Godin, J. Lalande, P. Fossati, Chunwei Hsu, T. Szkopek and G. Gervais, Method of Mechanical Exfoliation of Bismuth with Micro-Trench Structures, arXiv:2311.01321 (2023).

[53] Oulin. Yu, Sujatha Vijayakrishnan, R. Allgayer, T. Szkopek, and G. Gervais, Anomalous Hall effect in thin bismuth, Phys. Rev. B **109**, L121406 (2024).

[54] D. Wawrzika, J. I. Facioa, and J. van den Brink, Surface induced electronic Berry curvature in bulk Berry curvature free materials, Mater. Today Phys. **33**, 101027 (2023).

[55] Oulin Yu, F. Boivin, A. Silberztein, G. Gervais, Observation of Temperature Independent Anomalous Hall Effect in Thin Bismuth from Near Absolute Zero to 300 K Temperature, arXiv:2406.12134, (2024).

[56] E.S. Walker, S.R. Na, D. Jung, S.D. March, J.-S. Kim, T. Trivedi, W. Li, L. Tao, M.L. Lee, K.M. Liechti, D. Akinwande, and S.R. Bank, Large-Area Dry Transfer of Single-Crystalline Epitaxial Bismuth Thin Films, Nano Lett. **16**, 6931 (2016).

[57] V. Tayari, N. Hemsworth, I. Fakih, A. Favron, E. Gaufrès, G. Gervais, R. Martel and T. Szkopek, Two-Dimensional Magnetotransport in a Black Phosphorus Naked Quantum Well, Nat. Comm. **6**, 7702 (2015).

[58] D. L. Partin, J. Heremans, D. T. Morelli, C. M. Thrush, C. H. Olk, and T. A. Perry, Growth and characterization of epitaxial bismuth films, Phys. Rev. B **38**, 3818 (1988).

[59] F. Gity, L. Ansari, M. Lanius, P. Schüffelgen, G. Mussler, D. Grützmacher, and J.C. Greer, Reinventing solid state electronics: Harnessing quantum confinement in bismuth thin films, Appl. Phys. Lett **110**, 093111 (2017).

[60] C. A. Hoffman, J. R. Meyer, F. J. Bartoli, A. Di Venere, X. J. Yi, C. L. Hou, H. C. Wang, J. B. Ketterson, and G. K. Wong, Semimetal-to-semiconductor transition in bismuth thin films, Phys. Rev. B **48**, 11431 (1993).

[61] Nan Wang, Yu-Xiang Dai, Tian-Lin Wang, Hua-Zhe Yang, and Yang Qi, Investigation of growth characteristics and semimetal–semiconductor transition of polycrystalline bismuth thin films, IUCrJ **7**, 49 (2020).